*Doklady Physics, Vol. 45, No. 1, 2000, pp. 1–4. Translated from Doklady Akademii Nauk, Vol. 370, No. 1, 2000, pp. 34–37.*


**PHYSICS**

# On Additional Broadening of Spectral Lines in Plasma

**N. Yu. Orlov and Academician V. E. Fortov**

Received September 21, 1999

Solving many problems of plasma physics requires rather precise information on optical properties of plasma in a wide range of temperatures and densities. Theoretical models of plasmas, which were developed over the past few years, provide a way of calculating spectral absorption coefficients for the electromagnetic radiation and ranges according to Planck and Rosseland. The accuracy of such calculations depends upon specific physical approximations laying in the base of one or another model [1]. However, the problem of allowance for an entire abundance of spectral lines is common to all the models, even for light substances with a relatively low nuclear charge $Z$. For high $Z$ values, the number of the lines can exceed $10^8$ making the calculations impossible even with most advanced modern computers [2]. Such a great number of spectral lines is a consequence of the abundance of various kinds of ions, each having low concentration, which are contained in hot dense plasma along with highly concentrated atoms and ions. It is worth noting that spectral lines of low-concentration ions are often very close to the lines of high-concentration ones. If these lines merge, the resulting profile is determined not only by the Doppler and Stark effects, but also by the distribution of low-concentration ions. This fact is of particular importance in the cases of determining the plasma density by the broadening of spectral lines, when experimentally measured line widths are compared with results of calculations based on a certain model. To overcome these difficulties, along with the conventional mechanisms for the broadening of spectral lines, an approach is proposed in this paper, which we call the additional broadening. Parameters of this broadening are determined by the distribution of low-concentration ions. The subsequent discussion is based on the ionic model for a substance [1].

We consider plasma consisting of atoms and ions of a substance with the nuclear charge $Z$, the atomic number $A$, temperature $\Theta$, and the density $\rho$ (g/cm$^3$). A spherical atomic cell of the radius $r_0$ with a nucleus located at the cell center is used as a subsystem of the Gibbs statistics. The subsystems differ from one another by sets of occupation numbers $\{N_{nl}^j\}$ for electron quantum states belonging to the discrete spectrum. Here, $N_{nl}^j$ is the number of bound electrons of the subsystem $j$, which are in a state with the principal quantum number $n$ and the orbital quantum number $l$. In addition to the bound electrons localized nearby the nucleus, the subsystem contains electrons belonging to continuum, which move in the resulting field of both the nucleus and other electrons. Quantum states of each subsystem are interpreted as those of plasma atoms and ions. A set of equations for the self-consistent field describing states for an ensemble of plasma atoms and ions can be derived by the density-functional method. We restrict ourselves to the case of the Schrödinger equation for the single-electron radial wave functions. Then, the set of equations can be represented in the form

$$-\frac{1}{2}(R_{nl}^j)'' + \left[-V_j(r) + \frac{l(l+1)}{2r^2}\right]R_{nl}^j(r) = E_{nl}^j R_{nl}^j(r).$$

The boundary conditions are imposed as

$$R_{nl}^j(0) = 0, \quad R_{nl}^j(r_0) = 0.$$

The normalization conditions are written out in the form

$$\int_0^{r_0} R_{nl}^2(r)dr = 1.$$

The quantity $r_0$ is given by the formula

$$r_0 = \left[\frac{3}{4\pi N_A}\right]^{1/3}\frac{1}{a_0}\left[\frac{A}{\rho}\right]^{1/3},$$

where $a_0 = 5.292 \times 10^{-9}$ cm, $N_A = 6.02 \times 10^{23}$ is the Avogadro's number. Henceforth, the atomic system of units is used. The potential $V_j(r)$ is written out in the form $V_j(r) = V_1^j(r) + V_2^j(r)$, where

$$V_1^j(r) = \frac{Z}{r} - \frac{4\pi}{r}\int_0^r r_1^2\rho_j(r_1)dr_1 - 4\pi\int_r^{r_0} r_1\rho_j(r_1).$$

*Research Center of Pulse-Action Thermophysics,*
*Joint Institute for High Temperatures,*
*Russian Academy of Sciences,*
*Izhorskaya ul. 13/19, Moscow, 127412 Russia*

1028-3358/00/4501-0001$20.00 

The exchange interaction is approximated by the formula

$$V_2^j(r) = \frac{\pi\rho_j(r)}{\Theta}\left[1 + 6\frac{\rho_j(r)}{\Theta^{3/2}} + \frac{\pi^4}{3}\left(\frac{\rho_j(r)}{\Theta^{3/2}}\right)^2\right]^{-1/3}.$$

We represent the electron density in the form $\rho_j(r) = \rho_1^j(r) + \rho_2^j(r)$, where the electron density for the discrete spectrum is written out as

$$\rho_1^j(r) = \frac{1}{4\pi r^2}\sum_{n,l} N_{nl}^j (R_{nl}^j(r))^2.$$

For the continuum electron spectrum, we use the quasiclassic approximation

$$\rho_2^j(r) = \frac{\sqrt{2}\Theta^{3/2}}{\pi^2}\int_A \sqrt{y}\left\{1 + \exp\left[y - \frac{V_j(r)}{\Theta} - \frac{\mu}{\Theta}\right]\right\}^{-1} dy,$$

$$A: y > \frac{V_j(r)}{\Theta}.$$

The chemical potential $\mu$ can be determined from the electroneutrality condition

$$\sum_j W_j N_j = Z,$$

where

$$N_j = \sum_{nl} N_{nl}^j + 4\pi\int_0^{r_0} \rho_2^j(r) r^2 dr$$

is the total number of electrons in the $j$th subsystem. The concentration $W_j$ of atoms or ions corresponding to this subsystem is determined by the Gibbs distribution

$$W_j = C g_j \exp\left\{-\frac{E_j - \mu N_j}{\Theta}\right\}.$$

Here, $E_j$ is the total energy, $g_j = \prod_{nl} C_{g_l}^{N_{nl}^j}$ is the statistical weight, and $g_l = 2(2l + 1)$.

Evidently, the above set of equations cannot be solved for all plasma atoms and ions, if all possible electron configurations $\{N_{nl}^j\}$ are taken into consideration. However, this set of equations can be solved for a group of atoms and ions having the highest concentrations (the so-called basic ions). For low-concentration atoms and ions, the perturbation theory can be used. If the set of equations is solved for a group of basic ions at $j = 1, 2, \ldots, K$, this yields $K$ sets for the wave functions $\{R_{nl}^j(r)\}$ and the energy levels $\{E_{nl}^j\}$. Hence, $K$ samples of the perturbation theory can be constructed. Let, for example, we need to calculate characteristics of an ion with a set of the occupation numbers $\{\tilde{N}_{nl}\}$, the concentration $\tilde{W}$ of such ions being known to be low. Then, we can find among the basic ions those with the electron configuration $\{N_{nl}^k\}$ being the closest to the configuration $\{\tilde{N}_{nl}\}$. Let $W_k$ be also the concentration of these ions, and $\{E_{nl}^k\}$ be the set of the single-electron energy levels. Then, the concentration $\tilde{W}$ can be found from the formula

$$\tilde{W} = \frac{W_k P[\tilde{N}_{n_1 l_1}]}{P[N_{n_1 l_1}^k]},$$

where

$$P[N_{nl}] = C_{g_l}^{N_{nl}} p_{nl}^{N_{nl}} (1 - p_{nl})^{g_l - N_{nl}},$$

$$p_{nl} = \left[1 + \exp\left(\frac{E_{nl}^k - \mu}{\Theta}\right)\right]^{-1},$$

$$g_l = 2(2l + 1), \quad C_m^n = \frac{m!}{n!(m-n)!}.$$

The above formulas are presented for the simple case of the $\{N_{nl}^k\}$ configuration being different from the $\{\tilde{N}_{nl}\}$ configuration only by the occupation numbers $n_1 l_1$ of a single shell. These formulas can be generalized to a more complex case. For sufficiently large values of $g_l$, the binomial distribution transforms to the normal (Gaussian) distribution. Therefore,

$$\tilde{W} \approx W_k \frac{1}{\sqrt{2\pi}\sigma}\exp\left[-\frac{(\tilde{N}_{n_1 l_1} - N_{n_1 l_1}^k)^2}{2\sigma^2}\right],$$

for $N_{n_1 l_1}^k \approx \bar{N}_{n_1 l_1}^k \ll 1$, where $\bar{N}_{n_1 l_1}^k = g_{l_1} p_{n_1 l_1}$.

On the other hand, the spectral-line shift corresponding to the transition $(n_\alpha l_\alpha \longrightarrow n_\beta l_\beta)$ for an ion with the configuration $\{\tilde{N}_{nl}\}$ with respect to the position of this line for an ion with the configuration $\{N_{nl}^k\}$ is given by the well-known formula of the perturbation theory

$$\delta\omega_{\alpha\beta} = (\tilde{N}_{n_1 l_1} - N_{n_1 l_1}^k)(R_{n_\beta l_\beta n_1 l_1} - R_{n_\alpha l_\alpha n_1 l_1}),$$

$$R_{n l n' l'} = \iint R_{nl}^2(r)\frac{1}{r_>} R_{n'l'}^2(r_1) dr dr_1, \quad r_> = \max(r, r_1).$$

Consequently, the probability distribution function for the spectral-line shift $(n_\alpha l_\alpha \longrightarrow n_\beta l_\beta)$ has the form

$$\varphi(\delta\omega_{\alpha\beta}) \approx \frac{1}{\sqrt{2\pi}\sigma_{\text{extra}}}\exp\left[-\frac{(\delta\omega_{\alpha\beta})^2}{2\sigma_{\text{extra}}^2}\right],$$

with the variance defined by the formula

$$\sigma^2_{\text{extra}} = \sum_{nl} \tilde{W}[(\tilde{N}_{nl} - N^k_{nl})(R_{n_\beta l_\beta nl} - R_{n_\alpha l_\alpha nl})]^2.$$

Here, the summation is performed over all configurations of low-concentration ions reasonably close to the $\{N^k_{nl}\}$ ion configuration.

We now consider the shape of the spectral lines, which is associated with the Doppler effect. According to [3], this shape is determined by the expression

$$I_{\text{Doppler}}(\delta\omega_{\alpha\beta}) = \frac{1}{\sqrt{2\pi}\sigma_{\text{Doppler}}}\exp\left[-\frac{(\delta\omega_{\alpha\beta})^2}{2\sigma^2_{\text{Doppler}}}\right],$$

where $\delta\omega_{\alpha\beta} = \omega - \omega^0_{\alpha\beta}$; $\omega^0_{\alpha\beta} = E^k_\beta - E^k_\alpha$ is the spectral-line position of an ion having the electron configuration $\{N^k_{nl}\}$. For essentially imperfect plasma, the line shape determined by the Stark effect is of the form [4]

$$I_{\text{Stark}}(\delta\omega_{\alpha\beta}) = \frac{1}{\sqrt{2\pi}\sigma_{\text{Stark}}}\exp\left[-\frac{(\delta\omega_{\alpha\beta})^2}{2\sigma^2_{\text{Stark}}}\right].$$

We consider $\varphi(\delta\omega_{\alpha\beta})$, $I_{\text{Doppler}}(\delta\omega_{\alpha\beta})$, and $I_{\text{Stark}}(\delta\omega_{\alpha\beta})$ as distribution functions that present probabilities of a deviation from the spectral-line center owing to fluctuations of the occupation numbers, to the Doppler effect, and to the Stark effect, respectively. This leads us to a problem of the distribution of the total deviation caused by all these processes taken together. The solution to this problem is provided by the well-known theorem of the probability theory. According to this theorem, such a distribution will be normal provided that all three quantities have also normal distributions. As a result, we arrive at the distribution, that can be approximately considered as the line shape, for which all the three mentioned effects are taken into account:

$$I_\Sigma(\delta\omega_{\alpha\beta}) = \frac{1}{\sqrt{2\pi}\sigma_\Sigma}\exp\left[-\frac{(\delta\omega_{\alpha\beta})^2}{2\sigma^2_\Sigma}\right],$$

$$\sigma^2_\Sigma = \sigma^2_{\text{Doppler}} + \sigma^2_{\text{Stark}} + \sigma^2_{\text{extra}}.$$

An additional term $\sigma^2_{\text{extra}}$ in the second formula can be treated as a result of a certain additional broadening with respect to that caused by the Doppler and Stark effects.

We now pass to the comparison of the theoretical and experimental data. Figure 1 shows the spectral absorption coefficient $k(E)$ (cm$^2$/g) as a function of the photon energy $E$, which is calculated for germanium plasma, initially with, only the Doppler and Stark effects taken into account, and then, with inclusion of the additional broadening. The natural and electron broadening were also taken into account, but their effects turned out to be negligibly small. The theoretical and experimental data are compared in Fig. 2. The function

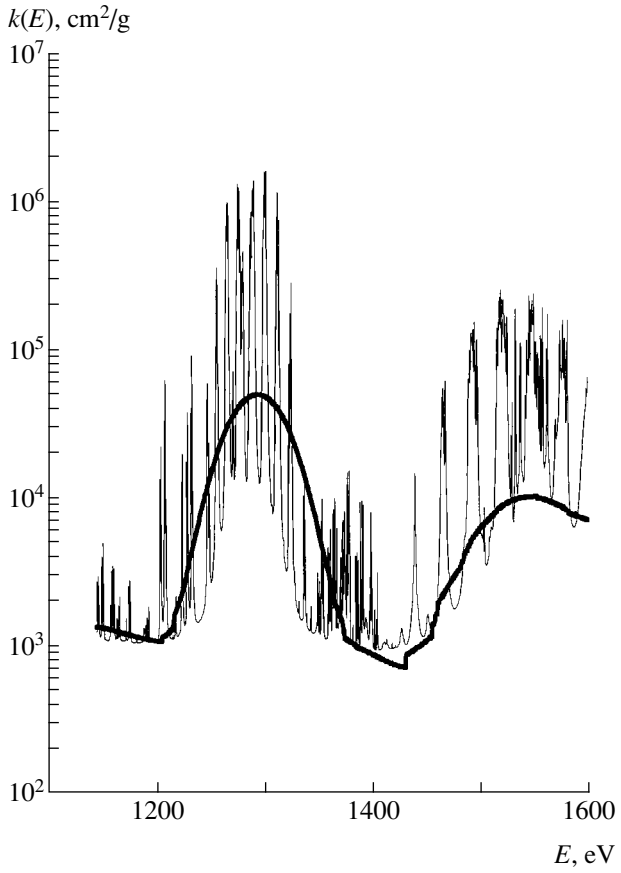


**Fig. 1.** Spectral absorption coefficient $k(E)$ calculated for germanium plasma having temperature of 76 eV and the density $\rho = 5 \times 10^{-2}$ g/cm$^3$ as a function of the photon energy $E$ with allowance for only the Doppler and Stark broadening (thin line), as well as with the additional broadening (thick line) taken into account.

$$T(E) = \exp[-k(E)\rho d],$$

with $\rho d = 1.6 \times 10^{-4}$ g/cm$^2$ was measured in the experiment [5]. The same function was calculated by the above-described procedure with the additional broadening taken into account. As is seen, the procedure proposed provides a reasonable agreement with experimental data, whereas allowance for only the Doppler and Stark effects results in a considerable disagreement with the experimental data. Indeed, in this case, the absorption coefficient is as much as $10^5$ to $10^6$ (see Fig. 1). As a result, the function $N(E)$ becomes zero in certain segments of the energy interval under consideration.

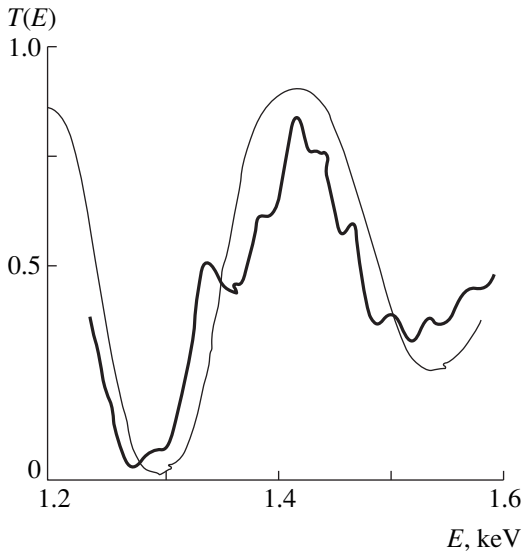


**Fig. 2.** Measured [5] (thick line) and calculated (thin line) function $T(E)$ for germanium plasma having temperature of 76 eV and the density $\rho = 5 \times 10^{-2}$ g/cm$^3$ according to the ionic model with the additional broadening taken into account.

The procedure proposed may essentially facilitate the calculations when the number of spectral lines is so large that it is impossible to take into account individual profiles for all the lines. The effect of the additional broadening must be taken into consideration if the plasma density is determined from the broadening of spectral lines.

## REFERENCES

1. N. Y. Orlov, Laser Part. Beams **15**, 627 (1997).
2. S. J. Rose, J. Phys. B, Atom. Molec. Phys. **25**, 1667 (1992).
3. I. I. Sobel'man, *Introduction to the Theory of Atomic Spectra* (Fizmatgiz, Moscow, 1963).
4. I. O. Golosnoĭ, *Allowance for an Effect of Ionic Microfields on Optic Properties of a Substance* (Moscow, 1991), No. 38.
5. J. M. Foster, Phys. Rev. Lett. **67**, 3255 (1991).

*Translated by V. Tsarev*

*Doklady Physics, Vol. 45, No. 1, 2000, pp. 11–13. Translated from Doklady Akademii Nauk, Vol. 370, No. 2, 2000, pp. 175–177.*


**PHYSICS**

# A Model of Unsteady Two-Dimensional Electron Tunneling through a Double Barrier and of Quantum Control

**Academician A. M. Dykhne, V. V. Zosimov, and A. G. Rudavets**

Received June 25, 1999

The end of the twentieth century was marked by promising achievements of mesoscopic researches, which gave impetus to an intensive development of nanotechnology. New nanostructures with desired electric properties are being purposefully synthesized in laboratories. Among such structures, nanoclusters and nanowires are of particular interest as prototypes of one-electron transistors [1–3], commutators, and tunnel diodes [4]. In molecular electronics, quantum transport properties must manifest themselves more fully in researching unsteady processes that occur in real time of electron transmission through nanoclusters. The characteristic tunneling time scale is in the femtosecond range. Therefore, for this purpose, electronic excitation and current control have to be performed by methods of the femtosecond spectroscopy. The optics of extra-short pulses also allows us to solve more complicated problems of optimizing quantum motions [5]. In particular, the aforesaid is applicable to nanoclusters in mesoscopy when the motion of an electron wave packet need be traced for investigating the electron affinity. Studying unsteady transport processes is also interesting from the viewpoint of the conventional Landauer's approach, because the packet dynamics involves exhaustive information on the tunneling-electron spectrum.

In this paper, we study the electron packet transmission through a two-dimensional double barrier. The wave packet can be formed by, for example, a extra-short laser pulse, that excites localized electrons of impurity centers into the conductivity zone. We consider a well (which an electron tunnels into) with a cylindrically symmetrical potential, which is a simplified model of carbon nanotubes referring to fullerenes.[1] The electron dynamics is described by the Schrödinger equation

$$i\frac{\partial\Psi}{\partial t} = H\Psi, \quad H = -\frac{1}{2}\Delta + V(x, y).$$

*Moscow State University, Vorob'evy gory, Moscow, 119899 Russia*

[1] Carbon nanotubes are characterized by an additional spiral symmetry of the arrangement of their walls and potential.

Here, $\Delta$ is the two-dimensional Laplacian, and $V(x, y)$ is a potential in the atomic units. A numerical solution can be found by the Trotter's method:

$$\Psi(\xi, t+\tau) = \exp(-iH\tau)\Psi(\xi, t)$$
$$= \left(\prod_{n=1}^{N}\exp(-iH\tau)\right)\Psi(\xi, 0).$$

For small $\tau = t/N$, the operator exponent is represented, with an accuracy of $O(\tau^2)$, in the form

$$\exp(-iH\tau) = \exp\left(\frac{i\tau\Delta}{4}\right)\exp(-iV\tau)\exp\left(\frac{i\tau\Delta}{4}\right).$$

Each expansion factor is evaluated in its own diagonal representation [6]. The operators of the potential and kinetic energies are diagonal in the coordinate and momentum representations, respectively. The coordinate representation transforms to the momentum one by the two-dimensional fast Fourier transformation. The electron dynamics was visualized with the time step $\tau \sim 10$ as on the torus with the dimensions $5.3 \times 10^{-9}$ cm $\times$ $5.3 \times 10^{-9}$ cm, which was covered by the net of $256 \times 256$ nodes. The initial state was taken as a wave packet of the Gaussian form with the wave vector $k = (k_x, k_y)$, at the point $\xi_0 = (x_0, y_0)$, and with the variance $d_\xi$:

$$\Psi(\xi, 0) = (\pi d_\xi)^{-1}\exp\left[-\frac{0.5(\xi-\xi_0)^2}{d_\xi^2} + ik\xi\right].$$

The potential $V(x, y)$ with the barrier height $V_0$ was taken in the form

$$V(x, y) = \frac{V_0}{2}[1 - \mathrm{sgn}(|y| - R - D)]$$
$$+ \frac{V_0}{2}[\mathrm{sgn}(r - R) - 1].$$

Here, $r = (x^2 + y^2)^{1/2}$ is the radial coordinate, $2(D + R)$ is the barrier width, and $R$ is the interior radius of the cylindrical well.

Inside the cylinder, the wave function takes the form of a nonuniform cluster, that reflects at the walls and is focused in accordance with the ray optics. The results

1028-3358/00/4501-0011$20.00 

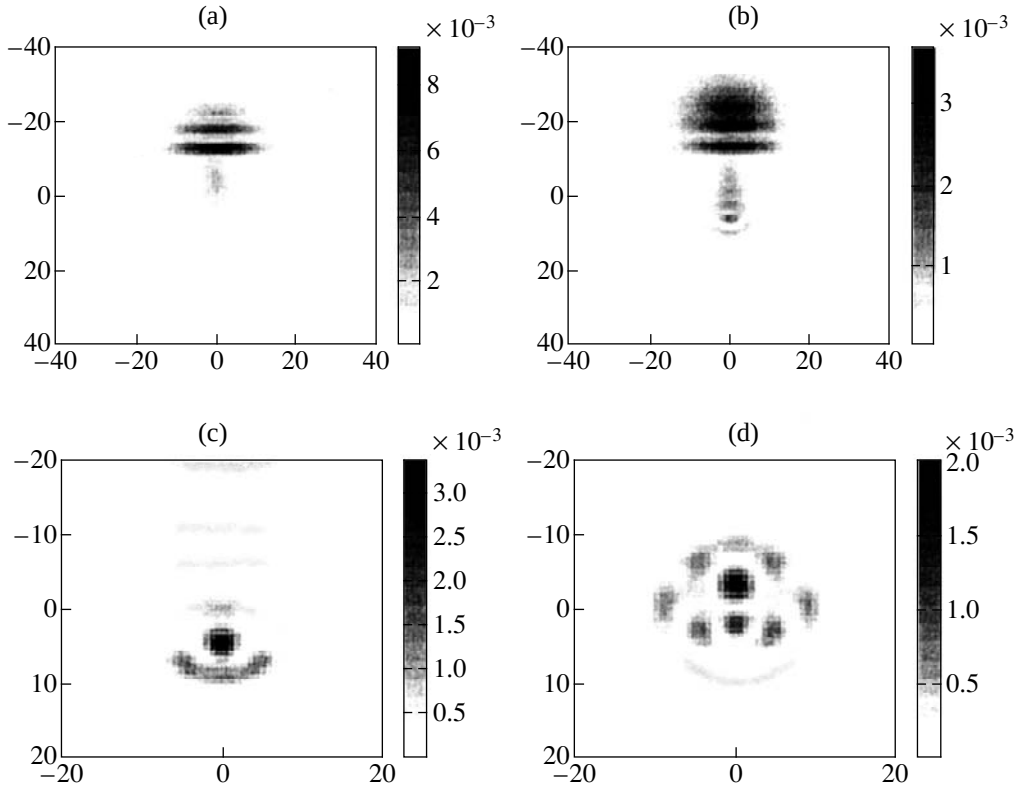


**Fig. 1.** Electron distributions at various moments $t$: (a) $t = 34$, (b) 60, (c) 40, and (d) 100. The following initial parameters of the packet are used: the variance $d = 6$, the momentum $k = 0.7$ (the energy $E = 0.245$), and the position $\xi_0 = (0, -30)$. The barrier with the height $V_0 = 0.6$ is along the lines $y = \pm 12$. The packet scatters by the barrier and tunnels into the cylindrical well with the radius $R = 10$.

of the numerical solution of the equation are shown in figure for various moments. At the moment $T = 60$, the first focus is at the distance $R/2$ from the distant boundary of the well, while, according to the paraxial approximation, the second focus is at the distance $5R/4$. The focusing is unaffected by varying the height and width of the barrier and the angle of incidence of the packet. For a fixed electron wavelength, the focal point spreads with decreasing the well radius. At the oblique incidence, the focuses shift along a circle and form an unclosed trajectory. It is worth noting that tunneling rather than above-barrier electrons are focused in this case. To make sure that such is the case, it is sufficient to carry out the spectral analysis of the solution. For the barrier with the height $V_0 = 0.6$, there are 27 eigenstates of the (quasi-)discrete spectrum, which the packet wave function can be expanded in. This set consists of three eigenstates with zero angular momentum (their radial quantum numbers are equal to 0, 1, and 2) and 12 pairs, degenerate in angular momentum, of the eigenstates with the following radial and azimuthal quantum numbers: (0, 1–7), (1, 1–3), (2, 2), and (2, 4). For the unsteady electron tunneling inside the well, the interference of these eigenstates is small.

The programmable optics allows a wave packet to be localized at a chosen point inside the well at a given moment. To do this, the initial distribution must be prepared so that the spatial harmonics compensate for the effects of quantum dispersion and scattering. A similar idea [7] has been discussed from the viewpoint of both acquiring the femtosecond coherence of electron states and the theorem of reversibility. Without going into details, we present only the final formula for the optimum packet at the initial moment:

$$\Psi(\xi, 0) = \frac{\langle \xi_f | \exp(iHt_f) | \xi \rangle}{\sqrt{\lambda}}.$$

This packet has the maximum overlap with the delta-function kernel at the point $\xi_f$ at the moment $t_f$. Here, $\langle \xi_f |$ and $| \xi \rangle$ are the bra- and cket-vectors at the point of localization and at a moving coordinate, respectively. The normalizing parameter $\lambda$ acts as a Lagrange multiplier in the functional of quantum control.

The above results are applicable for an arbitrary potential and hold for the focusing of an electron wave packet when it tunnels through nanoclusters. The packet localization occurs together with the opalescent scattering (which is the well-known quantum-mechanical and optical effect) and with the shining outside the cluster. It is worth noting once again that this quantum process is reversible. The scattered waves can be local-

ized at a chosen point by optimizing the phase modulation of the initial state. The incident wave packet must contain the spatial harmonics that are conjugate in phase with respect to the scattered waves. The inversion of the electron wave front is a necessary condition for the localization.

Studying the tunneling dynamics is of interest due to a number of reasons. First of all, it stimulates the development of the scanning tunneling microscopy, spectroscopy, and defectoscopy with the space-time resolution inside clusters. Further development of both the theory and experiment in the direction outlined will allow us to understand the character of the electron affinity in clusters and to trace the formation of anions, the reorganization of molecular structures, and the relaxation processes inside clusters.

## ACKNOWLEDGMENTS

This work was supported in part by the Russian Foundation for Basic Research, projects no. 96-02-17782 and no. 99-02-18349.

## REFERENCES

1. E. S. Soldatov, V. V. Khanin, A. S. Trifonov, *et al.*, Pis'ma Zh. Éksp. Teor. Fiz. **64**, 510 (1996) [JETP Lett. **64**, 556 (1996)].
2. E. S. Soldatov, V. V. Khanin, A. S. Trifonov, *et al.*, Usp. Fiz. Nauk **168**, 217 (1998) [Phys.–Usp. **42**, 202 (1998)].
3. A. Bezryadin, A. R. M. Verschueren, S. J. Tans., *et al.*, Phys. Rev. Lett. **80**, 4036 (1998).
4. S. J. Tans, A. R. M. Verschueren, and C. Dekker, Nature (London) **393**, 49 (1998).
5. A. M. Dykhne, S. Yu. Vasil'ev, O. A. Petriĭ, *et al.*, Dokl. Akad. Nauk **368**, 467 (1999) [Dokl. Phys. **44**, 653 (1999)].
6. B. Kohler, V. V. Yakovlev, J. Che, *et al.*, Phys. Rev. Lett. **74**, 3360 (1995).
7. C. J. Bardeen, V. V. Yakovlev, K. R. Wilson, *et al.*, Chem. Phys. Lett. **280**, 151 (1997).
8. M. J. Feit, J. A. Fleck, and A. Steĭger, J. Comput. Phys. **47**, 412 (1982).
9. V. M. Akulin, V. A. Dubovitskiĭ, A. M. Dykhne, *et al.*, J. Phys. Chem. **102**, 4310 (1998).

*Translated by V. Chechin*

*Doklady Physics, Vol. 45, No. 1, 2000, pp. 14–17. Translated from Doklady Akademii Nauk, Vol. 370, No. 3, 2000, pp. 328–331.*


**PHYSICS**

# Shock-Wave Carbyne Synthesis from Graphite

**A. Z. Zhuk, T. I. Borodina, V. V. Milyavskiĭ, and Academician V. E. Fortov**

Received August 16, 1999

Nowadays, there are two basic methods for obtaining Carbyne, i.e., the allotropic form of carbon with $sp^1$ hybridization of atomic orbitals [1]. These methods are dehydrohalogenation of certain halogen-containing polymers (chemical method) and carbon precipitation from the gaseous phase. The first method usually results in obtaining the amorphous substance with high impurity content exceeding 10%. The precipitation from the gaseous phase allows thin films ordered in two dimensions and having the maximum thickness of ~10 μm to be obtained. However, in most cases, only sufficiently large Carbyne crystals (of no less than submillimeter dimensions) can be of interest for practice.

It seems to be natural to make an attempt of Carbyne synthesizing based on a thermodynamic approach, i.e., to use a method similar to that realized while synthesizing artificial diamonds from graphite. In this case, it is necessary to choose such pressures and temperatures at which the direct graphite–Carbyne phase transition could be realized. For both these values being sufficiently close to the line of graphite–Carbyne equilibrium and a sufficiently long duration of the process, we would expect formation of relatively large Carbyne crystals with well-ordered structure.

Previously, A.G. Whittaker [2], and R.B. Heĭmann *et al.* [3] made attempts of synthesizing Carbyne using compression or thermal action. Heating a graphite sample up to temperature of 2600–2800 K by direct action of electric current, Whittaker [2] has succeeded in obtaining a certain (seemingly, small) amount of Carbyne.

The authors of [3] used graphite preliminarily heated up to temperature of 2900 K for shock compressing at pressures up to 15–25 GPa. They discovered Carbyne traces conserved in the samples.

Recently, we took part in an attempt to synthesize Carbyne from graphite by using a laser-induced shock. The results of the experiments are published in part elsewhere [4]. The laser-pulse duration was ~600 ps, and the maximum pressure in the graphite varied within the range 12 to 32 GPa. Carbyne crystals, whose dimensions varied within the limits from 1 to 30 μm, were found both in the focal spot and around it. Carbyne structure was essentially different in these two regions. Therefore, it was assumed that in the focal spot, Carbyne was formed in the cycle of compression, while outside this spot, its formation occurred owing to precipitation of the carbon that had vaporized during the irradiation. In the region subjected to the action of the laser beam, surface temperature of the sample material is estimated to be higher than 3800 K.

The data presented above justify an assumption that, at certain temperatures and pressures, crystalline Carbyne can be obtained directly from graphite. However, data available are insufficient to optimize the dynamic synthesis (i.e., to determine conditions of the maximum Carbyne yield) and to estimate a possibility of static Carbyne synthesizing.

The goal of this study is to refine the conditions (i.e., pressure and temperature) of dynamic Carbyne synthesis from graphite and searching for technological approaches to commercial synthesis of crystalline Carbyne.

The MGP-RD-60 graphite with the density of $2.20 \pm 0.05$ g/cm$^3$ and of the monochromator quality was used in the experiments. The impurity content was lower than 0.5 at. %. Figure 1a shows a diffraction pattern of the original sample.

In the shock-wave experiments, we applied a plane steel recovery ampoule that had been described in detail in [5]. A graphite sample was placed into the ampoule between two 2 mm-thick disks each 10 mm in diameter, which were made of copper or Teflon. The assembly was subjected to impacts of a 10 mm-thick aluminum plate 90 mm in diameter, which was accelerated up to 2.5 km/s as a result of detonation of an explosive. The shock wave propagated in the direction of the graphite *c*-axis. The shock pressure in the sample was attained in the course of several wave circulations between steel walls of the ampoule and amounted to ~35 GPa.

We have realized two variants of the experiment with the impact loading. In the first of them, graphite foils 10 to 15 μm thick and with characteristic dimensions of 5 to 7 mm were placed between copper disks. In the second variant, the graphite foils were fixed between the Teflon disks. According to our estimates, duration of the loading was such, that the foils and the

*Research Center for Thermal Physics of Pulse Actions, Russian Academy of Sciences, Izhorskaya ul. 13/19, Moscow, 127412 Russia*

1028-3358/00/4501-0014$20.00 

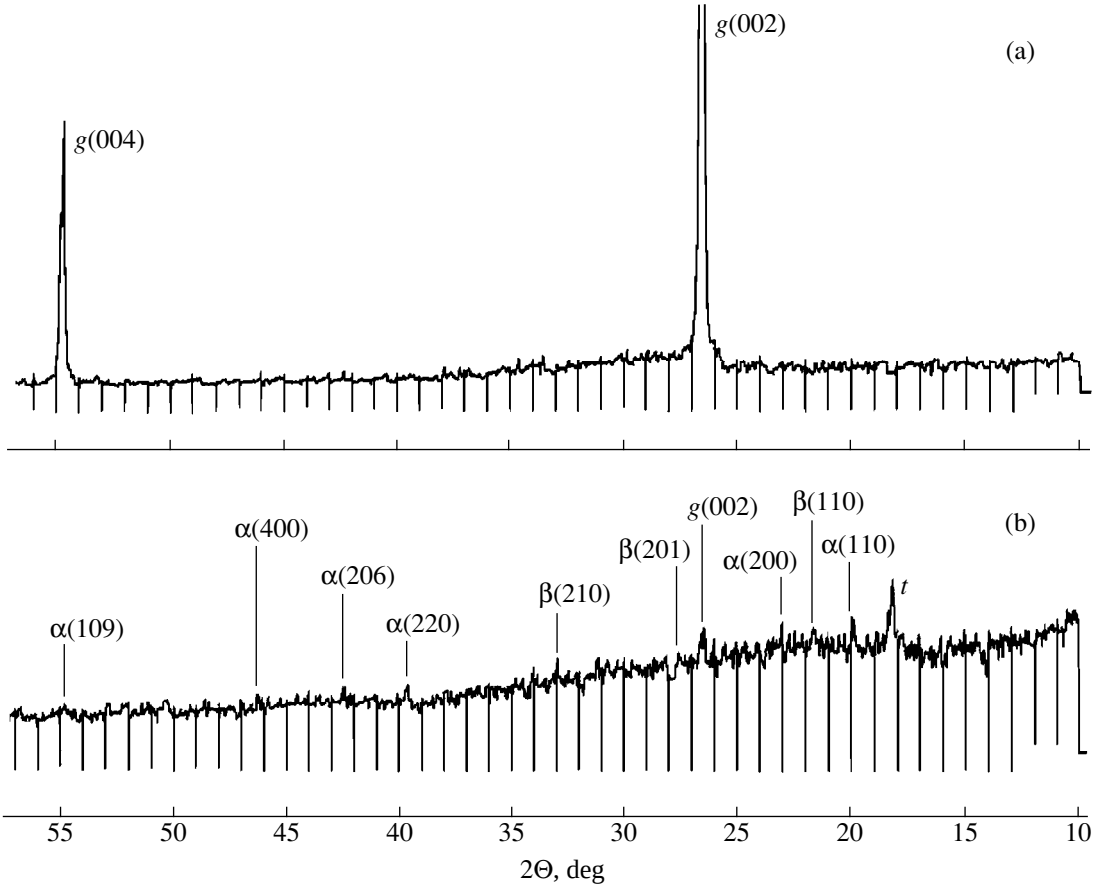


**Fig. 1.** X-ray pattern for (a) the original graphite film and (b) the material conserved after the impact loading. Letters *t*, α, β, and *g* correspond to Teflon, α-Carbyne, β-Carbyne, and graphite, respectively (the numbers in parentheses correspond to Miller indices; Θ is the Bragg angle).

disks had enough time to turn out in a state close to the thermal equilibrium. In addition, we carried out similar experiments with massive (~1 mm thick) graphite samples.

The structure of the conserved samples was investigated by the method of X-ray diffractometry with the help of the DRON-3M setup using Cu$K_\alpha$ emission line. Carbyne was not found in the samples of the first group (i.e., after loading in the copper container). The major part of graphite crystals retained its original orientation. We detected a small number of fine-grained cubic diamonds as well. The results of the experiment, as a whole, coincide with the data obtained previously in the experiments with massive samples of the MGP-RD-60 graphite [5].

Figure 1b shows the diffraction spectrum of graphite subjected to shock compression in the Teflon container. Although the film with the original diffraction pattern contains only diffraction lines intrinsic to graphite, the diffraction spectrum of the material after the impact loading includes, in addition to these lines, diffraction maxima corresponding to α- and β-Carbyne and Teflon. Low intensity of these lines is explained by rather small surface area of the fragments under investigation.

Comparing intensities of the recorded Carbyne diffraction lines obtained with the corresponding maxima of the crystalline α-Carbyne reference sample [6], we may conclude that, after the impact loading, the major part of Carbyne is in the crystalline state. For different fragments of the sample, the bulk content of crystalline Carbyne should be estimated as 60 to 80 vol. %. This value is uniquely high for the direct graphite–Carbyne synthesis. The amount of crystalline graphite does not exceed 5%.

The enhanced (with respect to the standard level) intensity of the (220) and (440) lines of α-Carbyne reveals the existence of a preferable orientation of α-Carbyne crystals synthesized in the experiment. The *c*-axes of the α-Carbyne crystals are preferably parallel to the basal plane of the original graphite. This fact agrees with the assumption that, in our experiments, Carbyne is formed via single bond opening in the graphite basal plane [7].

While loading massive graphite samples in the Teflon container, Carbyne formed there only in a thin

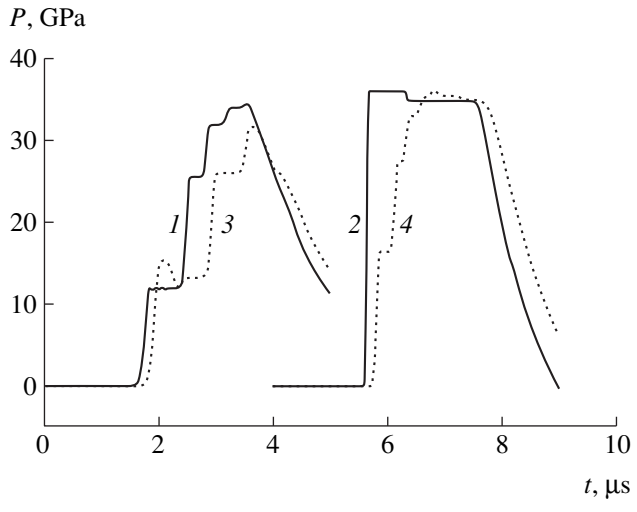


**Fig. 2.** Profiles for pressures in the container material while shock loading: (*1*) Teflon container and (*2*) copper container (at the surface of the graphite foil); (*3*) Teflon container and (*4*) copper container (in the middle parts of massive graphite samples).

near-surface layer. After loading, the middle part of the sample consisted only of original graphite.

Figure 2 shows pressure profiles calculated for the graphite foil fixed between two Teflon (curve *1*) and copper (curve *2*) disks. For comparison, the same figure presents pressure profiles in the middle parts of the 2 mm-thick massive graphite samples during their loading in the Teflon (curve *3*) and copper (curve *4*) containers. The calculations were carried out in the one-dimensional hydrodynamic approximation. To describe thermodynamic properties of the substances, we used wide-range equations of state presented in [8] (for Teflon), [9] (for Al, Fe, and Cu), and [10] (for graphite).

We think that it is the higher temperature of the sample (compared to its values in other our experiments) that can be one of possible reasons for appearance of crystalline Carbyne when the Teflon container is used for impact loading the thin graphite film.

Over the entire pressure range realized in our experiments, the temperature of single shock compression of Teflon [11] exceeds essentially those of graphite [10] and copper [12]. For example, temperatures arising when single shock compressing Teflon, graphite, and copper up to 10 GPa attain 570, 380, and 335 K, respectively. At a pressure of 40 GPa, they are 1960, 960, and 570 K. Being placed in the recovery ampoule, both the container and the sample are subjected to stepwise compression during which the maximum pressure in the sample is attained after several motions of a shock wave inside the container. Under such conditions, the temperature is determined mainly by heating the substance in the first shock. Pressures $P_1$ and temperatures $T_1$ in the first shock wave, as well as the maximum temperature $T_{max}$ attained for various materials of the sample and container are presented in the table.

**Table**

| Parameters | Graphite in the Teflon container | | Graphite in the copper container | |
|---|---|---|---|---|
| | Teflon | graphite | copper | graphite |
| $P_1$, GPa | 11.9 | 15.3 | 36.0 | 16.4 |
| $T_1$, K | 645 | 470 | 515 | 485 |
| $T_{max}$, K | 730 | 495 | 515 | 520 |

The maximum temperature of the graphite shock compression was calculated directly from the equation of state [10]. When the copper plates are used for fixing graphite during its shock compression, the maximum temperature $T_{max} = T_1 \approx 515$ K of the container material is attained in the first shock. The Teflon container is heated additionally by the repeated-compression waves, so that $T_{max} = T_1 + \Delta T$. An increment of Teflon temperature can be estimated as $\Delta T \approx \Delta E_T/C_V$. Here, $\Delta E_T$ is an increment of the thermal part of the specific internal energy during repeated compressions, which is calculated by the equation of state taken from [8], and $C_V$ is the specific heat at a constant volume. For the given temperature range, the specific heat of Teflon $C_V$ satisfies the inequality $0.65 < C_V/(3Rn/\mu) < 1$ (see [11]), where $R = 8.31$ J/(mol K), $\mu = 50.01$ g/mol is the mole mass of the ($-CF_2-$) monomer, $n = 3$ is the number of monomer atoms, and the value 0.65 corresponds to the standard conditions of environment. As a result, we have $71 < \Delta T < 109$ K, and the maximum temperature of the Teflon container is estimated to be $T_{max} \approx 730 \pm 20$ K.

In the conditions of our experiments, it is the temperature of a container that determines temperature of the graphite foil. Thus, being loaded in the Teflon container, the 10-μm-thick graphite sample has temperature exceeding approximately by 200 K that of graphite in other our experiments. Therefore, the graphite–Carbyne transformation can be realized via shock compression at a pressure of ~35 GPa and the temperature ~730 K. In this case, the transformation efficiency can reach 80%.

Figure 3 shows the equilibrium diagram for carbon, which corresponds to [13]. The known data concerning conditions, for which synthesis of Carbyne from graphite occurs, occupy two regions in this diagram. The temperatures taken from [3, 4] are close to the temperature range that, in Whittaker's opinion [2], bounds a zone of Carbyne thermodynamic stability. The parameters of dynamic synthesis of Carbyne, which are obtained by us, correspond to the temperature interval in which crystallization of amorphous Carbyne at atmospheric pressure was observed [6, 14].

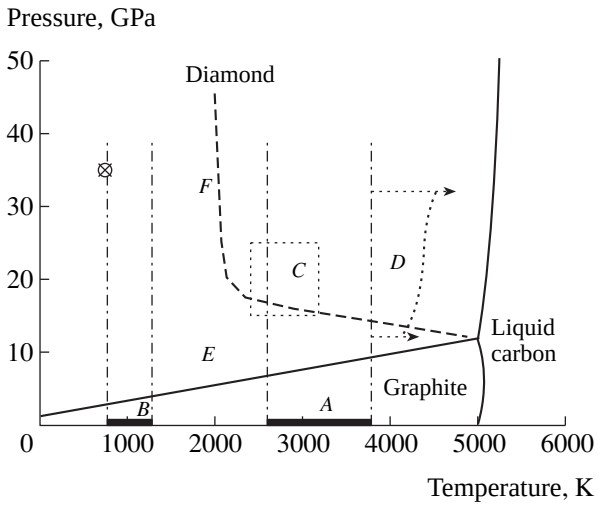


**Fig. 3.** Equilibrium diagram for carbon according to [13]. Zones denoted by letters correspond to: (*A*) the Carbyne thermodynamic stability [2] and (*B*) amorphous-Carbyne crystallization [6, 14]. Zones (*C*) [3], (*D*) [4], and ⊗ (this study) correspond to the parameters of synthesizing crystalline Carbyne from graphite. Zones (*E*) and (*F*) relate to catalytic synthesizing diamonds [13] and the lower boundary for the parameters of the dynamic synthesizing cubic diamonds [13].

We assume that mechanisms of Carbyne formation are different for high and low temperatures.

At 3000–4000 K, the basic mechanism governing the Carbyne formation, most likely, is the precipitation of carbon clusters, which occurs from the gaseous phase formed in the course of the experiment.

In the experiments described in this paper, Carbyne formation, in our opinion, occurs via opening a single bond in the graphite basal plane. Dynamic compression of graphite up to pressures exceeding ~20 GPa [13] causes decomposition of the graphite crystal lattice, changes the type of electron bonds in carbon atoms, and leads to formation of nucleation centers of Carbyne crystals. Annealing at the temperature of ~730 K causes the formation of sufficiently stable Carbyne crystals [6, 14] capable of surviving after both removal of the excess pressure and lowering the temperature.

In our experiments, graphite was heated up to temperature exceeding that of its shock compression due to the heat flux coming from the hotter Teflon disks. Evidently, this way allows only thin Carbyne samples to be obtained. For synthesizing massive polycrystalline samples, apparently, it is advisable to heat previously a massive graphite sample up to temperature of ~600 K at standard pressure. Then, in the course of subsequent impact loading and heating, the sample temperature can attain the value required for a sufficiently high-level transformation. From the industrial standpoint, such a technology of the polycrystalline– Carbyne production seems to be quite realizable.

The data obtained raise hopes of finding conditions for static Carbyne synthesis, which is necessary for obtaining large Carbyne crystals. Comparing conditions for shock-induced and static syntheses of artificial diamonds, we hope that, in the case of Carbyne, thermodynamic parameters of the static synthesis will also be much lower than those at which the phase transition occurs during the shock compression.

## REFERENCES

1. Yu. P. Kudryavtsev, S. E. Evsyukov, M. B. Guseva, *et al.*, Izv. Akad. Nauk SSR, Ser. Khi., No. 3, 450 (1993).
2. A. G. Whittaker, Nature (London) **276**, 695 (1978).
3. J. Kleĭman, R. B Heĭmann, D. Hawken, and N. M. Salansky, J. Appl. Phys. **56**, 1440 (1984).
4. V. M. Babina, M. Boustie, M. B. Guseva, *et al.*, Teplofiz. Vys. Temp. **37**, 573 (1999).
5. A. Z. Zhuk, T. I. Borodina, V. E. Fortov, *et al.*, High Pressure Res. **15**, 245 (1997).
6. T. I. Borodina, V. E. Fortov, A. A. Lash, *et al.*, J. Appl. Phys. **80**, 3757 (1996).
7. R. B. Heĭmann, Diamond Relat. Mater., No. 3, 1151 (1994).
8. K. V. Khishchenko, Candidate's Dissertation in Physics and Mathematics (Moscow, 1996).
9. S. Yu. Gus'kov, V. B. Rozanov, and M. A. Rumyantsev, Preprint no. 28, FIAN (Lebedev Institute of Physics, Russian Academy of Sciences, Moscow, 1996).
10. A. B. Averin and A. T. Sapozhnikov, Khim. Fiz. **16**, 70 (1997).
11. C. E. Morris, J. N. Fritz, and R. G. McQueen, J. Chem. Phys. **80**, 5203 (1984).
12. M. V. Zhernokletov, V. N. Zubarev, R. F. Trunin, and V. E. Fortov, *Experimental Data on Impact Compressibility and Adiabatic Expansion of Condensed Substances at High-Energy Density* (Chernogolovka, 1996).
13. F. P. Bundy, W. A. Basset, M. S. Weathers, *et al.*, Carbon **34**, 141 (1996).
14. M. B. Guseva, N. F. Savchenko, and V. G. Babaev, Dokl. Akad. Nauk **283**, 1336 (1985) [Sov. Phys.–Dokl. **30**, 686 (1985)].

*Translated by Yu. Verevochkin*

*Doklady Physics, Vol. 45, No. 1, 2000, pp. 18–21. Translated from Doklady Akademii Nauk, Vol. 370, No. 3, 2000, pp. 332–335.*


**PHYSICS**

# Metal-Ceramic Cathodes for Electron Accelerators

**Corresponding Member of the RAS Yu. A. Kotov, E. A. Litvinov, S. Yu. Sokovnin, M. E. Balezin, and V. R. Khrustov**

Received June 23, 1999

**1.** Nanosecond pulse generators with the pulse recurrence frequency as high as 1 kHz and the resource up to $10^{10}$–$10^{11}$ pulses and electron accelerators with such generators [1, 2], which are of considerable promise for technological applications [3, 4], have been developed on the basis of semiconductor current switches. In connection with this, the problem of creating simple, inexpensive, and high-resource cathodes with high and stable emissivity in the course of the exploitation becomes urgent. Metal–dielectrics–metal cathodes [5], in which electrons are emitted from plasma arising at a point of contact of special electrodes with ceramics (triple points), most fully conform to these requirements. Among disadvantages of these cathodes are a complexity of the structure and limited number of emitting points. This causes the erosion of igniting electrodes and the ceramics under them, a inhomogeneity in the current distribution at the output foil of a vacuum diode, and a reasonably high impedance of the diode for small dimensions of the cathode unit.

For creating plasma, we propose to use a metal-ceramic cathode, which consists in ceramics with metallic particles uniformly distributed over the cathode volume. The first results of investigating the emissive characteristics of such cathodes are presented in this study.

**2. Experimental procedure.** We used the frequency nanosecond electron accelerator URT-0.5 [6] with the accelerating voltage $U \le 500$ kV, the pulse half-width $t_p = 50$ ns, the voltage-pulse rise time $t_{f\,0.1–0.9} = 40$ ns, the response frequency $f \le 200$ Hz, and the maximum pulse power $W \le 130$ MW.

In experiments, we measured the accelerating voltage $U_a$ across the vacuum diode by means of a potentiometer-type voltage divider, the total current $I_D$ and the anode current $I_A$ in the vacuum diode by means of current transformers, and the power of the absorbed dose of bremsstrahlung by means of the pin-diode SKD1-02. The shape and the current distribution of the electron beam were detected by dosimetric films of the TsDP-2-F2 type [7], which were tightly superimposed on the output foil of the diode and processed after the exposure using the densitometer IFO-463.

As a cathode, we used ceramic plates prepared in the Institute of Electrophysics, Ural Division of the Russian Academy of Sciences on the basis of $Al_2O_3$ powders with spherical 12Kh18N10T-steel particles 26 μm in diameter, which were uniformly distributed over the plate's volume. The density of these particles on the surface was ~4300 $cm^{-2}$, the plate thickness was 2 mm, and the diameter was 12.2 mm. The plate edge was polished, and the plate was glued by a paste (cyatine) to the cathode holder (see Fig. 1), $h = 10$ mm.

**3. The principal experimental results.** The processing of the oscillograms obtained (Fig. 2) enabled us to establish the following features.

There is a time delay $t_d$ between the arrival time of the voltage pulse and the onset of the current pulse. It was established that $t_d$ does not vary with the cathode–anode separation over the range $d = 30$–$90$ mm and amounts to ~20 ns.

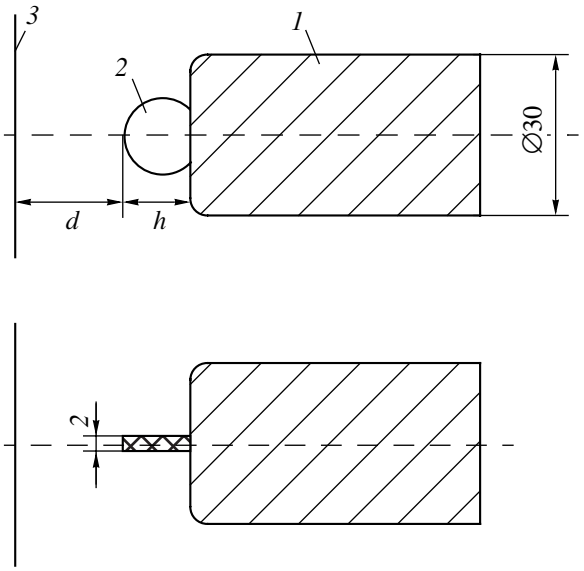


**Fig. 1.** Structure of a metal-ceramic cathode (two projections): (*1*) cathode holder; (*2*) ceramic plate; (*3*) anode.

*Institute of Electrophysics, Ural Division, Russian Academy of Sciences, Komsomol'skaya ul. 34, Yekaterinburg, 620219 Russia*

1028-3358/00/4501-0018$20.00 

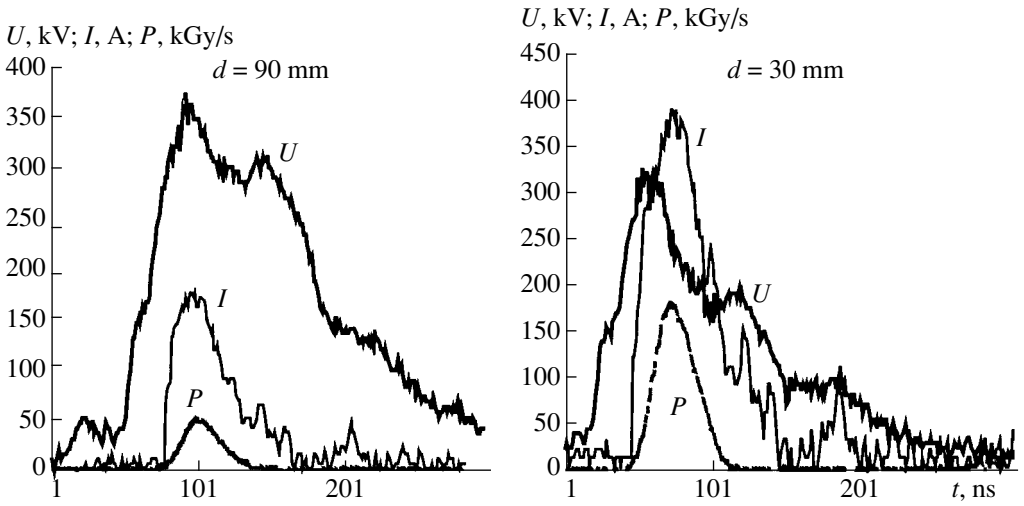


**Fig. 2.** Voltage $U$ across the vacuum diode; the anode current $I_a$ in the vacuum diode and the power $P$ of the absorbed dose of bremsstrahlung for various values of the anode–cathode separation $d$ for the metal-ceramic cathode.

The application of the metal-ceramic cathode leads to increasing the rate of rise of the electron-beam current and the output power $P$ of the accelerator. It was also established that, for a constant voltage-rise rate $\frac{dU}{dt} \sim 5 \times 10^{12}$ V/s, $\frac{di}{dt}$ attains the value $3 \times 10^{10}$ A/s in the region of the maximum power for the X-ray radiation, $d = 30$ mm (Fig. 3), and the rate of rise for the electron-beam power amounts to $\frac{dP}{dt} \sim 2 \times 10^{15}$ W/s in this case, whereas we did not obtain $\frac{di}{dt} > 5 \times 10^9$ A/s and $\frac{dP}{dt} > 2.5 \times 10^{13}$ W/s [8] with the metal–dielectrics–metal cathodes.

The voltage corresponding to the onset of the current is virtually independent of the cathode–anode separation over the range $d$ = 30–90 mm and amounts to $U \sim 250$ kV.

From comparing the dependencies of the diode impedance and the accelerator power corresponding to the moment of the maximum current (Fig. 3), it is possible to conclude that the emissivity of the cathode does not restrict the output power of the accelerator: in the region $d$ = 30 mm, the accelerator power attains its maximum, and the current continues to grow for smaller $d$ owing to a proportional decreasing the voltage, while the power remains virtually unaltered (within a certain region of $d$ values).

The shape of the beam imprint on the detector is an ellipse (the ratio of the axes is ~5 : 7), whose longer axis lies in the plane of the metal-ceramic plate. The distribution of the anode current (along the short axis, see Fig. 4) shows that, even for relatively small $d$, the beam is distributed unexpectedly uniformly; this fact invokes no explanations until now. For $d$ = 10 mm, the current density at the anode amounts to $24.3 \pm 8\%$ A/cm$^2$. The uniformity increases with $d$. A reasonably sharp boundary of the beam and its large dimension with respect to those of the cathode also engage our attention.

**4. Discussion of the results.** We estimate the electric-field intensity near the metallic particles embedded into the dielectrics. On the basis of the geometry of the diode and the cathode unit presented in Fig. 1, it is felt that, in our case, the field strength $E_1$ in the ceramics lies in the range between the corresponding values for a dielectric ball in an external uniform field and a perpendicular dielectric cylinder [9, 10]:

$$\frac{3}{2\varepsilon + 1}\frac{U}{d + h} > E_1 > \frac{2}{\varepsilon + 1}\frac{U}{d + h}. \quad (1)$$

Here, $\varepsilon$ is the relative dielectric constant of the metal-

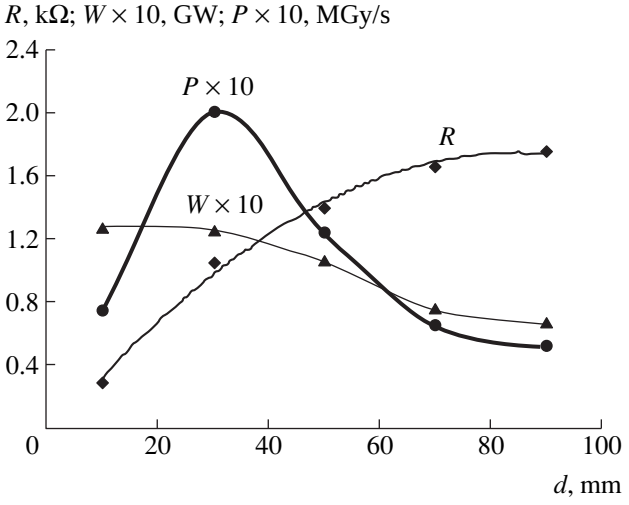


**Fig. 3.** Impedance $R$, output power $W$, and bremsstrahlung-dose power $P$ for various separations $d$.

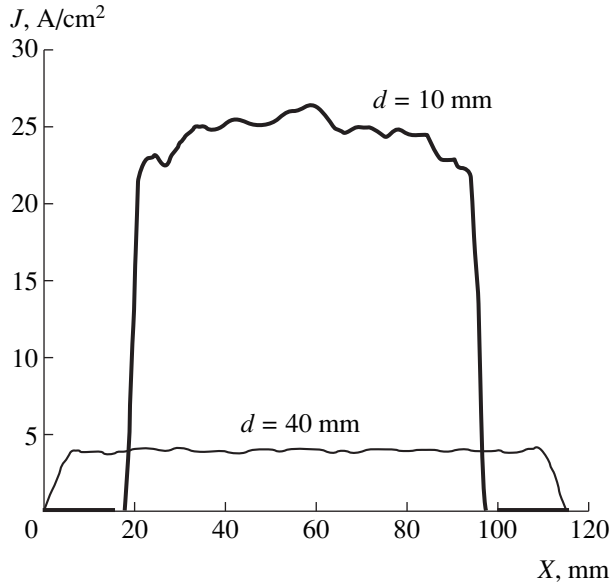


**Fig. 4.** Integral distribution of the electron-beam current at the anode for various separations *d*.

ceramic plate, and $U$ is the voltage across the diode. The dimensions of the metallic particles are ~$10^{-3}$ cm, the surface density of these particles is $4.3 \times 10^3$ cm$^{-2}$; consequently, a mean separation between the particles is ~$10^{-2}$ cm. It follows from these estimates that the particles are electrostatically independent. The field near a particle can be estimated [9, 10] as

$$E_2 = 3E_1 \cos\theta, \tag{2}$$

where $\theta$ is the angle between the direction of $E_1$ and that of the radius vector drawn from the particle center.

As can be seen from the oscillograms for the voltage and the current, a sharp current rise lags behind the voltage rise. The delay time is ~$3 \times 10^{-8}$ s. At this stage, the current is small and can stem from the bias currents in the metal-ceramic plate owing to a reasonably high voltage-rise rate. A sharp rise of the current implies that a conducting medium (plasma) is generated on the surface of the metal-ceramic plate, and the plasma provides a high emissivity of the cathode.

The bias currents can not provide decomposition of condensed media, a metal or dielectrics, to the plasma state because the bias-current density is

$$j_1 = (4\pi)^{-1}\frac{dE_3}{dt}$$

$$= \frac{6\pi}{4\pi(\varepsilon + 1)}(d + h)^{-1}\frac{dU}{dt} \approx 0.58 \ \frac{\text{A}}{\text{cm}^2}. \tag{3}$$

The thermionic field emission from metallic particles on the surface of the metal-ceramic plate is also impossible because the metallic particles are electrically insulated with respect to the charge.

In this situation, it is natural to assume that plasma is generated as a result of developing a gas discharge in micropores between the dielectrics and the metal, similarly to that proposed in studies [11, 12]. This conclusion is suggested by both the similarity of the voltage–current characteristics found from our oscillograms to the characteristics taken from the studies [11, 12], and the electric-field intensity $E_3 = \varepsilon E_2$ in the micropores and its dependence on $d$ (the so-called total-voltage effect) found from our data to that found from the study [11] for the moment of the onset of the sharp current rise. The plasma generated in the micropores, that emerge at the surface of the metal-ceramic plate, can provide the necessary electron emission and the electric contact with a metallic cathode holder.

The micropores can arise during the process of preparing the metal-ceramic plates owing to a difference in the temperature coefficients of linear expansion (the temperature coefficients of linear expansion are equal to 23 K$^{-1}$ at 1300 K and 17.6 K$^{-1}$ at 373 K for the 12Kh18N10T steel, and $9.8 \times 10^{-6}$ K$^{-1}$ at 1400 K and 8.1 K$^{-1}$ at 400 K for $Al_2O_3$ [14]). When a sintered cermet material is cooled, micropores arise between the metallic particles and the ceramics; these micropores are filled by a gas, which is just the working substance for generating plasma once the necessary electric-field intensity has been attained on the surface of metallic particles. On the basis of the numerical data presented above, we can estimate the cross dimensions of the micropores as $10^{-6}$–$10^{-5}$ cm, the field intensity $E_3$ as ~ $6 \times 10^5$ V/cm, and the gas concentration as $10^{19}$–$10^{20}$ cm$^{-3}$. A characteristic of the discharge development can be determined to a large degree by the processes at electrodes (micropores) and has the properties of the high-frequency discharge. We are not familiar with any results of a comprehensive studying such types of gas discharges. It seems likely that the purposeful work along this line will be necessary. It is not improbable also that, in our case, a certain role is played by a release of the Joule heat caused by the fluctuation electromagnetic field [15].

**5.** Thus, the type of the cathode tested has a number of attractive characteristics (the power sharpening, the uniform current distribution, and a high emissivity), which show that further investigations are required.

## ACKNOWLEDGMENTS

The authors thank A.M. Murzakaev for the photographs of the metal-ceramic cathodes, O.M. Samatov and I.V. Beketov for the preparation of necessary powders, and V.M. Tel'nova for the preparation of a mixture of ceramic and metallic powders.

The authors thank also the Foundation INCO COPERNICUS for partial financial support of this work on the contract NIC no. IC15-CT97-0713 (DG12-SNRD).

## REFERENCES


1. Yu. A. Kotov, G. A. Mesyats, S. N. Rukin, *et al.*, Dokl. Akad. Nauk **330**, 315 (1993) [Phys.–Dokl. **38**, 229 (1993)].
2. Yu. A. Kotov, G. A. Mesyats, S. N. Rukin, *et al.*, in *Digest Techn. Papers. IX IEEE Pulsed Power Conf.* (Albuquerque, N. M., USA, 1993), Vol. 1, p. 134.
3. Yu. A. Kotov, G. A. Mesyats, S. R. Korzhenevskiĭ, *et al.*, in *Proceedings of the X IEEE Pulsed Power Conf.* (Santa Fe, N. M., USA, 1995), p. 1231.
4. Yu. A. Kotov and S. Yu. Sokovnin, Prib. Tekh. Éksp., No. 4, 84 (1997).
5. S. P. Bugaev, V. A. Ilyushkin, E. A. Litvinov, *et al.*, Zh. Tekh. Fiz. **43**, 2138 (1973) [Sov. J. Tech. Phys. **43**, 1343 (1973)].
6. Yu. A. Kotov, S. Yu. Sokovnin, in *Abstracts XII Intern. Conf. High Power Part. Beams* (Haifa, Israel, 1998), p. 5.
7. V. V. Generalova and M. N. Gurskiĭ, *Dosimetry in Radiation Technology* (Izd. Standartov, Moscow, 1981).
8. Yu. A. Kotov, S. Yu. Sokovnin, and M. E. Balezin, in *Abstracts XII IEEE Intern. Conf. Pulsed Power* (Monterey, Calif., USA, 1990).
9. L. D. Landau and E. M. Lifshits, *Electrodynamics of Continues Media* (Nauka, Moscow, 1982; Pergamon Press, New York, 1960).
10. W. Smythe, *Static and Dynamic Electricity* (New York, 1950; Inostrannaya Literatura, Moscow, 1954).
11. N. V. Tatarinova, Preprint No. 067-89, MIFI (Moscow Institute of Engineering Physics, 1988).
12. B. S. Kul'varskaya and N. V. Tatarinova, Radiotekh. Électron. **37**, 362 (1992).
13. N. V. Tatarinova, N. E. Novikov, and V. S. Sokolov, Izv. Akad. Nauk SSSR, Ser. Fiz. **56** (7), 64 (1992).
14. *Physical Quantities. Handbook*, Ed. by I. S. Grigor'ev and E. Z. Melikhov (Énergoizdat, Moscow, 1991), pp. 235, 240.
15. I. A. Dorofeev, Zh. Tekh. Fiz. **67** (11), 70 (1997) [Tech. Phys. **42**, 1305 (1997)].


*Translated by V. Bukhanov*

*Doklady Physics, Vol. 45, No. 1, 2000, pp. 22–24. Translated from Doklady Akademii Nauk, Vol. 370, No. 3, 2000, pp. 336–338.*


**PHYSICS**

# Relativistic Electron in the Field of Finite Electric Dipole

**V. I. Matveev, D. U. Matrasulov, M. M. Musakhanov, and Corresponding Member of the RAS P. K. Khabibullaev**

Received April 7, 1999

The problem on electron motion under the action of finite electric dipole ranked among classic problems of nonrelativistic quantum mechanics. It has applications in the theory of mesomolecules and in the physics of polar molecules. The energy levels and other characteristics of the nonrelativistic electron–dipole system have been investigated by a number of authors analytically [1], as well as numerically [2, 4–6]. It is well known [1–3, 5] that a certain critical value of the dipole moment, $d_c = Zr$, exists, below which an electron lacks bound states in the field of a dipole, i.e., the electron cannot be held by the dipole field, when the separations between the poles of the dipole are less than $r_c = d_c/Z = 0.64$ au. Solving the corresponding relativistic problem (i.e., the problem on a relativistic electron motion in the field of a finite dipole) presents a complicated mathematical problem, because variables in the Dirac equation with the two-center potential cannot be separated (in distinction to the Schrödinger equation) in any orthogonal coordinates. In this paper, the energy term close to the continuum is calculated analytically by sewing together the logarithmic derivatives of the asymptotic solution. This method has earlier been successfully employed by V.S. Popov for solving the Dirac equation for the symmetrical problem of two Coulomb centers with equal values and signs of the center's charges.

In this paper, we generalize the results of [1], where the problem on nonrelativistic electron motion in the field of a finite electric dipole has been solved, to the relativistic case. In doing so, we employ the above-mentioned method of sewing together the asymptotics. This method has been employed in [7, 10] for solving the Coulomb two-center problem with the center's charges being equal both in the value and the sign.

We consider the motion of relativistic electron in the field of finite electric dipole consisting of the charges $+Z\alpha$ and $-Z\alpha$, which are spaced at the distance $R$. The potential of such a system has the form

$$V = \frac{Z\alpha}{r_1} - \frac{Z\alpha}{r_2}, \tag{1}$$

where $r_i$ is the spacing between the electron and the $i$th particle, $\alpha = 1/137$ (hereafter, we use the system of units $\hbar = m_e = c = 1$). The electron motion is described by the stationary Dirac equation:

$$H\psi = \varepsilon\psi. \tag{2}$$

Here, $H = \boldsymbol{\alpha}\mathbf{p} + \beta + V$ is the Dirac Hamiltonian, $\varepsilon$ is the electron energy, and $\alpha$ and $\beta$ are the Dirac matrixes.

For the subsequent studying the motion of this electron, we employ the squared Dirac equation, which can be expressed in the spinor representation in terms of the components $\psi_1$ and $\psi_2$ of the bispinor $\psi = \begin{pmatrix}\psi_1\\ \psi_2\end{pmatrix}$:

$$[(\varepsilon - V)^2 + \Delta + i\boldsymbol{\sigma}\nabla V - 1]\psi_1 = 0, \tag{3}$$

$$[(\varepsilon - V)^2 + \Delta - i\boldsymbol{\sigma}\nabla V - 1]\psi_2 = 0. \tag{4}$$

Here, $\boldsymbol{\sigma}$ is the Pauli matrixes.

Away from the dipole, the terms $V^2$ and $i\boldsymbol{\sigma}\nabla V$ can be neglected in comparison with the term $V$.

Then, for each of the components, we obtain the equation:

$$[\Delta - 2\varepsilon V + \varepsilon^2 - 1]\psi = 0. \tag{5}$$

This equation can be treated as the Schrödinger equation with the potential $\varepsilon V$ and the energy $(\varepsilon^2 - 1)/2$. Asymptotic properties of such an equation have been studied in detail in [1]; therefore, below, we employ the results of this paper.

Thus, away from the dipole, the wave function can be represented in the separated form [1]:

$$\psi = \frac{U(\xi)}{(\xi^2 - 1)^{1/2}} \frac{V(\eta)}{(1 - \eta^2)^{1/2}} \exp(im\varphi). \tag{6}$$

Here, $\xi$, $\eta$, and $\varphi$ are elongated spheroidal coordinates

*Department of Thermal Physics, Academy of Sciences of Uzbekistan, ul. Katartal 28, Tashkent, 700135 Uzbekistan*
*E-mail: davron@silk.org*

1028-3358/00/4501-0022$20.00 © 2000 MAIK "Nauka/Interperiodica"

determined in [1] as:

$$\xi = (r_1 + r_2)R^{-1}, \quad \eta = (r_1 - r_2)R^{-1},$$
$$\text{and } \varphi = \arctan(y/x).$$

Here, $y$ and $x$ are Cartesian coordinates, and $R$ is the spacing between the charges. On substitution into (5), the radial and angular distributions take the form [1]:

$$U''(\xi) + \left[-p^2 + \frac{A}{\xi^2 - 1} + \frac{1 - m^2}{(\xi^2 - 1)^2}\right]U(\xi) = 0, \quad (7)$$

$$V''(\eta) + \left[-p^2 + \frac{D\eta - A}{1 - \eta^2} + \frac{1 - m^2}{(1 - \eta^2)^2}\right]V(\eta) = 0. \quad (8)$$

Here, $p^2 = -\frac{R^2}{4}(\varepsilon^2 - 1)$, $D = 2|\varepsilon|RZ\alpha$, $A$ is the separation constant, and $m$ is the azimuth quantum number. $U''(\xi)$ and $V''(\eta)$ are the second derivatives of the radial and the angular functions, respectively. Boundedness of the wave function $\psi$ results in the boundary conditions for the functions $U$ and $V$ [1, 6]:

$$U(1) = 0, \quad U(\xi)_{\xi \to \infty} \longrightarrow 0, \quad V(\pm 1) = 0. \quad (9)$$

These equations have been analyzed in detail in [1]. Hence, using the results of [1], we can represent the asymptotics of the wave-function at large separations from the dipole in the form (at $m = 0$):

$$\psi \sim \left[\frac{\pi}{\nu \sinh \pi\nu}\right]^{1/2} (p\xi)^{1/2}(\xi^2 - 1)^{-1/2} \times \sin\left(\nu \ln\frac{2}{p\xi} + \arg\Gamma(1 + i\nu)\right). \quad (10)$$

Nearby the dipole (at $R \ll 1$), the asymptotics of the wave function can be written out as:

$$\psi_1 \sim (\xi^2 - \eta^2)^{\beta}, \quad (11)$$

where

$$\beta = \begin{cases} \gamma - 1 & (Z < 137) \\ 1 & (Z > 137). \end{cases}$$

At small $\eta$

$$\psi_1 \sim \xi^{2\beta}. \quad (12)$$

For $|\varepsilon| \approx 1$, the above asymptotics of the wave functions, both away from the dipole and nearby it, overlap each other on the interval $1 \ll \xi \ll 1/p$. Equating the logarithmic derivatives of functions (12) and (10) on this interval and taking into account that here the relation $\ln\frac{2}{p\xi} \approx \ln\frac{2}{p}$ holds, we obtain

$$\frac{1}{2} + \nu \cot\left[\nu \ln\frac{2}{p} + \arg\Gamma(1 + i\nu)\right] = -2\beta, \quad (13)$$

where

$$D = 2|\varepsilon|ZR\alpha,$$
$$\nu = \left[\frac{8\pi^2}{\Gamma^4(1/4)}(D - D_{cr}) - \frac{R^2}{6}(\varepsilon^2 - 1)\right]^{1/2}, \quad (14)$$
$$\text{and } D_{cr} = \frac{\Gamma^4(1/4)}{32\pi}\left[1 - \frac{2}{3\pi}\right]$$

is the critical value of the dipole moment. At $D = D_{cr}$, the term $\varepsilon(R)$ reaches the continuum boundary.

For $Z < 137$, solving this equation yields the energy term:

$$\varepsilon_{\pm} = \pm 1 \mp \frac{2}{R^2}\exp\left[-\frac{\Gamma^2(1/4)}{\pi(4Z\alpha R - 2D_{cr})^{1/2}} \times \operatorname{arccot}\frac{\Gamma^2(1/4)(3 - 4\gamma)}{4\pi(4Z\alpha R - 2D_{cr})^{1/2}}\right]. \quad (15)$$

As it is well known, the nonrelativistic limit is reached near the upper continuum, where $(4Z\alpha R - 2D_{cr}) \sim 0$ and $\operatorname{arccot} \longrightarrow \pi$. Hence, to evaluate the nonrelativistic limit for our formula, it is necessary to perform the following changings: $\gamma \longrightarrow 1$, $\operatorname{arccot} \longrightarrow \pi$. Then, we obtain in the nonrelativistic limit (after subtraction of the rest mass):

$$\varepsilon_{\pm} = \mp\frac{2}{R^2}\exp\left[-\frac{\Gamma^2(1/4)}{(4Z\alpha R - 2D_{cr})^{1/2}}\right]. \quad (16)$$

This formula coincides with the one obtained earlier in [1] for the energy term of nonrelativistic electron–dipole system. We would like to note that nonrelativistic limit for our formula can be reached only over a small region of center-to-center separations close to the critical distance. Really, expanding the arccotangent into series,

$$\operatorname{arccot}\frac{\Gamma^2(1/4)(3 - 4\gamma)}{4\pi(4Z\alpha R - 2D_{cr})^{1/2}} \approx \pi - \frac{4\pi(4Z\alpha R - 2D_{cr})^{1/2}}{\Gamma^2(1/4)(4\gamma - 3)}, \quad (17)$$

we obtain for $\varepsilon_{\pm}$:

$$\varepsilon_{\pm} = \pm 1 \mp \frac{2}{R^2}\exp\left[-\frac{\Gamma^2(1/4)}{(4Z\alpha R - 2D_{cr})^{1/2}} + \frac{4}{4\gamma - 3}\right]. \quad (18)$$

This results in the nonrelativistic limit taking place at

$$R_{cr} \ll R \ll R_{cr} + \frac{4(4\gamma - 3)}{3Z\alpha}.$$

For example, for $Z = 1$, this can be written as either $R_{cr} \ll R \ll R_{cr} + 182$, or $R_{cr} \ll R \ll 3R_{cr}$ (as in the system of units where $m = h = c = 1$, $R_{cr} = 88.3$).

At $Z > 137$, we obtain:

$$\varepsilon_{\pm} \approx \pm 1 \mp \frac{2}{R^2} \exp\left[ -\frac{\Gamma^2(1/4)}{\pi(4Z\alpha R - 2D_{cr})^{1/2}} \times \left( \operatorname{arccot} \frac{5\Gamma^2(1/4)}{4\pi(4Z\alpha R - 2D_{cr})^{1/2}} - \pi \right) \right]. \quad (19)$$

It should be noted that the formulas evaluated are relevant only for the ground state. Nevertheless, the same method could be applied for calculating the energy term for any excited state, using the expression for $D$ from [1] relevant for excited states.

Thus, we have evaluated analytic formulas for the energy levels nearby the continuum for a relativistic electron moving in the field of a finite electric dipole. The analytic formulas obtained could be useful for further numerical calculations in the nonasymptotic region.

## REFERENCES


1. D. I. Abramov and I. V. Komarov, Teor. Mat. Fiz. **13**, 209 (1972).
2. J. E. Turner and K. Fox, Phys. Rev. **174**, 81 (1968).
3. E. Fermi and E. Teller, Phys. Rev. **72**, 399 (1947).
4. O. H. Crawford, Proc. Phys. Soc. **91**, 279 (1967).
5. R. F. Wallis, R. H. Herman, and H. W. Milnes, J. Molec. Spectrosc. **4**, 51 (1960).
6. I. V. Komarov, L. N. Ponomarev, and S. Yu. Slavyanov, *Spheroidal and Coulomb Spheroidal Functions* (Nauka, Moscow, 1976).
7. V. S. Popov, Yad. Fiz. **17**, 621 (1973) [Sov. J. Nucl. Phys. **17**, 322 (1973)].
8. V. S. Popov, Yad. Fiz. **19**, 155 (1974) [Sov. J. Nucl. Phys. **19**, 81 (1974)].
9. M. S. Marinov and V. S. Popov, Zh. Éksp. Teor. Fiz. **68**, 421 (1975) [Sov. Phys. JETP **41**, 205 (1975)].
10. V. S. Popov, Pis'ma Zh. Éksp. Teor. Fiz. **16**, 355 (1972) [JETP Lett. **16**, 251 (1972)].
11. A. A. Grib, S. G. Mamaev, and V. M. Mostepanenko, *Vacuum Quantum Effects in Strong Fields* (Énergoatomizdat, Moscow, 1988).


*Translated by O. Chernavskaya*

*Doklady Physics, Vol. 45, No. 1, 2000, pp. 25–26. Translated from Doklady Akademii Nauk, Vol. 370, No. 3, 2000, pp. 339–340.*


**PHYSICS**

# Interference Pattern at Gravitational Focusing

**Corresponding Member of the RAS S. G. Rautian**

Received July 2, 1999

Microlensing (gravitational focusing) of stellar radiation is actively investigated during last few years [1, 2]. A principal and most important result consists in the fact that a short-term (of about several tens days) enhancement in the stellar brightness for a number of stars, which is caused by gravitational fields, is established by observations and as a result of theoretical analysis. The goal of this paper is to draw attention to interference features of the focused-radiation field.

The conventional procedure for calculating ray trajectories is shown schematically in the figure. The relation between transverse coordinates ($\rho$, $r$) of light rays in the plane ($D$) of a gravitational lens and the observation plane ($O$) has the form

$$\frac{\rho L}{L_1} - \theta(\rho)L_2 = r, \quad L = L_1 + L_2, \tag{1}$$

where $\theta(\rho)$ is the angle of the ray deviation by the gravitational lens, $L_1 = DS$, and $L_2 = OD$. In the case of a spherically symmetric point lens, we can assume that

$$\theta(\rho) = \frac{2r_g}{\rho}, \quad r_g = \frac{2GM}{c^2}. \tag{2}$$

Here, $M$ and $r_g$ are the mass and gravitational radius of the lens, respectively; $G$ is the gravitation constant. Equality (1) is a quadratic equation with respect to $\rho$, and its roots are

$$\rho_{1,2} = \frac{[r \pm \sqrt{r^2 + r_0^2}]L_1}{2L}, \quad r_0^2 = \frac{8r_g L L_2}{L_1}. \tag{3}$$

Using relations (3), we can calculate illumination $E(r)$ of the plane $O$, which is proportional to $L_1^{-2}\sum|\rho d\rho/rdr|$ [the sum over roots (3)]. It is easy to show that $E(r)$ is described by formulas

$$E(r) = L^{-2} + \Delta E(r), \tag{4}$$

$$\Delta E(r) = \frac{r_0^4}{2L^2 r\sqrt{r^2 + r_0^2}[\sqrt{r^2 + r_0^2} + r]^2}. \tag{5}$$

The parameter $r_0$ determines the effective width $\Delta E(r)$ as a function of $r$. For $r_g = 0$, we have $\Delta E(r) = 0$, i.e., the term $1/L^2$ in formula (4) corresponds to the illumination in the absence of gravitational focusing. The function $\Delta E(r) > 0$ determines the illumination enhancement produced by the gravitational lens (in the domain of small angles $r/L$). For $r = 0$, an integrable singularity inherent in geometric-optic calculation for a point-source model takes place. Integrating $\Delta E(r)$ with respect to $r$, we find the corresponding light flux:

$$\Delta\Phi = 2\pi\int_0^\infty \Delta E(r) r dr = 2\pi\left(\frac{r_0}{2L}\right)^2. \tag{6}$$

The coherent properties of the telescopic image for a star, whose radiation had passed through a gravitational lens, were considered in [3]. We now examine interference properties of the illumination distribution in the $O$-plane, which is a quantity proportional to the total light flux entering the telescope lens. We consider the interference of waves propagating from two imaginary light sources $S_1$ and $S_2$ (see figure). Due to the spherical symmetry of the lens, the elements of the fringe pattern observed in the $O$-plane have the form of concentric rings. The contrast of fringes is determined by the ratio between the intensities of interfering rays. Let $E_1$ and $E_2$ be contributions to $E(r)$ from $S_1$ and $S_2$, respectively. It is easy to show that $E_1 + E_2 = 1/L^2 + 2E_2$, i.e., both rays equally contribute to $\Delta E(r)$. Therefore, fringes have the unit contrast with respect to the variable part of the fringe pattern. Thus, the distribution of

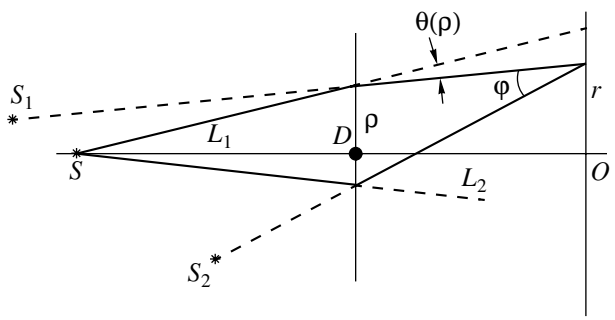


**Figure.**

*Institute of Automation and Electrometry,*
*Siberian Division, Russian Academy of Sciences,*
*Universitetskiĭ pr. 1, Novosibirsk, 630090 Russia*

1028-3358/00/4501-0025$20.00 

the illumination in the *O*-plane can be written out in the form

$$E(r) = L^{-2} + \Delta E(r)\left\{1 + \cos\left[\frac{2\pi\Delta(r)}{\lambda}\right]\right\}. \quad (7)$$

The difference in the ray path lengths for the rays outgoing from $S_1$ and $S_2$ is

$$\Delta(r) = \int_{l_2} n(R)dl - \int_{l_1} n(R)dl, \quad n(R) = 1 + \frac{r_g}{R}, \quad (8)$$

where integrals are taken along the rays from $S_2$ and $S_1$; $n(R)$ and $R$ is the effective refractive index [4] depending on the gravitation field and the distance from the point mass to the ray, respectively. Evaluating $\Delta(r)$, it is possible to approximate the rays by segments of straight lines and then to arrive at the equality

$$\Delta(r) \approx 4r_g[\eta\sqrt{1+\eta^2} + \ln(\sqrt{1+\eta^2} + \eta)], \quad \eta = \frac{r}{r_0}. \quad (9)$$

Here, the first term in square brackets and the logarithmic term are stipulated by the unity in expression (8) for $n(R)$ and the term $r_g/R$, respectively. It is seen from relation (5) that a noticeable enhancement in illumination caused by microlensing takes place provided that $\eta \ll 1$ (e.g., $\Delta E = 4L^{-2}$ at $\eta = 0.1$). In such conditions important from the standpoint of practice, it follows from formula (9) that

$$\Delta(r) \approx 8r_g\eta, \quad \eta = \frac{r}{r_0} \; 1. \quad (10)$$

We now write out basic characteristics of the interference pattern, The order $m$ of a fringe can be approximately represented in the form

$$m = \frac{\Delta}{\lambda} \approx \frac{8r_g\eta}{\lambda}. \quad (11)$$

The fringe period $\delta r$ is determined by the expression

$$\delta r = \lambda\left(\frac{d\Delta}{dr}\right)^{-1} \approx \frac{r}{m} = \frac{\lambda L_2}{2R_E} = \lambda\sqrt{\frac{LL_2}{8r_gL_1}},$$
$$R_E = \sqrt{\frac{2r_gL_1L_2}{L}}, \quad (12)$$

where $R_E$ is the Einstein radius. The words related to the contrast hold true for the point light source as well. The finiteness of angular dimensions $\theta_S$ of the star $S$ does not decrease the contrast if the period is $\delta r > \theta_S LL_2/L_1$, i.e.,

$$\theta_S < \theta_{S\,\mathrm{cr}} \equiv \frac{\delta r L_1}{LL_2} = \frac{\lambda}{r_0}. \quad (13)$$

We recall that the observation of fringes on the order of $m$ requires for the radiation monochromaticity to be $\lambda/\Delta\lambda \geq m$ ($\Delta\lambda$ is the spectral width).

Note also that the fringe order $m$ is determined by the ratio of two principal parameters of gravitational and electromagnetic fields. According to expression (12), approximately $m$ fringes lie in the enhanced-illumination domain of the width $r$. The feasibility to observe the interference is dependent on the values of $m$ and $\theta_{S\,\mathrm{cr}}$, which, in turn, are determined by the values of $\lambda$ and the mass $M$ of a gravitational lens:

$$m \backsim \frac{M}{\lambda}, \quad \theta_{S\,\mathrm{cr}} \backsim \frac{\lambda}{M^{1/2}}.$$

Numerical values for basic quantities are presented below for $\lambda = 10^{-4}$ cm, $\lambda = 10$ cm, $M = M_\odot$ (mass of the Sun), and $M = 10^{-6}M_\odot$:

| $M/M_\odot$ | 1 | | $10^{-6}$ | |
|---|---|---|---|---|
| $r_g$, cm | $3 \times 10^5$ | | 0.3 | |
| $r_0$, cm | $2.7 \times 10^{14}$ | | $2.7 \times 10^{11}$ | |
| $\lambda$, cm | $10^{-4}$ | 10 | $10^{-4}$ | 10 |
| $m$ | $2.4 \times 10^8$ | $2.4 \times 10^3$ | $2.4 \times 10^2$ | 0.024 |
| $\theta_{S\,\mathrm{cr}}$, rad | $0.4 \times 10^{-18}$ | $0.4 \times 10^{-13}$ | $0.4 \times 10^{-15}$ | $0.4 \times 10^{-10}$ |

The values of $M$ chosen correspond to the present concepts of a wide mass range for the dark matter, which is able to realize microlensing. In addition, it was taken that $L_1 = L_2$, $L = 10$ kpc $= 3 \times 10^{22}$ cm, $\eta = r/r_0 = 10^{-2}$. As is seen from the data represented above, in the short-wave region and for relatively massive lenses, the observation of the interference is hampered by the requirements for the radiation to be monochromatic and for the star dimensions to be finite (e.g., the angular dimension of a star with the Sun's radius and removed from us by a distance of 10 kpc must be $\theta_S = 5 \times 10^{-12}$ rad). Conditions for observations in a long-wave (decimeter) region are more favorable, especially as the highly monochromatic radiation of space masers are known in this region [5]. It is also evident that the observation of interference phenomena is more probable for small-mass lenses.

The described interference pattern corresponds to the case of a spherically symmetric compact lens. In other cases, the interference pattern also exists, but its shape and characteristics are, naturally, different.

## REFERENCES

1. V. A. Gurevich, K. P. Zybin, and V. A. Sirota, Usp. Fiz. Nauk **167**, 913 (1997) [Phys.–Usp. **40**, 869 (1997)].
2. A. A. Zakharov and V.M Sazhin, Usp. Fiz. Nauk **168**, 1041 (1998) [Phys.–Usp. **41**, 945 (1998)].
3. A. F. Zakharov, *Gravitational Lenses and Microlenses* (Yanus, Moscow, 1997).
4. V. A. Fok, *Theory of Space, Time, and Gravitation* (Gostekhizdat, Moscow, 1955).
5. V. S. Strel'nitskiĭ, Usp. Fiz. Nauk **113**, 463 (1974).

*Translated by V. Devitsyn*

*Doklady Physics, Vol. 45, No. 1, 2000, pp. 27–29. Translated from Doklady Akademii Nauk, Vol. 370, No. 2, 2000, pp. 178–180.*


**TECHNICAL PHYSICS**

# Features of Discontinuous Decomposition of Austenitic Nitrogenized Steel after Shock-Wave Loading

**V. I. Zel'dovich*, A. I. Uvarov*, N. A. Tereshchenko*, N. Yu. Frolova*, Academician B. V. Litvinov**, and N. P. Purygin****

Received August 31, 1999

We have investigated the discontinuous decomposition of 09Kh20AG19 steel containing 0.09, 19.5, 18.6, and 0.6 wt % of C, Cr, Mn, and N, respectively. Beforehand, the steel was subjected to three-stage processing such as (i) quenching from 1323 K in water (isothermal soaking for 2 h); (ii) quenching from 1323 K with subsequent shock-wave loading; and (iii) heating up to 1323 K with subsequent soaking (without cooling down to the room temperature 293 K) in a furnace with a temperature of 1073 K. The decomposition occurred at 1073 K with different soaking time (up to 30 h). The decomposition temperature is chosen at which the discontinuous decomposition of the investigated hardened steel is the most intense. At this temperature (1073 K), the discontinuous decomposition was observed in steels with close composition as well [1, 2]. A sample was loaded by shock waves at a pressure $P$ equal to 40 or 100 GPa, which was exerted to sample end faces or arose at a place of superposition of primary shock waves, respectively, [3].

In papers [4–6], the effect of shock-wave loading on decomposition of a supersaturated solid solution was investigated for the continuous aging mechanism. The goal of this study is to investigate discontinuous aging of the austenitic nitrogenized steel that had been subjected to the shock-wave loading.

After aging of the hardened steel for 1 h at 1073 K, its discontinuous decomposition was noticed only at certain segments of grain boundaries. The degree of the decomposition (the ratio between the area of a section that has undergone discontinuous decomposition and the total area) is 0.04–0.05. The degree of the decomposition $R$ grows monotonically with increasing the aging time $\tau$ and attains the value $R \approx 0.5$ at $\tau = 15$ h. The further increase of the soaking time almost does not vary the degree of the decomposition (see Fig. 1, curve *2*). In the austenitic steel, the maximum degree of the discontinuous decomposition is determined by the nitrogen content in the solid solution.

The shock-wave loading intensifies essentially the discontinuous decomposition. For example, after soaking the sample subjected to such a loading at constant temperature ($T$ = 1073 K) for 1 h, the degree of the decomposition is the same as after quenching the sample and soaking it at constant temperature for 15 h. For the sample that has been subjected to the shock-wave loading, an excess of the soaking time over 1 h affects negligibly the degree of the decomposition (Fig. 1, curve *1*). It should be noted that the shock-wave loading, in itself, did not lead to the discontinuous decomposition.

We have also found that at 923 K, the discontinuous decomposition of the hardened steel does not develop. However, after the shock-wave loading, the discontinuous decomposition occurs intensely at this temperature.

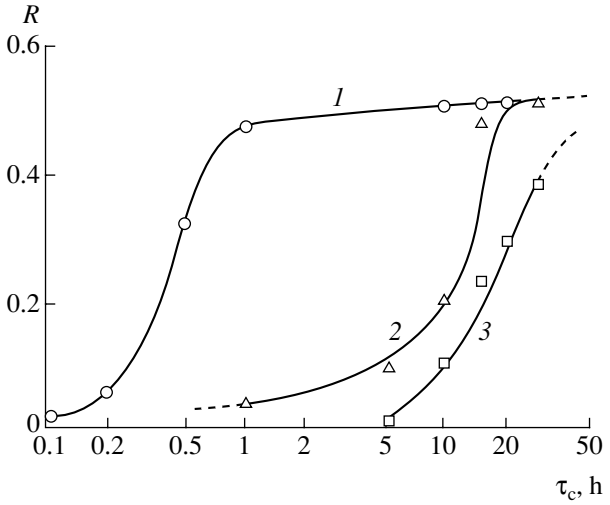


**Fig. 1.** Degree of the discontinuous decomposition as a function of soaking time at a constant temperature (1073 K) in the case of different preliminary processing: (*1*) shock-wave loading, (*2*) quenching in water, (*3*) heating up to 1323 K with subsequent soaking in another furnace at 1073 K.

* *Institute of Metal Physics, Ural Division, Russian Academy of Sciences, ul. S. Kovalevskoĭ 18, Yekaterinburg, 620219 Russia*

** *Russian Research Institute of Technical Physics, Snezhinsk, Chelyabinsk oblast, 454000 Russia*

1028-3358/00/4501-0027$20.00 © 2000 MAIK "Nauka/Interperiodica"

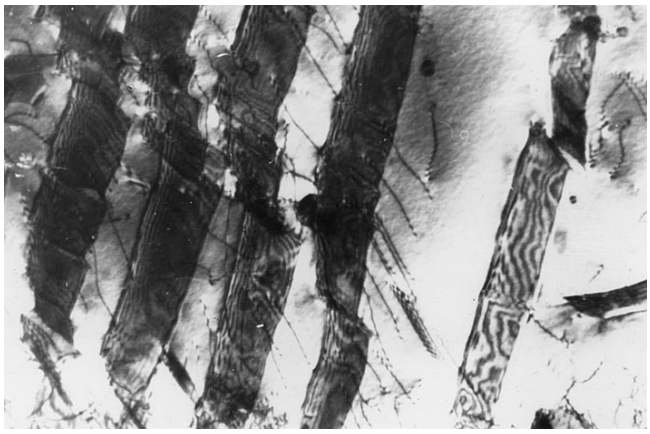

**Fig. 2.** Discontinuous decomposition after shock-wave loading, 1073 K, 1 h. A picture obtained with the use of an electron microscope, ×40000.

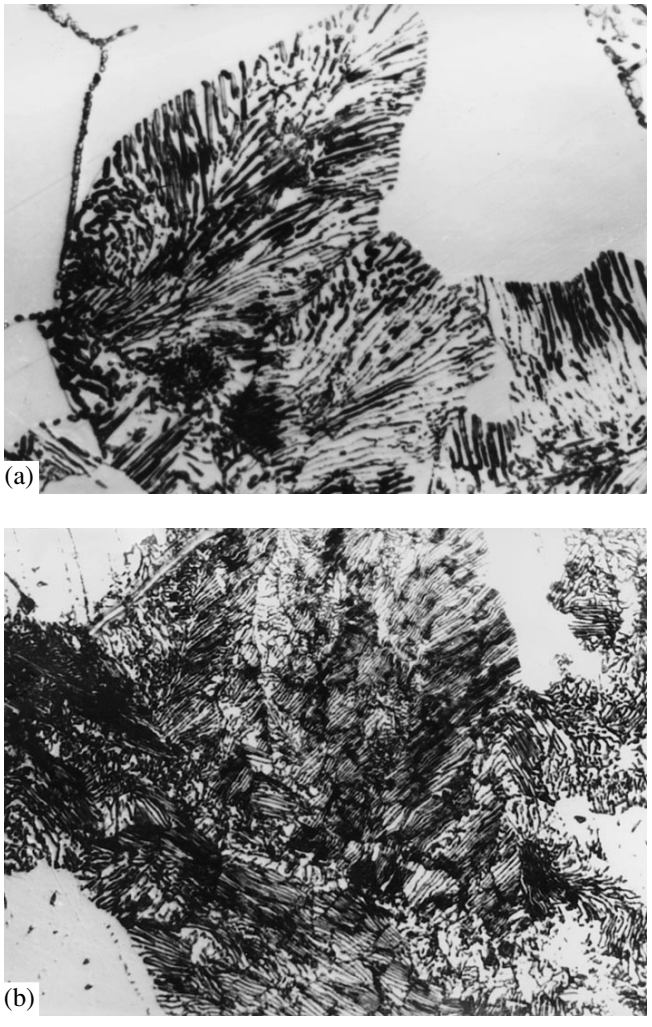

(a)

(b)

**Fig. 3.** (a) Microstructure of cells in the case of the discontinuous decomposition in hardened steel (1073 K, 30 h) and (b) decomposition after shock-wave loading (1073 K, 1 h), ×880.

In 5 h, the degree of the decomposition attained is the same as in 1 h at 1073 K.

It is known that the discontinuous decomposition of austenitic nitrogenized steels occurs with precipitation of chrome nitride ($Cr_2N$) particles [1, 2]. We have demonstrated that these particles have the shape of thin plates either flat or curved. The plates consist of separate short parts and can be, sometimes, displaced with respect to each other. The orientation of $Cr_2N$ particles situated in cells of the discontinuous decomposition is related to austenite: the basal plane of the hexagonal chrome-nitride lattice ($a$ = 0.275 nm, $c$ = 0.445 nm) is approximately parallel to the {111}-type austenite plane.

For close-packed directions in the $Cr_2N$ (0001) planes and austenite {111} planes, a mismatch parameter was determined in the standard way as

$$\left(a - \frac{a_\gamma\sqrt{2}}{2}\right)\left(\frac{a_\gamma\sqrt{2}}{2}\right)^{-1},$$

where $a_\gamma$ = 0.362 nm is the austenite-lattice spacing. The mismatch parameter turns out to be high and equal to 7.4%. Owing to its high value, considerable elastic distortions arise in cells of the discontinuous decomposition. These distortions play an important role for both originating and growing the cells. They cause bending and fracturing the $Cr_2N$ plates, their cleavage, formation of new boundaries in the cell's austenite, and nucleation of dislocations. The shock-wave loading causes additional generation of dislocations, stacking faults, and deformation twins [3]. This results in strong deforming the $Cr_2N$ plates in certain cells of the discontinuous decomposition (Fig. 2). Extinction contours occurring inside the plates testify to the extremely small plane thickness and a high degree of their local bending. The growth of the discontinuous-decomposition cells becomes slower or completely ceases at boundaries of annealing twins and on slip planes decorated by the precipitation phase. Therefore, boundaries of cellular-decomposition aggregates formed as a result of shock-wave loading, sometimes have acute-angle shape and consist of short rectilinear segments.

After the shock-wave loading, cell dimensions and interplate distances turn out to be much smaller than they are after quenching the sample (Fig. 3). Microstructure photographs were used to determine kinetic parameters of the discontinuous decomposition in steels subjected to both quenching and shock-wave loading. The data obtained are brought together in the table. After the shock-wave loading, the number of growth centers (the number of cells) per grain (average grain dimension is 200 μm) increases three times. The actual increase is possibly still further, because we cannot always resolve in photographs cell boundaries after their merging in steels subjected to the shock-wave loading. Due to the shock-wave loading, new growth centers arise both at boundaries of initial grains and

inside them. The maximum cell size in the direction of their growth decreases approximately three times, seemingly, because their collisions in the growth process. The average growth rate $G$ calculated according to the total duration of the decomposition, increases by the order of magnitude after the shock-wave loading, while the distance $S$ between the plates decreases approximately twice.

The discontinuous decomposition process in steels under investigation is governed by the chrome diffusion in boundary grains [7, 8]. We now estimate the coefficient of boundary chrome diffusion by the relation $D_b = GS^2/\lambda$, where $\lambda$ is the boundary thickness [8]. Usually, $\lambda = 0.5$ nm is accepted [9]. Values of both the average growth rate $G$ and distance $S$ between the plates are presented in the table. Our calculations show that, after the shock-wave loading, the coefficient of boundary chrome diffusion increases nearly three times.

It is well known that, at grain boundaries, the diffusion mechanism for substitutional atoms is of vacancy nature [9]. Since the diffusion coefficient is proportional to the vacancy concentration $C_v$, we can conclude that, after the shock-wave loading, the value of $C_v$ increases three times. In actual situations, an increase in $C_v$ can be even more, because vacancies tend rapidly to move towards grain boundaries, to dislocations and their aggregates.

Special experiments were carried out in order to additionally confirm the explanation proposed for promoting the discontinuous-precipitation kinetics by shock-wave loading. Steel samples were heated up to 1323 K. Then, instead of being quenched in water, they were placed in another furnace, then were soaked there for some time at a constant temperature of 1073 K, and, hereupon, were subjected to cooling in the air ambient. According to [7], such a processing method decreases the number of vacancies in the matrix. As a result, kinetics of the discontinuous decomposition is decelerated, which is proven by comparison of curves *2* and *3* plotted in Fig. 1.

Thus, we can summarize the results obtained. In the austenitic nitrogenized steels subjected to shock-wave loading under pressure exceeding or equal to 40 GPa, the discontinuous decomposition becomes by the factor of ten (or larger) more rapid than that occurring in hardened steel. The growth rate of the decomposition cells increases by the order of magnitude, the number of decomposition centers increases approximately three times, while the distance between the plates decreases twice. The observed promotion of the discontinuous decomposition reaction is explained by an increase in vacancy concentration and, therefore, by the triple increase in the coefficient of the chrome boundary diffusion.

**Table**

| Initial state | Number of centers per grain | Maximum cell dimension, μm | $G$, μm/h | $S$, μm | $D_b$, $10^8$ cm$^2$/s |
|---|---|---|---|---|---|
| Quenching | 3.5 | 102 | 3.4 | 1.1 | 2.3 |
| Shock-wave loading | 11 | 33 | 33 | 0.6 | 6.6 |

## REFERENCES


1. Yu. N. Goĭkhenberg, L. G. Zhuravlev, V. Yu. Vnukov, *et al.*, Fiz. Met. Metalloved., No. 1, 99 (1990).
2. N. C. Santhisrinivas, *et al.*, Scr. Materialia **37**, 285 (1997).
3. A. I. Uvarov, B. V. Litvinov, V. I. Zel'dovich, *et al.*, Khim. Fiz. **14** (2/3), 106 (1995).
4. I. N. Gavril'ev, A. A. Deribas, V. I. Zel'dovich, *et al.*, Fiz. Met. Metalloved. **65**, 801 (1988).
5. A. I. Uvarov, V. I. Zel'dovich, O. S. Rinkevich, *et al.*, Fiz. Met. Metalloved. **83**, 138 (1997).
6. O. A. Bannykh, V. M. Blinov, I. N. Gavril'ev, *et al.*, Fiz. Goreniya Vzryva, No. 3, 104 (1982).
7. L. N. Larikov and O. A. Shmatko, *Cellular Decomposition of Supersaturated Solid Solutions* (Naukova Dumka, Kiev, 1976).
8. Sukhovarov, V.F., *Discontinuous Phase Precipitation in Alloys* (Nauka, Novosibirsk, 1983).
9. B. S. Bokshteĭn, *Diffusion in Metals* (Metallurgiya, Moscow, 1978).


*Translated by Yu. Verevochkin*

*Doklady Physics, Vol. 45, No. 1, 2000, pp. 30–32. Translated from Doklady Akademii Nauk, Vol. 370, No. 1, 2000, pp. 43–45.*


**MECHANICS**

# On Plane Flows of an Ideally Rigid-Plastic Medium

**D. D. Ivlev and L. A. Maksimova**

Presented by Academician A.Yu. Ishlinskiĭ April 7, 1999

Received April 22, 1999

Unsteady plane yielding of an ideally rigid-plastic medium is considered below.

**1.** For a plane problem of the ideal-plasticity theory, the condition of plasticity can be written as

$$(\sigma_x - \sigma_y)^2 + 4\tau_{xy}^2 = 4\kappa^3, \quad \kappa = \text{const}, \qquad (1.1)$$

where $\sigma_x$, $\sigma_y$, and $\tau_{xy}$ are the stress components in the Cartesian coordinate system, and $\kappa$ is the shear yield stress.

We assume that a plastic half-space of an ideal rigid-plastic material contains the *FOF*' wedge as a rigid inclusion. A wedge position is asymmetric with respect to the *CC*' free boundary and determined by both the distance from it $PO = h$ and the angles $\alpha$ and $\beta$ (see Fig. 1).

A zone of plastic straining is bounded by the *BOB*' triangle, and a stressed state occurring there is uniform: $\sigma_x = 2\kappa$ and $\sigma_y = \tau_{xy} = 0$. The lines *BO* and *B*'*O* along which tangential stress is maximum ($\tau_{max} = \kappa$) are the slip lines. Therefore, tangential velocity components discontinue there [1, 2]. We assume that, in the *CBOF* region, the rigid material moves with the velocity *V* along *OF*, while, in the *C*'*B*'*OF*' region, its motion occurs with the velocity *V*' along *OF*'. According to our further assumptions, when the material yields, vertical velocity components of the rigid material are equal to each other, that is, $V\cos\alpha = V'\cos\beta$, and displacements of the *BC* and *B*'*C*' half-lines along the *y*-axis are parallel. We denote projections of the velocities *V* and *V*' onto the normal lines to the *BO* and *B*'*O* characteristic lines as $V_n$ and $V_n'$, respectively, (Fig. 1):

$$V_n = V\cos\left(\frac{\pi}{4} - \alpha\right), \quad V_n' = V'\cos\left(\frac{\pi}{4} - \beta\right). \qquad (1.2)$$

The velocity *U* characterizing motion in the zone of plastic straining is defined as a sum vector of the velocities $V_n$ and $V_n'$ (Fig. 1).

At the final moment of yielding, the *A* point reaches the $A_1$ position, which coincides with the *O* point (Fig. 1). Simultaneously, the points *B* and *B*' reach the positions $B_1$ and $B_1'$, respectively, so that zones occupied by the deformed material coincide with $B_1OO_1$, $B_1'OO_1'$.

The angle of inclination $\mu$ that the velocity *U* has with respect to the *y*-axis is determined by the relation

$$\tan\mu = \frac{\tan\alpha - \tan\beta}{2 + \tan\alpha + \tan\beta}. \qquad (1.3)$$

Dimensions of a cup formed in the final yield state are calculated with the use of the relations

$$B_1B_1' = B_1H + B_1'H,$$
$$B_1H = h\left[1 + \frac{2\tan\alpha}{2 + \tan\alpha + \tan\beta}\right], \qquad (1.4)$$
$$B_1'H = h\left[1 + \frac{2\tan\beta}{2 + \tan\alpha + \tan\beta}\right].$$

The cup depth is determined by the relation

$$OH = h\left[\frac{\tan\alpha + \tan\beta}{2 + \tan\alpha + \tan\beta}\right], \qquad (1.5)$$

which, at $\alpha = \beta$, takes the form

$$OH = h\frac{\tan\alpha}{1 + \tan\alpha}. \qquad (1.6)$$

At $\alpha = \pi/2$, the strip stretches [1] and $OH = h$.

If the vertical velocity $V\cos\alpha = V'\cos\beta$ is imposed, the straight lines *BC* and *B*'*C*' (see Fig. 1) are fixed and the deformation occurs via penetration of the *FOF*' indenter.

**2.** We consider stretching the strip along the *x*-axis under the condition that symmetric local isolated straining regions form. In the first quadrant, such a region of plastic straining is bounded by the *OACM* zone (see Fig. 2). A similar situation occurs in the other quadrants. An intermediate position of the deformed free boundary is presented by the open polygons $EC_{12}A_{12}A_{11}A_{12}'C_{12}'E'$ and $FD_{12}B_{12}B_{11}B_{12}'D_{12}'F'$ (Fig. 2).

In the first quadrant, the material is deformed in the $OA_{11}A_{12}C_{12}ENO$ region. A similar situation occurs in

*Chuvash State Pedagogical University,*
*ul. Karla Marksa 38, Cheboksary, 428000 Russia*

1028-3358/00/4501-0030$20.00 

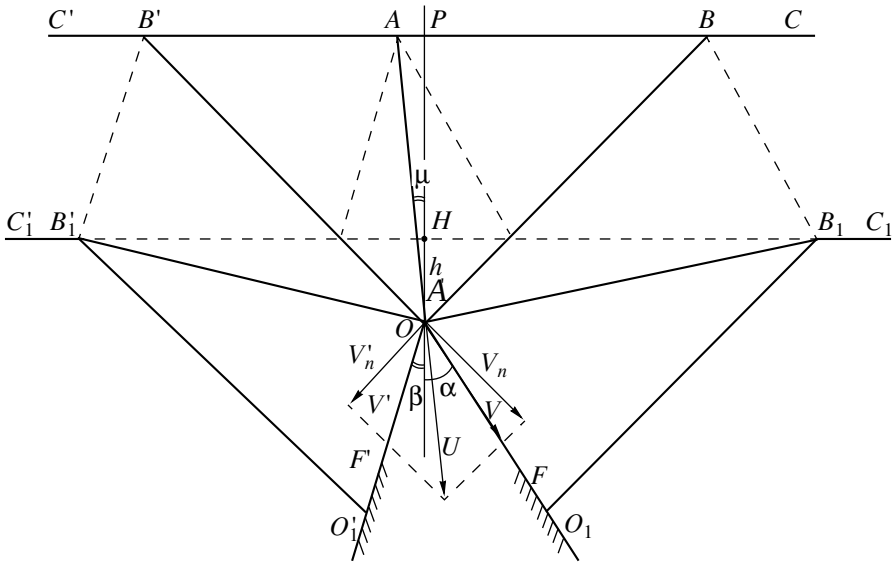


**Fig. 1.**

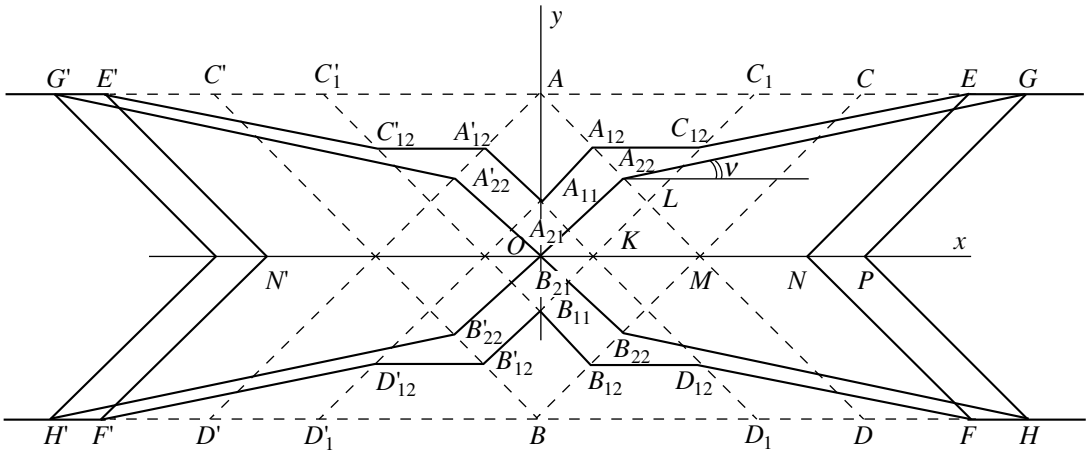


**Fig. 2.**

the other quadrants. We assume that the rigid-material velocity, which is directed along the $x$-axis, is equal to unity. Initially, the slip occurs along the characteristic lines $AD$, $AD'$, $BC$, and $BC'$. In an intermediate state, the $KC_{12}EN$ region is rigid. Simultaneously, velocity of the material in the $KA_{11}A_{12}L$ region is equal to $\sqrt{2}/2$ and directed along $A_{11}K$. The $A_{11}$ point shifts along the $y$-axis with velocity equal to unity. Tangential velocity components have a discontinuity along the $KC_{12}$ slip line. The line of velocity discontinuity moves; $KC_{12}$ shifts along the $x$-axis with velocity equal to unity. During straining, the initially undistorted zone of the plastic material $ACMO$ turns into a zone bounded by the $A_{11}A_{12}C_{12}ENO$ open polygon. At the final moment of straining, the points $O$, $A_{21}$, and $B_{21}$ coincide with each other.

The zone of plastic straining that forms finally in the first quadrant is bounded by the $OA_{22}GP$ open polygon. The relation $\tan\nu = 1/5$ holds, where $\nu$ is the angle of inclination of the $A_{22}G$ boundary of the deformed material with respect to the $x$-axis.

For a crack propagating in a rigid ideally plastic material, formation of a one-sided local isolated straining region has been considered in [3].

**3.** We consider yielding a strip of the width $h$ when it rotates round the $O$ point (see Fig. 3). The zone of plastic straining coincides with the $BOB'$ triangle in which $\sigma_x = 2\kappa$ and $\sigma_y = \tau_{xy} = 0$. The bending moment has the form $M = \kappa h^2/2$.

We denote the angular velocity as $\omega$ and define linear velocities in the $BOB'$ zone as

$$u = \omega x, \quad \nu = -\omega y. \tag{3.1}$$

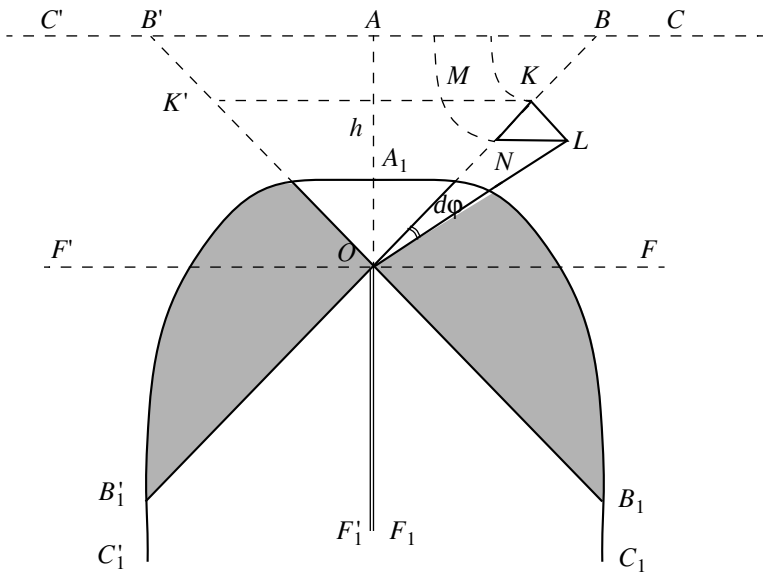


**Fig. 3.**

Stream lines of the flow described by (3.1) represent the hyperbolas $xy$ = const. The characteristic lines $BO$ and $B'O$ are free from velocity discontinuities. We assume that an intermediate position of the free boundary is presented by the $KK'$ line and use the notation $KO = r$. Rotation of the rigid zone by the angle $d\varphi$ turns the $MK$ elementary segment into the $NL$ segment (see Fig. 3). Since $dr = KN = KL$, we obtain that

$$dr = -rd\varphi, \quad r = C\exp(-\varphi). \tag{3.2}$$

At $\varphi = 0$, $r = BO = \sqrt{2}h$. Then, relation (3.2) yields

$$r = \sqrt{2}h\exp(-\varphi). \tag{3.3}$$

Figure 3 shows a position of the strip at the moment when each of its halves has turned by the angle $\pi/2$. Then, $A_1O = h\exp\left(-\frac{\pi}{2}\right)$. A zone of plastic straining of the material is shaded.

## REFERENCES

1. E. Onat and V. Prager, in *Mechanics* (Inostrannaya Literatura, Moscow, 1954), No. 4.
2. D. D. Ivlev and L. A. Maksimova, Dokl. Akad. Nauk **363**, 483 (1998) [Dokl. Phys. **43**, 779 (1998)].
3. A. I. Khromov, *Strain and Destruction of Rigid-Plastic Bodies* (Nauka, Vladivostok, 1996).

*Translated by Yu. Verevochkin*

*Doklady Physics, Vol. 45, No. 1, 2000, pp. 33–36. Translated from Doklady Akademii Nauk, Vol. 370, No. 1, 2000, pp. 46–49.*


**MECHANICS**

# Solving the Nozzle Direct Problem by Iterations along Streamlines

**Corresponding Member of the RAS N. N. Kalitkin, B. V. Rogov, and I. A. Sokolova**

Received July 21, 1999

**1. Methods for solving the problem.** Numerically solving the Laval-nozzle direct problem for viscous gas in the framework of the steady-state Navier–Stokes equations is hampered by a necessity to determine, in the course of solving, the critical gas-flow rate. Another difficulty consists in the fact that, in the case of high Reynolds numbers, these equations are of a mixed elliptic-hyperbolic type [1, 2]. Therefore, the basic numerical method for solving the direct problem in the framework of the Navier–Stokes equations is the relaxation method [3–5]. Besides an increase in the dimension of the problem under consideration, the disadvantage of this method is the slow (requiring several hundreds time steps) flow relaxation caused by a weak attenuation of wave processes in the subsonic part of nozzles.

Methods based on different simplified forms of the Navier–Stokes equations [2, 6], which are valid at certain restrictions imposed on the nozzle contour and the character of the flow, are sufficiently more efficient These simplified equations are of the evolution type with respect to the longitudinal coordinate (along the main flow direction) and, therefore, can be integrated by the use of rapid marching algorithms. For example, the marching calculation method based on the slender-duct approximation allows us to calculate the entire flow field in a nozzle with small inclinations $\tan\theta$ of the contour to the main flow direction and a small dimensionless duct curvature $K_w$ [2, 7].

The smooth-duct approximation [8–12] based on using an orthogonal coordinate system adapted to the duct geometry provides a better accuracy. This approximation accounts for the transverse pressure gradient associated with the centrifugal force. The accuracy of the method is determined by deviations of directions and curvatures of streamlines and longitudinal lines of the coordinate network used. The smooth-duct approximation makes it possible to calculate with an acceptable accuracy viscous flow in nozzles with moderate values of $\tan\theta \le 1$ and $K_w \le 0.5$ [9, 11].

Below, we propose an improved modification of the smooth-duct model. It well describes the entire field of viscous flow in nozzles with a considerable duct curvature ($K_w \le 2$) and thus, covers all requirements of practice. In contrast to both the parabolic slender-duct model and smooth-duct model, the set of equations describing the new model is elliptic in the subsonic zones and hyperbolic in supersonic ones.

For numerically solving the direct problem in the framework of these equations, an efficient marching method was developed. This method is based on the global iteration along streamlines and the longitudinal component of the pressure gradient. The method makes it possible to calculate, by a unified manner, viscous flow in the subsonic and supersonic zones. It is by orders of magnitude more efficient with respect to time consumed and computer memory required compared to the relaxation methods. Two global iterations are sufficient to determine within the accuracy of 0.01% such integral characteristics as the critical flow rate and the nozzle thrust.

**2. The flow model.** We consider the steady laminar flow of viscous gas in a plane or axial-symmetric Laval nozzle. The system of the simplified Navier–Stokes equations in terms of the adapted $(\xi, \eta)$ coordinate system [8, 9, 11] and natural variables has the following form.

The $\xi$-projection of the momentum equation is

$$\begin{aligned} & y^\nu H_\eta\left(\frac{\gamma p u}{T}\frac{\partial u}{\partial \xi} + \frac{\partial p}{\partial \xi}\right) \\ & = \frac{1}{\mathrm{Re}_r}\left\{\frac{\partial}{\partial \eta}\left[\mu y^\nu H_\xi\left(\frac{1}{H_\eta}\frac{\partial u}{\partial \eta} + K_\eta u\right)\right]\right. \\ & \left. - \mu y^\nu H_\xi H_\eta K_\eta\left(\frac{1}{H_\eta}\frac{\partial u}{\partial \eta} + K_\eta u\right)\right\} \\ & - y^\nu H_\xi H_\eta \frac{\gamma p u}{T}\tan\theta\left(\frac{1}{H_\eta}\frac{\partial u}{\partial \eta} - K_\eta u\right). \end{aligned} \tag{1}$$

*Institute of Mathematical Modeling, Russian Academy of Sciences, Miusskaya pl. 4a, Moscow, 125047 Russia*

1028-3358/00/4501-0033$20.00 

The energy equation is

$$y^{\nu}H_{\eta}\frac{\gamma pu}{T}\left[(\gamma-1)u\frac{\partial u}{\partial\xi}+\frac{\partial T}{\partial\xi}\right]$$

$$=\frac{1}{\mathrm{Re}_r}\frac{\partial}{\partial\eta}\left\{y^{\nu}H_{\xi}\left[(\gamma-1)\mu u\left(\frac{1}{H_{\eta}}\frac{\partial u}{\partial\eta}+K_{\eta}u\right)\right.\right. \quad (2)$$

$$\left.\left.+\frac{\lambda}{\mathrm{Pr}H_{\eta}}\frac{\partial T}{\partial\eta}\right]\right\}-y^{\nu}H_{\xi}\frac{\gamma pu}{T}\tan\theta\left[(\gamma-1)u\frac{\partial u}{\partial\eta}+\frac{\partial T}{\partial\eta}\right].$$

The η-component of the momentum equation is

$$\frac{\gamma pu}{TH_{\xi}}\left(\tan\theta\frac{\partial u}{\partial\xi}+u\frac{\partial\tan\theta}{\partial\xi}\right)$$

$$=-\frac{1}{H_{\eta}}\frac{\partial p}{\partial\eta}+(K_{\xi}\tan\theta-K_{\eta})\frac{\gamma pu^2}{T}. \quad (3)$$

Finally, the continuity equation is

$$\frac{y^{\nu}H_{\eta}}{T}\left[p\frac{\partial u}{\partial\xi}-\frac{pu}{T}\frac{\partial T}{\partial\xi}+u\frac{\partial p}{\partial\xi}\right]=-\frac{\partial}{\partial\eta}\left(y^{\nu}H_{\xi}\frac{pu}{T}\tan\theta\right)$$

$$+H_{\xi}H_{\eta}\left(y^{\nu}K_{\xi}-\frac{\nu\eta y'_w(x)}{\sqrt{1+\eta^2y'^2_w(x)}}\right)\frac{pu}{T}. \quad (4)$$

Here, $H_{\xi}$, $H_{\eta}$ are the Lamé parameters of the orthogonal (ξ, η)-coordinate system, ξ- and η-coordinates being longitudinal and transversal ones, respectively; $K_{\xi}$, $K_{\eta}$ are curvatures of coordinate lines ξ = const and η = const, respectively; $x$, $y$ are the Cartesian (the plane flow, ν = 0) or cylindrical (axial-symmetric flow, ν = 1) coordinates; $y = y_w(x)$ is the contour of the nozzle wall; $u$ and θ are the velocity-vector projection onto the line η = const and the angle between the vector and this line, respectively; $p$ and $T$ are static pressure and temperature of the gas; μ and λ are the dynamic viscosity coefficient and thermal conductivity, respectively. Equation (1)–(4) are written out with allowance for the equation of state of perfect gas $\rho = \gamma p/T$, where ρ is the density. We use dimensionless variables, the following values being taken as scales: $\rho_0$ and $T_0$ are values of corresponding variables on the axis in the inlet nozzle cross section; $u_0$ is the sound velocity $\sqrt{\gamma RT_0}$, where $R$ is the gas constant; $p_0 = \rho_0 u_0^2$, $r_0$ is the radius of the critical nozzle cross section. The following dimensionless expressions are also used: $\mathrm{Re}_r = \rho_0 u_0 r_0/\mu_0$ (the Reynolds number), $\gamma = c_{p0}/c_{\nu 0}$ (the adiabatic exponent), $\mathrm{Pr} = \mu_0 c_{p0}/\lambda_0$ (the Prandtl number).

The system of equations (1)–(4) differs from that of the smooth-duct model by additional terms appearing in the equation (3) for the transverse momentum [8–12]. From the mechanical standpoint, this difference reflects the following fact: In the smooth-duct model, the centrifugal force is calculated under the assumption that gas moves along the longitudinal network coordinate lines, whereas in the new model—with allowance for the gas motion along actual flow lines. From the mathematical standpoint, additional terms in equation (3) change the form of the set of equations in subsonic-flow domains from parabolic to elliptic one.

Equations (1)–(4) are first-order evolution ones with respect to the longitudinal ξ-coordinate; equations (1), (2), and (3), (4) are of the second order and of the first order, respectively, in terms of the transverse η-coordinate. The mathematical type of these equations determines their properties, the method of their solving, and the formulation of boundary conditions as well.

The calculation domain was bounded from below, from above, from the left, and from the right by the symmetry axis η = 0, the hard curvilinear wall η = 1, the inlet cross section, and the outlet cross section, respectively.

For evolution equations (1)–(4), transverse profiles $u/u_a$ ($u_a$ is the velocity on the axis), $\tan\theta$, $T$, and, also, the pressure $p_a$ on the axis are specified in the inlet cross section related to the subsonic zone. The velocity value on the axis, pressure distribution in this cross section, and the gas flow rate are determined in the process of solving the problem. In the outlet cross section, the soft boundary condition $\frac{\partial^2\tan\theta}{\partial\xi^2}=0$ is posed, which corresponds to the expected regime of the supersonic outflow from the nozzle [4].

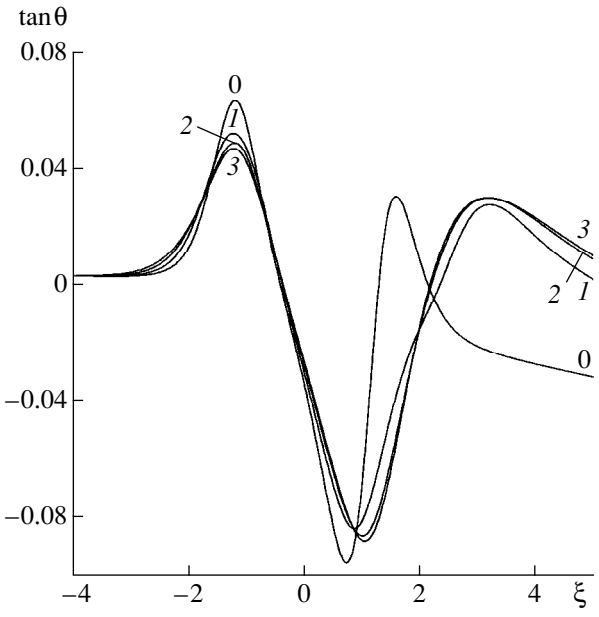


**Fig. 1.** Maximum deviation of streamlines from longitudinal coordinate ones. Ciphers indicate the number of a global iteration. Zero iteration step corresponds to the smooth-duct approximation [8–12].

The following boundary conditions are defined for equations (1), (2): the no-slip condition for the longitudinal velocity $u$; the heat-insulation condition $\frac{\partial T}{\partial \eta} = 0$ on the wall; and the symmetry conditions $\frac{\partial u}{\partial \eta} = \frac{\partial T}{\partial \eta} = 0$. For equations (3), (4), it is assumed that $\tan\theta = 0$ on the both wall and axis. This implies that the wall and the axis are the streamlines.

**3. Numerical method.** The system of equations (1)–(4) is elliptic in subsonic zones. Therefore, it is impossible to construct a purely evolutional method with respect to the longitudinal coordinate. Global iterations are required [6, 13] with fixing at each step evolutional derivatives responsible for the upstream-perturbation propagation in the subsonic-flow zones. There, such derivatives are the longitudinal pressure gradient in equation (1) and the longitudinal gradient of $\tan\theta$ in equation (3). The solution is found by iterations, each of them including two steps.

At the first step, we take streamline directions given by the $\tan\theta$ field. Then, we calculate for them the values of the critical flow rate, the velocity field, temperature, and pressure. To do this, the parabolic system of kinematic and energy equations (1)–(3) is solved by the marching method [12]. The mass-balance equation in the nozzle

$$\gamma \int_0^1 \frac{pu}{T} y^\nu H_\eta d\eta = \text{const}, \qquad (5)$$

that follows from continuity equation (4) with the boundary conditions taken into account for $\tan\theta$ on both the wall and axis, serves as the boundary condition for pressure on the axis.

The streamline directions are refined at the second step. For this purpose, the system of equations (1)–(4) regularized according to Vigneron [6] is integrated by the marching method [12]. The regularization consists in the replacement of the longitudinal pressure gradient in equation (1) by

$$\omega \frac{\partial p}{\partial \xi} + (1-\omega)\left(\frac{\partial p}{\partial \xi}\right)^0, \quad \omega = \frac{\sigma\gamma M_\xi^2}{1 + (\gamma-1)M_\xi^2}, \qquad (6)$$
$$0 \le \sigma < 1,$$

where $M_\xi$ is the local Mach number determined by the longitudinal velocity component, $\left(\frac{\partial p}{\partial \xi}\right)^0$ is the longitudinal pressure gradient calculated at the first step. As a result, the system of equations (1)–(4) becomes hyperbolic in subsonic zones and can be integrated by the marching method. In the course of computations, the safety factor $\sigma$ was taken to be $\sigma = 0.95$.

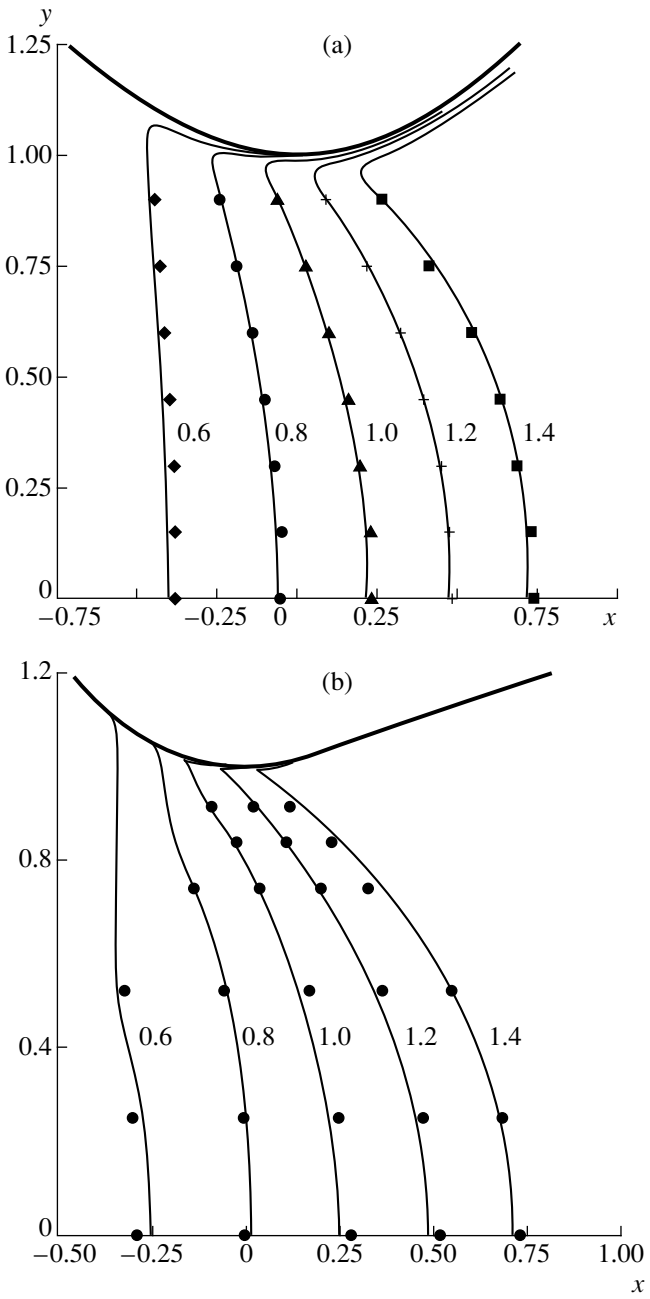


**Fig. 2.** Isolines for the Mach numbers M: (a) $K_w = 1.0$ and (b) 1.6. Calculation results and experimental data are shown by solid lines and by dots, respectively. Ciphers near the curves indicate values of M.

The upstream-perturbation propagation was efficiently taken into account by smoothing [13] values of $\tan\theta$ and $\left(\frac{\partial p}{\partial \xi}\right)^0$ along longitudinal coordinate lines before performing algorithm first and second steps, respectively.

The finite-difference scheme used in integrating at the first and second steps has the fourth and second orders of accuracy with respect to the $\eta$- and $\xi$-coordinates, respectively. A nonuniform network, concen-

trated towards both the wall and critical nozzle section, was used in the calculations.

The convergence rate of the global iterations is illustrated in Fig. 1 by the example for the distribution of $\tan\theta$ along that longitudinal-coordinate line near which maximum values of $\tan\theta$ are attained in each nozzle cross section. As is seen, two to four iteration steps are sufficient to find the solution. In this case, two iteration steps are sufficient for calculating such characteristics as the flow rate and the nozzle thrust to within the accuracy of 0.01%.

**4. The results.** The accuracy of the model proposed is illustrated in Fig. 2 by comparing the calculated and experimental distributions of Mach-number isolines [14, 15] in the zone of the nozzle throat. Figure 2a corresponds to the air flow with $\mathrm{Re}_r = 10^4$ in a conic nozzle with the opening half-angles of 30° for the narrowing and broadening cones and the throat curvature $K_w = 1.0$. Figure 2b relates to air flow with $\mathrm{Re}_r = 10^6$ in a conic nozzle with opening half-angles of 45° and 15° for narrowing and broadening cones, respectively, and the throat curvature $K_w = 1.6$. It is seen that the results of computations and experimental data are in the excellent agreement.

Thus, in the case of structureless viscous flows, the accuracy of the improved (elliptic) smooth-duct model is not worse than for the exact Navier–Stokes equations. The iterating-marching algorithm proposed reduces the computer time required for solving the Laval-nozzle direct problem by the factor of several tens, and for flows of chemically reacting mixtures—by the factor of several hundreds.

## ACKNOWLEDGMENTS

This work was supported by the Russian Foundation for Basic Research, project no. 97-01-00005.

## REFERENCES

1. U. G. Pirumov and G. S. Roslyakov, *Gas Flow in Nozzles* (Mos. Gos. Univ., Moscow, 1978).
2. Yu. V. Lapin and M. Kh. Strelets, *Internal Flows of Gas Mixtures* (Nauka, Moscow, 1989).
3. A. P. Byrkin and A. I. Tolstykh, Zh. Vych. Mat. Mat. Fiz. **28**, 1234 (1988).
4. Yu. É. Egorov, M. Kh. Strelets, and M. L. Shur, Mat. Model. **2**, 3 (1990).
5. A. S. Kiselev and L. E. Sternin, Zh. Vych. Mat. Mat. Fiz. **39**, 154 (1999).
6. D. A. Anderson, J. C. Tannehill, and R. H. Pletcher, *Computational Fluid Mechanics and Heat Transfer* (Hemisphere, New York, 1984; Mir, Moscow, 1990), Vol. 2.
7. V. G. Lushchik, V. I. Sizov, and A. E. Yakubenko, Teplofiz. Vys. Temp. **31**, 752 (1993).
8. B. V. Rogov and I. A. Sokolova, Dokl. Akad. Nauk **345**, 615 (1995) [Phys.–Dokl. **40**, 654 (1995)].
9. B. V. Rogov and I. A. Sokolova, Dokl. Akad. Nauk **357**, 190 (1997) [Phys.–Dokl. **42**, 619 (1997)].
10. N. N. Kalitkin, B. V. Rogov, and I. A. Sokolova, Dokl. Akad. Nauk **357**, 339 (1997) [Phys.–Dokl. **42**, 628 (1997)].
11. B. V. Rogov and I. A. Sokolova, AIAA Pap., No. 98,2493 (1998).
12. N. N. Kalitkin, B. V. Rogov, and I. A. Sokolova, Mat. Model. **11**, 95 (1999).
13. V. L. Kovalev, A. A. Krupnov, and G. A. Tirskiĭ, Dokl. Akad. Nauk **338**, 333 (1994) [Phys.–Dokl. **39**, 665 (1994)].
14. J. C. Dutton and A. L. Addy, AIAA J. **19**, 801 (1981).
15. R. F. Cuffel, L. H. Back, and P. F. Massier, AIAA J. **7**, 1364 (1969).

*Translated by V. Devitsyn*

*Doklady Physics, Vol. 45, No. 1, 2000, pp. 37–41. Translated from Doklady Akademii Nauk, Vol. 370, No. 2, 2000, pp. 181–185.*


**MECHANICS**

# Stress Singularity in Polyhedral Corner Points in the Case of Elastic Different-Modulus Joints

**N. V. Glushkova*, E. V. Glushkov*, and R. Hoff****

Presented by Academician V.A. Babeshko March 18, 1999

Received April 5, 1999

**1.** It is well known that solutions to the boundary value problems of the elliptic type and, in particular, to equations of linear elasticity theory have the following asymptotic representation in a neighborhood of boundary corner points [1]:

$$\boldsymbol{\tau} \sim \sum_k K_k \mathbf{f}_k r^{-\gamma_k}, \quad r \to 0,$$

$$c > \mathrm{Re}\gamma_1 > \mathrm{Re}\gamma_2 > \ldots > \mathrm{Re}\gamma_k > \ldots$$

(or a more complicated representation with logarithmic terms in the case of multiple spectrum points $\gamma_k$). Here, $r$, $K_k$, and $\mathbf{f}_k$ are the distance to the vertex, intensity coefficients, and functions defining the angular distribution of the stress field $\boldsymbol{\tau}$ in the neighborhood of the vertex, respectively. In the two-dimensional and three-dimensional cases, the functions $\mathbf{f}_k$ depend on one polar angular variable $\varphi$, $c = 1$, and two variables $\varphi$, $\psi$, $c = 2/3$, respectively.

In the two-dimensional case, the characteristics of the stress concentration [the values of the singularity indices $\gamma_k$ and the form of the functions $\mathbf{f}_k(\varphi)$] at corner points of linear-elastic bodies, including those of different-modulus joints, are investigated almost exhaustively. However, the problem of extracting singular components of the solution in the neighborhood of the vertex of polyhedral angles remains urgent. In contrast to the two-dimensional case, the characteristic equations for the determination of indices $\gamma_k$ (the spectrum points of corresponding boundary value problems) and the functions $\mathbf{f}_k(\varphi, \psi)$ (fundamental solutions) cannot be written here in an explicit form. For their determination, numerical approaches are used that imply the digitization in a certain way of the initial boundary value problem. In accordance with the number of variables needed for discretization, these approaches can be divided into three following groups:

(i) the direct approximation by the finite-element methods (FEM) (three variables);

(ii) the boundary-element method (BEM) [2], as well as approaches based on isolating the factor $r^\gamma$ in the explicit form (in fact, it is equivalent to application of the Melline transform to the initial three-dimensional boundary value problem) with a subsequent discretization with respect to two angular variables of a local spherical coordinate system [3–5]. This approach consisting in iterative refinement of the singularity characteristics, while approaching a vertex [6], is also two-dimensional;

(iii) the reduction of initial two-dimensional boundary integral equations (BIE) to one-dimensional integral equations by application of the Melline transform [7–12].

Mathematically, the first approach is simple but leads to large-scale systems of linear algebraic equations (on the order of 10000–20000 and higher) due to the necessity to refine a calculation net as the vertex is approached. Therefore, solving these systems calls for large computational expenditures. In the second case, we deal with systems on the order of 500–2000 that implies the use of middle-power computers. Concrete characteristics of singularities known at the present time are relatively sparse and were obtained, mainly, with making use of the second approach. In the first turn, these are the singularity indices for convex [3], and not only rectangular but also oblique trihedrons [6] and cracks reaching the surface [4, 5]. In connection with this, it is worth mentioning that in [2], numerical estimates of singularity indices for two coupled different-modulus trihedrons were obtained by analyzing the slope of characteristics for the stress field. Such trihedrons are considered in the present paper.

The third approach for determining the singularity of contact stresses at the vertex of a wedge-shaped press tool was put forward by V. A. Babeshko [7] and generalized later to the cases of wedge-shaped fractures [8], cracks reaching the surface [9], and arbitrary poly-

* *Kuban' State University, ul. Karla Libknekhta 9, Krasnodar, 350640 Russia*

** *Karlsruhe University (TH), Post Office box 36 40, D-76021, Karlsruhe, Germany*

1028-3358/00/4501-0037$20.00 

hedral angles [10]. This approach implies the application of a sufficiently complicated mathematical technique, but leads to almost explicit formulas convenient for calculations, which do not call for a considerable computational expenditures even in the case of using a personal computer. The general scheme of the method is described in detail in [11]. The key element providing the efficient use of this method is the representation of elements of the matrix-kernel for BIE in the form of series with isolated radial and angular variables, which considerably facilitates the application of the Melline transform and the subsequent discretization according to the Galerkin scheme. We note that the acceleration of the convergence of the series attained by isolating in the explicit form and summing up terms describing the asymptotic behavior at infinity, in fact, eliminate the computational expenditures for the system formation. In addition, a proper choice of basis functions ensuring the correct description of the behavior on edges, i.e., at the ends of intervals of the polar-angle variations on each of the faces, is of great importance.

The latter argument is essential for the convergence of the method, especially in the case when the solutions also have singularities on edges. For example, this takes place while changing the type of boundary conditions in the case when one face of a polyhedron is fixed or cemented to the face of another one. In the preceding papers [7–11], the orthogonal Jacobi polynomials with the weight ensuring the required behavior on edges were used as a basis. One of distinctive features of the approach [12] most close to that developed by us is the use as a basis of step splines ignoring the solution's behavior on edges.

The acceleration of the convergence of the series and the proper choice of coordinate functions provide more than raising the efficiency of the method. The computational practice shows that without them, we cannot manage in obtaining true results. For example, the plots for the dependence of the singularity indices at the vertex of a trihedral pyramid on the angle opening, which are presented in [10, 11], were determined in that time with too large error. Only initial and final values coinciding with those in particular cases of a press tool and a dihedral angle were correct. Unfortunately, this was not revealed appropriately due to the lack of independent results for intermediate values. In addition, extra roots corresponding to removable singularities are shown in the plots presented in [10, 11].

The modified scheme for the determination of a singularity in the vertex of a convex polyhedron was developed, which made it possible, for the first time within this approach, to obtain stable and exact results for not only homogeneous bodies but composite bodies as well. The reliability and accuracy of calculations were verified by the systematic comparison with the results obtained by the BEM. In this paper, we present both a brief description of principal distinctions for this new scheme and results of numerical analysis.

**2.** Previously [10, 11], the system of BIE for the neighborhood of the vertex of a polyhedral angle was derived on the basis of the superposition of integral representations of auxiliary solutions for half-spaces bounded by surfaces that coincide with the faces. In this paper, the classical approach based on the Betti–Somiliagno formula for the displacement field $\mathbf{u}(\mathbf{x})$ in an elastic body was used:

$$\mathbf{u}(\mathbf{x}) = \sum_{m=1}^{M} [G_m \boldsymbol{\tau}_m - H_m \mathbf{u}_m](\mathbf{x}). \tag{1}$$

Here $\boldsymbol{\tau}_m$ and $\mathbf{u}_m$ are the stress vector and displacement vector on the body surface (in our case, on the wedge faces $S_m$ of a $M$-hedral angle); $G_m$ and $H_m$ are well-known matrix integral operators acting on $\boldsymbol{\tau}_m$ and $\mathbf{u}_m$. Their kernels are expressed in terms of the matrix for fundamental solutions to Lamé equations.

Passing to the limit as $\mathbf{x} \longrightarrow \boldsymbol{\xi} \in S = \cup S_m$ and transferring terms with the given $\boldsymbol{\tau}_m$ or $\mathbf{u}_m$ to the right-hand side reduce (1) to BIE with respect to unknown surface displacements and/or stresses on faces. However, in contrast to the standard derivation of BIE, the Fourier transforms of their kernels (with respect to coordinates lying in the face planes) rather than the explicit form is used in the approach proposed. This saves from the necessity to deal with the kernel hypersingularity. On the other hand, this is a key point that allows us, as in [10, 11], to express the kernel elements in the form of series with isolated angular and radial variables. As was noted above, such a representation ensures the efficient realization of the method. Now, the degree of singularity of the kernel affects only the behavior of its Fourier image at infinity, or, what is the same, the degree of the convergence for the series. The procedure being used for the acceleration of their convergence is, in fact, equivalent to the kernel regularization.

For composed bodies, representation (1) is written out independently for each of polyhedrons in their own local coordinate systems. The matching conditions for displacements and stresses on common faces are added to this system of equations. For example, if two faces ($S_3$ and $\hat{S}_3$) of a trihedron are cemented together, then the BIE take the form

$$\begin{aligned} &\mathbf{u}_n + \sum_{m=1}^{3} (H_m^n \mathbf{u}_m) - G_3^n \boldsymbol{\tau}_3 = \mathbf{b}_n, \quad \mathbf{x} \in S_n, \\ &\hat{\mathbf{u}}_n + \sum_{m=1}^{3} (\hat{H}_m^n \hat{\mathbf{u}}_m) - \hat{G}_3^n \boldsymbol{\tau}_3 = \hat{\mathbf{b}}_n, \quad \hat{\mathbf{x}} \in \hat{S}_n, \\ &n = 1, 2, 3, \end{aligned} \tag{2}$$

with the contact conditions

$$\begin{aligned} \mathbf{u}_3(\mathbf{x}) &= P\hat{\mathbf{u}}_3(\hat{\mathbf{x}}), \\ \boldsymbol{\tau}_3(\mathbf{x}) &= -P\hat{\boldsymbol{\tau}}_3(\hat{\mathbf{x}}), \quad \mathbf{x} \in S_3, \quad \hat{\mathbf{x}} \in \hat{S}_3. \end{aligned} \tag{3}$$

Henceforth, quantities referring to the second trihedron are denoted by the cap superscript, $H_m^n$, $G_m^n$ and $\hat{H}_m^n$, $\hat{G}_m^n$ correspond to the integral operators on the faces $S_n$, $\hat{S}_n$ (i.e., at $\mathbf{x} \in S_n$ and $\hat{\mathbf{x}} \in \hat{S}_n$) for the first and second trihedrons, respectively;

$$\mathbf{b}_n = \sum_{m=1}^{2} G_m^n \boldsymbol{\tau}_m, \quad \hat{\mathbf{b}}_n = \sum_{m=1}^{2} \hat{G}_m^n \hat{\boldsymbol{\tau}}_m.$$

Here, $P$ is the matrix of the transfer between local coordinate systems.

The following stage consists in the application of the Melline transform $M_s$ (with respect to the parameter $r$) to equations (2), (3) obtained:

$$M_s[f] = \int_0^\infty f(r) r^{s-1} dr = F(s).$$

As a result, we reduce them to one-dimensional integral equations with respect to the Melline transform of unknown displacements $\mathbf{U}_m(s, \varphi_m) = M_s[\mathbf{u}_m]$ and stresses $\mathbf{T}_3(s+1, \varphi_3) = M_{s+1}[\boldsymbol{\tau}]$ ($\hat{\mathbf{U}}_m$ and $\hat{\mathbf{T}}_3$ are determined in a similar manner). Here $\varphi_m$ and $\hat{\varphi}_m$ are the polar angles on faces $S_m$ and $\hat{S}_m$, respectively. In the case of stresses, the shift of the transform parameters $s + 1$ is a consequence of the different homogeneity degree of the Fourier images for the operators $H_m$ and $G_m$: $G_m(t\alpha) = t^{-1}G_m(\alpha)$, while $H_m(t\alpha) = H_m(\alpha)$.

The principal distinction of the approach proposed from that developed in [10, 11] is the necessity to approximate not only $\mathbf{T}_m$ but also $\mathbf{U}_m$. While the Jacobi polynomials with the weight ensuring the desired behavior on edges,

$$p_k(t) = (1-t)^\alpha (1+t)^\beta P_k^{(\alpha,\beta)}(t), \quad \varphi = at + b, \quad t \in [-1, 1],$$

are the perfect basis for the expansion of stresses $\mathbf{T}_m$, a sole set of such functions does not ensure the proper description of the behavior of the displacements $\mathbf{U}_m$. This is explained by the fact that although the behavior of the derivatives of $\mathbf{U}'_m$ with respect to $\varphi$ is similar to that of stress components (i.e., can possess a weak singularity), the displacements themselves are bounded and, moreover, in contrast to stresses, they are continuous on edges. It is evident that the Jacobi polynomials cannot satisfy all these requirements simultaneously. It should be noted that the expansion of $\mathbf{U}_m$ in terms of two sets of Jacobi polynomials, such that the weight of one of which provides the required continuity on edges (the Legendre polynomials), while the other ensures the singularity of derivatives, leads to the numerical instability. The rapid and stable convergence of the method was attained only when the specific system of basis functions $q_{m,k}(\varphi)$, which satisfies all the requirements mentioned above, was constructed.

The expansion of unknowns in terms of basis functions $\{p_k^{(i)}\}_{k=0}^\infty$ and $\{q_{m,k}^{(i)}\}_{k=0}^\infty$, $i = 1, 2, 3$, being the number of the vector components, has the form

$$U_m^{(i)}(s, \varphi_m) \approx \sum_{k=0}^{N} c_{m,k}^{(i)}(s) q_{m,k}^{(i)}(\varphi_m), \quad m = 1, 2, 3,$$
$$T_3^{(i)}(s+1, \varphi_3) \approx \sum_{k=0}^{N} c_{4,k}^{(i)}(s) p_k^{(i)}(\varphi_3), \tag{4}$$

$\hat{U}_m$, $\hat{T}_3$ are expanded similarly and the subsequent projection, in accordance with the Galerkin scheme for the BIE residual, onto the system of the Legendre polynomials, $P_l(\varphi_n)$, $l = 1, 2, 3, \ldots, N$ lead, in our case, to the following linear algebraic system in unknown coefficients of the expansion $\mathbf{c}_{m,k}$, $\hat{\mathbf{c}}_{m,k}$:

$$\sum_{k=0}^{N} A_{lk}(s) \mathbf{c}_k(s) = \mathbf{b}_l(s), \quad l = 0, 1, \ldots, N. \tag{5}$$

Here, $\mathbf{c}_k = (\mathbf{c}_{1,k}, \mathbf{c}_{2,k}, \mathbf{c}_{3,k}, \mathbf{c}_{4,k}, \hat{\mathbf{c}}_{1,k}, \hat{\mathbf{c}}_{2,k})$ are the 18-component vectors; $\mathbf{c}_{m,k} = (c_{m,k}^{(1)}, c_{m,k}^{(2)}, c_{m,k}^{(3)})$ [unknown vectors $\hat{\mathbf{c}}_{3,k}$, $\hat{\mathbf{c}}_{4,k}$ corresponding to the face $\hat{S}_3$ are eliminated with the use of condition (3)];

$$A_{lk} = \begin{pmatrix} Q_1 + H_1^1 & H_2^1 & H_3^1 & -G_3^1 & 0 & 0 \\ H_1^2 & Q_2 + H_2^2 & H_3^2 & -G_3^2 & 0 & 0 \\ H_1^3 & H_2^3 & Q_3 + H_3^3 & -G_3^3 & 0 & 0 \\ 0 & 0 & \tilde{H}_3^1 & -\tilde{G}_3^1 & Q_1 + \hat{H}_1^1 & \hat{H}_2^1 \\ 0 & 0 & \tilde{H}_3^2 & -\tilde{G}_3^2 & \hat{H}_1^2 & Q_2 + \hat{H}_2^2 \\ 0 & 0 & \tilde{Q}_3 + \tilde{H}_3^3 & -\tilde{G}_3^3 & \hat{H}_1^3 & \hat{H}_2^3 \end{pmatrix}. \tag{6}$$

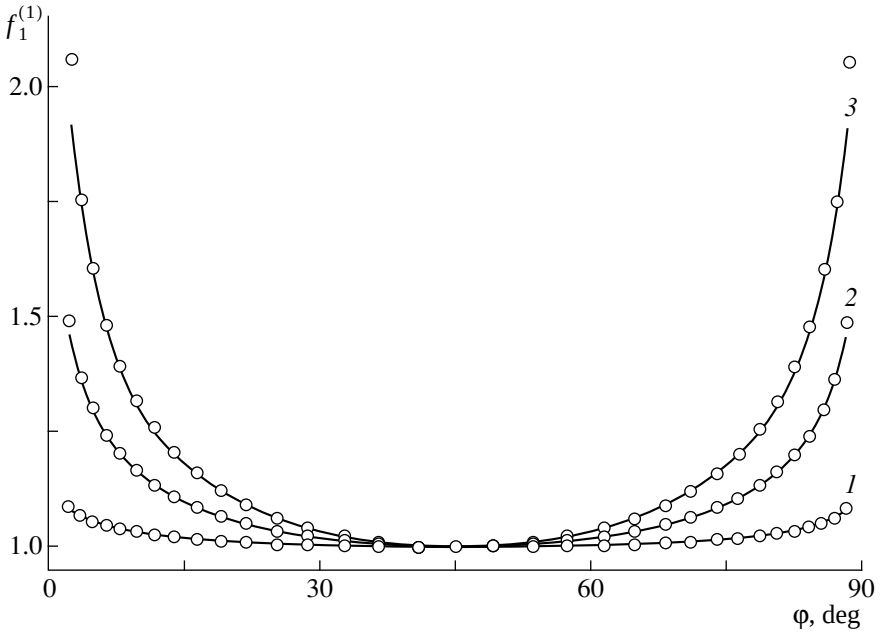


**Fig. 1.**

$Q_n$, $n$ = 1, 2, 3, are diagonal matrices arising while discretizing terms $\mathbf{U}_n$ and $\hat{\mathbf{U}}_n$ that stand outside the integral, [see (1)]. The matrix components $H_m^n$, $G_3^n$, $\hat{H}_m^n$, etc. are expressed in terms of the series $I_n(p_1, p_2)$. In the whole, the structure of series $I_n$ remains the same [9–11]; the differences consist only in constants $d_1(m, k)$ depending on the form of basis functions. The wavy superscript above $\tilde{H}_3^n$, $\tilde{G}_3^n$, $\tilde{Q}_3$ indicates the fact that transformations performed, in accordance with contact conditions (3), are taken into account, while eliminating unknowns $\hat{\mathbf{c}}_{3,k}$, $\hat{\mathbf{c}}_{4,k}$ in the matrices $\hat{H}_3$, $\hat{G}_3$, $Q_3$.

**Table**

| $E$ | ν | | | | |
|---|---|---|---|---|---|
| | 0.1 | 0.2 | 0.3 | 0.4 | 0.5 |
| 2 | 0.016 | 0.034 | 0.049 | 0.062 | 0.074 |
| 2.5 | 0.029 | 0.056 | 0.079 | 0.098 | 0.115 |
| 3 | 0.042 | 0.076 | 0.105 | 0.129 | 0.150 |
| 4 | 0.062 | 0.109 | 0.147 | 0.178 | 0.203 |
| 5 | 0.078 | 0.134 | 0.178 | 0.213 | 0.241 |
| 7 | 0.102 | 0.170 | 0.220 | 0.260 | 0.291 |
| 10 | 0.125 | 0.202 | 0.258 | 0.302 | 0.339 |
| 20 | 0.159 | 0.248 | 0.311 | 0.359 | 0.398 |
| 40 | 0.180 | 0.275 | 0.342 | 0.386 | 0.432 |
| 80 | 0.191 | 0.290 | 0.358 | 0.412 | 0.451 |
| 160 | 0.197 | 0.297 | 0.367 | 0.421 | 0.460 |
| 320 | 0.201 | 0.301 | 0.371 | 0.425 | 0.465 |
| 640 | 0.202 | 0.303 | 0.373 | 0.427 | 0.468 |

**3.** Being the poles of the Melline transform $\mathbf{T}_3(s, \varphi)$, the desired indices $\gamma_k$ of the stress singularities are approximated, with allowance for the shift of the argument $s + 1$, by the quantities $s_k + 1$, where $s_k$ are the zeros of the determinant of system (5). The intensity coefficients and angular functions are the residua at these poles [11]. These functions, with the accuracy to a constant factor, are expressed in terms of eigenvectors of the matrix $A(s_k)$ of system (5).

In order to verify the reliability of the method developed and evaluate its efficiency, numerical calculations for two rectangular parallelepipeds cemented together were performed simultaneously by this method and by that of boundary elements (the BEASY package). The comparison of the results obtained has shown that, for $N = 5$ (the total system dimension is $90 \times 90$), to within $\pm 0.001$, the indices coincide with each other. Some of calculated values of $\gamma_1$ are shown in the table for different ratios of Young's moduli $E = E_2/E_1$ and equal Poisson's ratios $\nu_1 = \nu_2 = \nu$. At $E = \infty$ (a cube is cemented to a nondeformable base), the index $\gamma_1$ agrees exactly with values given in [6] for $\nu_1$ = 0; 0.1; 0.2; 0.3; 0.4. In the case of a different-modulus joint, our results also agree with those obtained in [2] by the BEM.

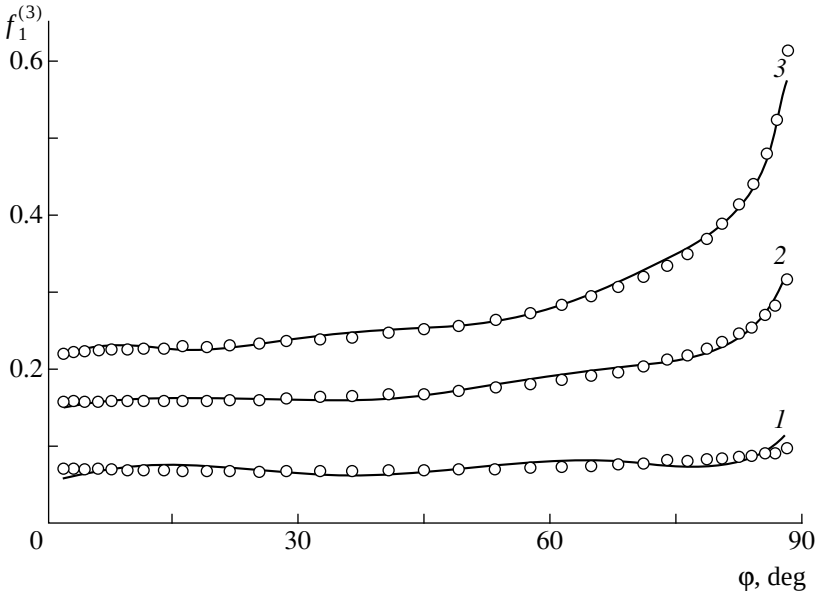


**Fig. 2.**

Plots of angular functions $f_1^{(1)}(\varphi)$ and $f_1^{(3)}(\varphi)$ normalized according to the condition $f_1^{(3)}(45°) = 1$ are shown in Figs. 1 and 2, respectively, for the stress components $\tau_{xz}$ and $\sigma_z$ in the contact zone $S_3$ in the case of $\nu_1 = \nu_2 = 0.3$, $E = 2, 7, \infty$ (lines *1*, *2*, *3*, respectively). Dots correspond to the values obtained by the BEM.

For a long time, the weak point of this method was the presence, apart of $\gamma_1$, of additional singularities, which were not revealed by other authors. For example, in the case of the cube vertex with one fixed face, three singular roots of the characteristic equation $\det A(s) = 0$ are obtained. For $\nu = 0.3$, these roots are $\gamma_k = 0.376$; 0.426; 0.597; and only the first of them can be found by the BEM. The analysis of the solution $\mathbf{c}(s)$ to system (5) as a function of $s$ has shown that, apart from poles $s_2$, $s_3$, there are zeros $z_2$, $z_3$ located very closely to the poles, which suppress them as a result of merging as $N \longrightarrow \infty$. It is interesting to note that, in this case, the removable (in this problem) pole corresponding to the index $\gamma_3 = 0.597$ and its values for all other values of $\nu$ agree with the principal singularity index for the Fichera vertex [12] (The Fichera vertex corresponds to the entire space with exception of 1/8 part with faces free of stresses. Thus, from the geometry standpoint, this is a medium complementary to the rectangular trihedron that was under consideration in this paper).

## ACKNOWLEDGMENTS

The authors are grateful to prof. V.A. Babeshko and prof. D. Munz for their help when performing this work.

This study was supported by the Integratsiya program, project no. 368, by the Russian Foundation for Basic Research, project no. 98-01-049091 and by the DFG, project no. 436 RUS 113/130/0(R).

## REFERENCES

1. V. A. Kondrat'ev, Trudy MMO **16**, 209 (1967).
2. H. Koguchi, Int. J. Solids Struct. **34**, 461 (1997).
3. V. P. Matveenko and S. G. Minakova, Abstracts of Papers, *All-USSR Conf. Modern Problems of Informatics, Computer Science, and Automation, Tula, 1988*, pp. 38–42.
4. F. Ghahremani and C. F. Shih, Trans. ASME, J. Appl. Mech. **59**, 61 (1992).
5. D. Leguillon, in *Lectures and Notes in Pure and Applied Mathematics* (Dekker, New York, 1995), Vol. 167, pp. 161–170.
6. R. W. Thatcher, in *Proceedings of Conference on CIRM* (M. Dekk, New York, 1995), pp. 285–298.
7. V. A. Babeshko, E. V. Glushkov, and N. V. Glushkova, Dokl. Akad. Nauk SSSR **257**, 289 (1981) [Soviet Phys.–Dokl. **26**, 290 (1981)].
8. E. V. Glushkov and N. V. Glushkova, Izv. Akad. Nauk SSSR, Ser. Mekh. Tv. Tela, No. 4, 82 (1992).
9. E. V. Glushkov, N. V. Glushkova, and O. N. Lapina, Izv. Akad. Nauk SSSR, Ser. Mekh. Tverd. Tela, No. 5, 146 (1998).
10. V. A. Babeshko, E. V. Glushkov, N. V. Glushkova, *et al*., Dokl. Akad. Nauk SSSR **318**, 1113 (1991) [Soviet Phys.–Dokl. **36**, 445 (1991)].
11. E. Glushkov, N. Glushkova, and O. Lapina, Int. J. Solids Struct. **36**, 1105 (1999).
12. H. Schmitz, K. Volk, and W. Wendland, Numer. Meth. Part. Diff. Equat **9**, 323 (1993).

*Translated by V. Devitsyn*

*Doklady Physics, Vol. 45, No. 1, 2000, pp. 42–45. Translated from Doklady Akademii Nauk, Vol. 370, No. 2, 2000, pp. 186–189.*


**MECHANICS**

# The Motion of a Flat Linkage over a Horizontal Plane

**Academician F. L. Chernous'ko**

Received September 7, 1999

We investigate the dynamics of a flat linkage moving over a rough horizontal plane under the action of both internal controlling torques applied in the hinges and the forces of dry friction between the linkage and the plane. We elaborated the modes of motion providing an arbitrary preset displacement of the linkage as a whole: the longitudinal and lateral motions and the on-the-spot turn. A velocity of these motions was estimated. The forms of motions found can serve as a model of the movement of snakes and certain other animals and also can be useful in designing mobile robots.

**1.** We consider a flat linkage, which is on a horizontal plane and is actuated by controlling torques applied in its hinges. The example of snakes and some other animals shows that such a system can very efficiently move over a plane by bending and using the forces of friction on the plane. Various aspects of the biomechanics of snakes and also the problems of mechanics of robots, which use the principles of movement of snakes, were discussed in [1–3]. Here, we propose a simple mechanical model of this manner of motion.

A flat three-link linkage $O_1C_1C_2O_2$ consists of a central link $C_1C_2$ with length $2a$ and two links $O_1C_1$ and $O_2C_2$ of length $l$ each (see Fig. 1). For simplicity, we take that the links are absolutely solid and imponderable rods, and the total mass of this three-link linkage is concentrated at the points $O_1$, $C_1$, $C_2$, and $O_2$. The mass of the points $O_1$ and $O_2$ is equal to $m_0$ each, and that of the points $C_1$ and $C_2$ is equal to $m_1$ each. Thus, the total mass of the linkage is equal to $m = 2(m_0 + m_1)$. We refer to the link $C_1C_2$ together with the masses concentrated in the hinges $C_1$ and $C_2$ as a body, and to the links $O_1C_1$ and $O_2C_2$ together with the end masses as the end links.

The linkage can move over an immobile rough horizontal plane on which the Cartesian system of coordinates $Oxy$ is introduced. The Cartesian coordinates of the center of the body are denoted by $x$ and $y$, while the angles of inclination of the links $O_1C_1$, $C_1C_2$, and $C_2O_2$ with respect to the $x$-axis are designated as $\theta_1$, $\theta$, and $\theta_2$, respectively. We set $\theta_i = \theta + \alpha_i$ ($i$ = 1, 2), where $\alpha_i$ are the angles between the body and the end links $O_iC_i$, respectively.

The forces of dry friction, obeying the Coulomb law, act between the points $O_i$, $C_i$ ($i$ = 1, 2) and the plane. At rest, the forces of friction do not exceed $m_igk$, where $m_i$ is the mass of a point, $g$ is the gravity acceleration, and $k$ is the friction coefficient. During the motion of the point, this force is equal to $m_igk$ and is in opposition to the velocity of the point.

In the hinges $C_1$ and $C_2$, the controlling torques $M_1$ and $M_2$ act; these torques can be varied in an arbitrary preset way.

**2.** In order to obtain an arbitrary preset displacement of the linkage over a plane, it is sufficient to construct its motion along the linkage itself (the longitudinal motion) and transverse to this direction (the lateral motion), and also to build the on-the-spot rotation. We form these motions from simpler motions, which are termed elementary. Every elementary motion starts from and terminates at a state of rest. Initial and final values of the angles $\alpha_i$ for every elementary motion are denoted by $\alpha_i^0$ and $\alpha_i^1$, respectively, $i$ = 1, 2. These motions are classified as slow and fast.

In slow motions, one or both end links rotate, while the body remains immobile. We take that the angular velocity of the end links $\dot{\alpha}_i$ ($i$ = 1, 2) does not alter the

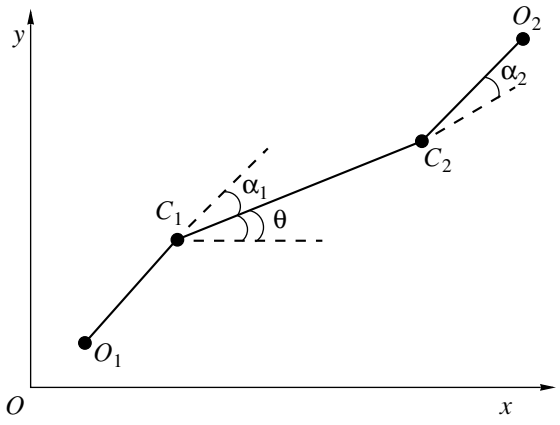


**Fig. 1.**

*Institute for Problems in Mechanics,*
*Russian Academy of Sciences,*
*pr. Vernadskogo 101, Moscow, 117526 Russia*

1028-3358/00/4501-0042$20.00 

sign for the slow motion, and the following relationships are valid:

$$\begin{aligned} \omega(t) &= \varepsilon_0 t, \quad t \in [0, T/2], \\ \omega(t) &= \varepsilon_0 (T - t), \quad t \in [T/2, T], \\ \omega &= |\dot{\alpha}_i|, \quad \Delta\alpha_i = \alpha_i^1 - \alpha_i^0, \\ |\Delta\alpha_i| &= \omega_0 T/2, \quad i = 1, 2, \quad \omega_0 = \varepsilon_0 T/2. \end{aligned} \tag{1}$$

Here, $t$ is the time, $T$ is the duration of the slow motion, and $\omega_0$ and $\varepsilon_0$ are constants. If both of the end links are involved in the slow motion, they rotate synchronously either in the same directions or in the opposite ones, so that

$$\alpha_2(t) = \pm\alpha_1(t) + \beta, \quad t \in [0, T], \tag{2}$$

where $\beta$ is a constant. It can be shown that, in order for the body be immobile during the slow motion of one or both end links, it is sufficient that the following conditions be fulfilled:

$$m_0 l[\sqrt{2}(\omega_0^4 + \varepsilon_0^2)^{1/2} + (\varepsilon_0 l + gk)a^{-1}] \le m_1 gk. \tag{3}$$

If the end links have an opposite sense of rotation, i.e., there is a minus sign in (2), it is sufficient that, instead of (3), the following conditions be fulfilled:

$$m_0 l(\omega_0^4 + \varepsilon_0^2)^{1/2} \le m_1 gk. \tag{4}$$

If the end links rotate reasonably slow, i.e., $\omega_0$ and $\varepsilon_0$ are sufficiently small in (1), inequality (4) will always be fulfilled, whereas inequality (3) will be fulfilled for $m_0 l < m_1 a$.

In fast motions, the angular velocities and accelerations are reasonably high, and the time of motion is small as compared with the time of slow motions. In this case, the controlling torques $M_1$ and $M_2$ are much higher than the moments of forces of friction, which are equal to $\mu gkL$, where $\mu = \max(m_0, m_1)$ and $L = \max(l, a)$. Thus, the forces of friction can be ignored. Here, condition (2) is fulfilled as before, with one of the three cases taking place:

(1) $\alpha_2(t) = -\alpha_1(t) + \beta$ and, moreover, either $\alpha_1^0 = 0$, or $\alpha_2^0 = 0$;

(2) $\alpha_2(t) = -\alpha_1(t)$;

(3) $\alpha_2(t) = \alpha_1(t)$.

These cases will be referred to as the fast motions of the types 1–3, respectively. The law of variation of angular velocities is inessential for the fast motions.

Using the laws of conservation of momentum and angular momentum, it can be shown that the increments of the variables $x$, $y$, and $\theta$ for the fast motion of the type 1 are equal to

$$\begin{aligned} \Delta x &= \mp 4 m_0 m^{-1} l \sin^2(\beta/2), \\ \Delta y &= \pm 2 m_0 m^{-1} l \sin\beta, \quad \Delta\theta = 0. \end{aligned} \tag{5}$$

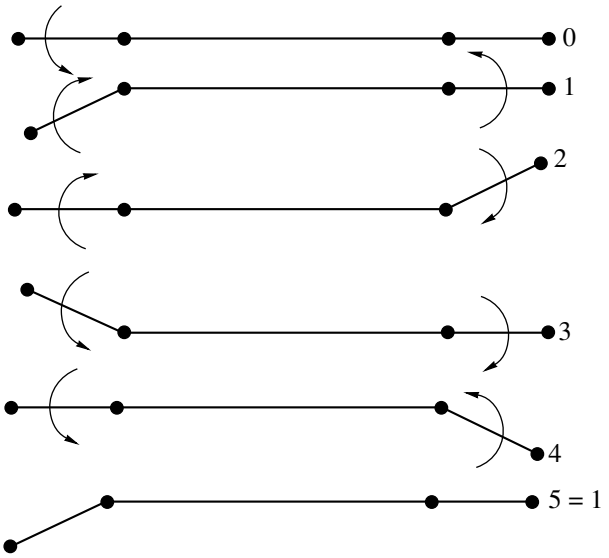


**Fig. 2.**

Here, the upper and lower signs correspond to the cases $\alpha_1^0 = 0$ and $\alpha_2^0 = 0$, respectively. For motion of the type 2, we obtain

$$\Delta x = 0, \quad \Delta y = 2 m_0 m^{-1} (\sin\alpha_1^1 - \sin\alpha_1^0), \quad \Delta\theta = 0. \tag{6}$$

For motion of the type 3, we have $\Delta x = \Delta y = 0$, $\Delta\theta \ne 0$, an explicit expression having been found for $\Delta\theta$.

Let us pass to forming the longitudinal, lateral, and rotary motions of a linkage from elementary motions.

**3. Longitudinal motion.** We assume that at the initial moment a linkage is of a rectilinear shape ($\theta = \alpha_1 = \alpha_2 = 0$) and is at rest (the state 0 in Fig. 2). The following motions will be executed:

(1) A slow motion by rotating the link $O_1C_1$ through an angle $\beta$. The other links remain immobile. The linkage passes into the state 1 in Fig. 2, in which $\alpha_1 = \beta$ and $\alpha_2 = 0$.

(2) A fast motion of the type 1, as a result of which $\alpha_1$ and $\alpha_2$ vary from $\beta$ to 0 and from 0 to $\beta$, respectively. The linkage passes into the state 2 in Fig. 2.

(3) A slow motion such that the angles $\alpha_1$ and $\alpha_2$ vary from 0 to $-\beta$ and from $\beta$ to 0, respectively. The linkage passes into the state 3 in Fig. 2.

(4) A fast motion of the type 1 such that the angles $\alpha_1$ and $\alpha_2$ vary from $-\beta$ to 0 and from 0 to $-\beta$, respectively. The linkage passes into the state 4 in Fig. 2.

(5) A slow motion such that the angles $\alpha_1$ and $\alpha_2$ vary from 0 to $\beta$ and from $-\beta$ to 0, respectively. The linkage passes into the state 5 in Fig. 2.

The state 5 is identical to the state 1. The described cycle of two fast and two slow motions can be repeated an arbitrary number of times. In order to transfer the linkage from the state 5 to the rectilinear state 0 at the

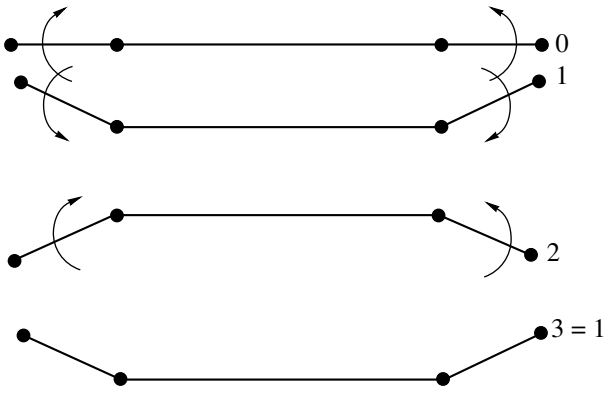


**Fig. 3.**

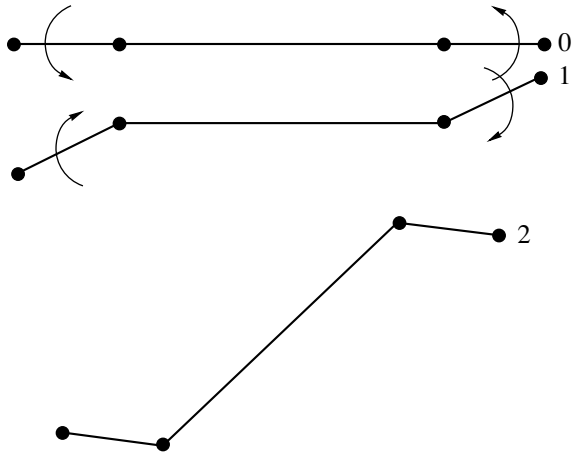


**Fig. 4.**

end of the motion, it is necessary to execute a slow motion by varying $\alpha_1$ from $\beta$ to 0.

Let us calculate the total displacement of the linkage in one cycle of the motion. Because $\alpha_2^0 = 0$ for the both fast motions of the cycle, it is necessary to take the lower signs in formulae (5), with $\beta$ having opposite signs for these motions. For the total displacement, we obtain

$$\Delta_0 x = 8m_0 m^{-1} l \sin^2(\beta/2), \quad m = 2(m_0 + m_1),$$
$$\Delta_0 y = \Delta_0 \theta = 0.$$

A mean velocity of the longitudinal motion $v_1 = \Delta_0 x(2T)^{-1}$, where the time $T$ of slow motion and the angle $\beta$ must satisfy the inequality

$$m_0 l[4\sqrt{2}\beta(\beta^2 + 1)^{1/2} T^{-2} + (4\beta l T^{-2} + gk)a^{-1}] \le m_1 gk,$$

which follows from (1) and (3).

**4. Lateral motion.** We start the motion once again from the state of rest (the state 0 in Fig. 3) and execute the following motions:

(1) A slow motion by varying the angles $\alpha_1$ and $\alpha_2$ from 0 to $-\beta$ and from 0 to $\beta$, respectively. The linkage passes into the state 1 in Fig. 3.

(2) A fast motion by varying the angles $\alpha_1$ and $\alpha_2$ from $-\beta$ to $\beta$ and from $\beta$ to $-\beta$, respectively. The linkage passes into the state 2 in Fig. 3.

(3) A slow motion by varying the angles $\alpha_1$ and $\alpha_2$ from $\beta$ to $-\beta$ and from $-\beta$ to $\beta$, respectively. The linkage passes into the state 3 in Fig. 3.

The state 3 is identical to the state 1. The cycle involving the fast and slow motions can be repeated. In order to bring the linkage from the state 3 to the initial state 0 at the end of the motion, it is sufficient to execute the slow motion by varying the angles $\alpha_1$ and $\alpha_2$ from $-\beta$ to 0 and from $\beta$ to 0, respectively.

The total displacement of the linkage in the cycle is determined employing formulas (6). We have

$$\Delta_0 x = 0, \quad \Delta_0 y = 4m_0 m^{-1} l \sin\beta, \quad \Delta_0 \theta = 0.$$

The mean velocity of the lateral motion $v_2 = \Delta_0 y T^{-1}$, where the time $T$ of the slow motion and the angle $\beta$ must satisfy the inequality

$$8m_0 l\beta(4\beta^2 + 1)^{1/2} T^{-2} \le m_1 gk,$$

which follows from (1) and (4).

**5. Turn.** In order to turn the linkage, which is initially at the state 0 in Fig. 4, we execute the following motions (here always, $\alpha_1 \equiv \alpha_2$).

(1) By means of the slow motion, we vary $\alpha_1 = \alpha_2$ from 0 to $\alpha^0$. The linkage passes into the state 1 in Fig. 4.

(2) By means of the fast motion of the type 3, we vary $\alpha_1 = \alpha_2$ from $\alpha^0$ to $\alpha^1$. In this case, the body turns through the angle $\Delta\theta$, and the linkage passes into the state 2 in Fig. 4.

These motions can be repeated. In order to bring the linkage from the state 2 to the rectilinear state, it is necessary to execute a slow motion by varying $\alpha_1 = \alpha_2$ from $\alpha^1$ to 0. As a result, the linkage turns on-the-spot through an angle $\Delta\theta$.

**6.** As an example, we take numerical values for the parameters: $\beta = 30°$, $k = 0.3$, $g = 9.81$ m s$^{-2}$, $m_0 = 0.5$ kg, $m_1 = 0.7$ kg, $a = l = 0.1$ m, and $T = 1$ s. It can be shown that all the conditions imposed are fulfilled in this case, and the mean velocities of the longitudinal and lateral motions are equal to $v_1 = 0.5$ cm s$^{-1}$ and $v_2 = 2$ cm s$^{-1}$, respectively. For realizing these motions, the torques $M_1$ and $M_2$, developed by the motors, must be of the order of 0.1 N m.

**7.** It is shown that the flat linkage can move over a rough horizontal plane in an arbitrary direction and turn

under the action of internal controlling torques applied to its hinges. Simple constructional ways for realizing these motions are proposed, sufficient conditions of their feasibility are given, and displacements and velocities are estimated.

A computer simulation, with all the factors taken into account more accurately and completely, confirmed a feasibility of the motions described for the linkage.

The distinguishing features of this manner of motion as compared with other ways of displacing vehicles and animals using wheels, legs, or caterpillar tracks are noteworthy.

(1) The motions under consideration occur in a horizontal plane exceptionally; a body contacts with the plane all the time by the same points. All the points of the body move parallel to this plane, while the controlling torques are perpendicular to it. Therefore, the vertical dimensions of the body (the height of a vehicle) can be small. As to the height of a wheel or stepping vehicle, it is bounded from below by dimensions of the wheels or legs.

(2) For realizing arbitrary motions, it is sufficient to have two independent motors mounted in hinges (for a stepping vehicle, it is necessary to have no less than two motors for each leg).

(3) The design of the vehicle and the mode of its motion are very simple.

These features can be useful in designing small-dimension mobile robots.

## ACKNOWLEDGMENTS

This work was supported by the Russian Foundation for Basic Research, project no. 99-01-00258.

## REFERENCES

1. A. I. Dobrolyubov, *Traveling Waves of Deformation* (Nauka i Tekhnika, Minsk, 1987).
2. S. Hirose, *Biologically Inspired Robots. Snake-Like Locomotors and Manipulators* (Oxford Univ. Press, Oxford, 1993).
3. J. Ostrowskĭ and J. Burdick, in *Proceedings of 1996 IEEE International Conference on Robotics and Automation* (Minneapolis, Minn., 1996), Vol. 2, p. 1294.

*Translated by V. Bukhanov*

*Doklady Physics, Vol. 45, No. 1, 2000, pp. 5–10. Translated from Doklady Akademii Nauk, Vol. 370, No. 1, 2000, pp. 38–42.*


**PHYSICS**

# On a Possibility to Reduce the Ignition Threshold for Combustible Mixtures by Selective Excitation of Molecular Vibrations in Initial Reagents

**A. M. Starik and N. S. Titova**

Presented by Academician O.N. Favorskiĭ April 26, 1999

Received May 5, 1999

In recent years, a possibility to control combustion processes, while exciting vibrational degrees of freedom in molecules was subjected to sufficiently wide discussions in literature [1–4]. It was shown that the excitation of vibrations in $H_2$, $O_2$, and even $N_2$ results in both intensifying formation of active O, H, and OH centers and accelerating the combustion of the $H_2$ + air mixture. In this study, we investigate another aspect of the problem, which is associated with the effect of exciting molecular vibrations of initial reagents on the self-ignition threshold.

First, we show for the general case that the selective excitation of molecular vibrational degrees of freedom in the case of the chain mechanism of the process must result in reducing the self-ignition threshold. We will assume that the thermodynamic equilibrium exists between the rotational and translational molecular degrees of freedom, while a local Boltzmann distribution with its proper vibrational temperature $T_\xi$ ($\xi = 1, \ldots, n$) is established very rapidly in each $\xi$th mode.

The simplest scheme of reactions describing the initiation (the appearance of an active radical), propagation, and the break of a chain has the form:

(I) $A \xrightarrow{k_1} r + D$,

(II) $r + A \xrightarrow{k_2} C + lr$,

(III) $r + r \xrightarrow{k_3} r_2$.

Here, $A$ is an initial reagent, whose decomposition leads to the formation of an active radical; $r$; $C$, $D$, and $r_2$ are reaction products; $l = 1$ and $l = 2, 3$ correspond to a nonramified and ramified chain reactions, respectively; $k_1$, $k_2$, and $k_3$ are the reaction-rate constants for the corresponding process. The equations specifying the formation of active radicals $r$ in the processes I–III can be represented in the form:

$$\frac{d[A]}{dt} = -k_1[A] - k_2[r][A], \tag{1}$$

$$\frac{d[r]}{dt} = k_1[A] + (l-1)k_2[r][A] - 2k_3[r]^2. \tag{2}$$

We seek the solution for $[r]$ in the form [5]:

$$[r] = \frac{y'(t)}{2k_3 y(t)}. \tag{3}$$

Here, $[A]$ and $[r]$ are the concentrations of molecules for the mixture components $A$ and $r$, and $y(t)$ is a certain continuous function of time.

Substituting (3) into (2), we obtain

$$y''(t) - (l-1)k_2[A]y'(t) - 2k_3k_1[A]y(t) = 0.$$

In the general case, $k_1$, $k_2$, and $k_3$ depend on the gas temperature $T$, while $k_1$ and $k_2$ depend also on the vibrational temperature $T_V$ for the molecule excited mode of the component $A$. The values of $T$, $T_V$, and $[A]$ vary in the process of combusting the mixture. However, within the range $[0, \tau_{in}]$, where $\tau_{in}$ is the induction period, we may assume that $T = T_0$, $T_V = T_{V0}$, and $[A] = [A]_0$ (the subscript zero corresponds to $t = 0$). In this case, we have for $[r(t)]$ that

$$[r(t)] = \frac{C_1 Z_1 e^{Z_1 t} + C_2 Z_2 e^{Z_2 t}}{2k_3(C_1 e^{Z_1 t} + C_2 e^{Z_2 t})}, \tag{4}$$

$$Z_{1,2} = \frac{b}{2} \pm \sqrt{\left(\frac{b}{2}\right)^2 + a^2}, \quad a^2 = 2k_1k_3[A]_0,$$

$$b = (l-1)k_2[A]_0,$$

where $C_1$ and $C_2$ are the integration constants. If $[r]_0 = 0$

*Central Institute of Aircraft Engine Building, Aviamotornaya ul. 2, Moscow, 111250 Russia*

1028-3358/00/4501-0005$20.00 

for $t = 0$, then

$$[r(t)] = \frac{Z_1 Z_2 (e^{Z_1 t} - e^{Z_2 t})}{2k_3 (Z_2 e^{Z_1 t} - Z_1 e^{Z_2 t})}. \quad (5)$$

As $t \longrightarrow \infty$, it follows from (5) that $[r(t)] = Z_1/2k_3$.

For $l = 1$ (a nonramified chain reaction),

$$[r(t)] = \frac{1 - e^{-2at}}{1 + e^{-2at}} \sqrt{\frac{[A]_0 k_1}{2k_3}}.$$

For $t > t_*$, $t_* = (2a)^{-1}$, the value $[r]$ tends to its ultimate value $[r_*] = \sqrt{[A]_0 k_1/2k_3}$. In the case of a ramified chain reaction ($l > 1$), $k_2^2 [A]_0/k_1 k_3 \gg 1$, and the maximum concentration of active radicals (furthermore, we denote it by the subscript $l$) is defined by the expression $[r_*]_l = (l-1)k_2[A]_0/2k_3$. Since $k_2 > k_1$, then $[r_*]_l > [r_*]$.

The self-ignition regime is realized if $[r_*] > [r_{ign}]$, where $[r_{ign}]$ is the critical concentration of active radicals for which the chain mechanism develops steadily [6]. The value of $[r_{ign}]$ depends on $[A]_0$, on the rates of formation and disintegration of active radicals, and on the rate of their diffusion or convective outflow from the reaction zone. The quantity $[A]_0$ determines the concentration threshold for the self-ignition, while the relationship between $k_1$, $k_2$, and $k_3$ determines the temperature threshold. The chemical-reaction rate constant for $T_\xi \neq T$ can be presented in the form

$$k_q(T, T_\xi) = \varphi_q(T, T_\xi) k_q^0(T), \quad (6)$$

where $k_q^0(T)$ is the reaction-rate constant for the $q$th reaction at $T_\xi = T$, and $\varphi_q(T, T_\xi)$ is the nonequilibrium-state factor. For determining a particular form of $\varphi_q(T, T_\xi)$, we use the theoretical results of [7]:

$$\varphi_q(T, T_\xi) = \frac{\prod_{j=1}^{b_q} [1 - \exp(-\theta_j/T_j)]^{-g_j}}{\prod_{j=1}^{b_q} [1 - \exp(-\theta_j/T)]^{-g_j}} \times \exp\left[\frac{E_q^*}{k}\left(\frac{1}{T} - \frac{\sum_{j=1}^{b_q} \beta_{qj}^2}{\sum_{j=1}^{b_q} \beta_{qj}^2 T_j}\right)\right]. \quad (7)$$

Here, $\theta_j$ is the characteristic vibrational temperature for the $j$th vibration, and $g_j$ is the multiplicity of its degeneration; $\beta_{qj}$ are the expansion coefficients for the $q$th reaction in coordinates of normal vibrations; $b_q$ is the number of modes participating in the $q$th reaction; $E_q^*$ is the energy corresponding to a certain vibrational level, being as though a "narrow neck" in the case of passing vibrationally excited molecules to the quasi-continuous (with respect to the energy) continuum in the $q$th reaction.

Let only one type of vibrations ($T_\xi = T_V$) be excited in molecules $A$. With allowance for (6) and (7), it is convenient to present the expressions for $[r_*]$ and $[r_*]_l$ in the form

$$[r_*] = [r_{*0}]\sqrt{\varphi_1(T, T_V)}, \quad [r_*]_l = [r_{*0}]_l \varphi_2(T, T_V).$$

Here, $[r_{*0}]$ is the maximum concentration of active radicals at $T_V = T$ and $l = 1$, while for $l \geq 1$, ($[r_{*0}] = \sqrt{k_1^0 [A]_0/2k_3^0}$; $[r_{*0}]_l = (l-1)k_2^0 [A]_0/2k_3^0$).

In the case of excitation of the component $A$ ($T_V > T_0$) $\varphi_1(T, T_V) > 1$ and $\varphi_2(T, T_V) > 1$. Therefore, $[r_*] > [r_{*0}]$ and $[r_*]_l > [r_{*0}]_l$. We assume that $[r_{*0}]_l < [r_{ign}]$ for the given $[A]_0$ and $T_0$; i.e., no regime of self-ignition is realized for both nonramified and ramified chain reactions. Exciting vibrations of molecules $A$ to a certain value $T_V$, it is possible to make the condition $[r_*]_l > [r_*] > [r_{ign}]$ fulfilled, i.e., to reduce both the temperature threshold and concentration threshold of the self-ignition. A relative increase in the concentration of active radicals $r_* = [r_*]/[r_{*0}]$ for $l = 1$ depends on $T_V' = T_V/T$ and $E_{V1}' = E_1^*/T$, while for $l > 1$, $r_{*l} = [r_*]_l/[r_{*0}]_l$ depends on $T_V'$ and $E_{V2}' = E_2^*/T$ ($E_1^*$, and $E_2^*$ are the values of $E_q^*$ for the reactions of initiation and chain ramification).

In Figs. 1a and 1b, we show $r_*$ as a function of $T_V'$ and $E_{V1}'$ and $r_{*l}$ as a function of $T_V'$ and $E_{V2}'$ for $l = 2$, respectively. In the same figures, we show in the ordinate axis certain values $r_{ign} = [r_{ign}]/[r_{*0}]_l > 1$ for $l = 1$ and $l = 2$; i.e., for the values $[A]_0$ and $T_0$ corresponding to $[r_{*0}]_l$, no self-ignition occurs. As is seen, the higher is $E_{V1}'$ for $l = 1$ or $E_{V2}'$ for $l = 2$, the lower is the degree of excitation for which the regime of the self-ignition ($r_* \geq r_{ign}$) is realized. It is natural that the degree of excitation must be lower in a ramified chain reaction for equal $E_{V1}'$ and $E_{V2}'$.

We illustrate the results obtained by the example for the $H_2 + O_2$ mixture. We consider the ignition of the mixed mixture in a certain region with the radius $R_a$. In this case, the time for active radicals to escape from the

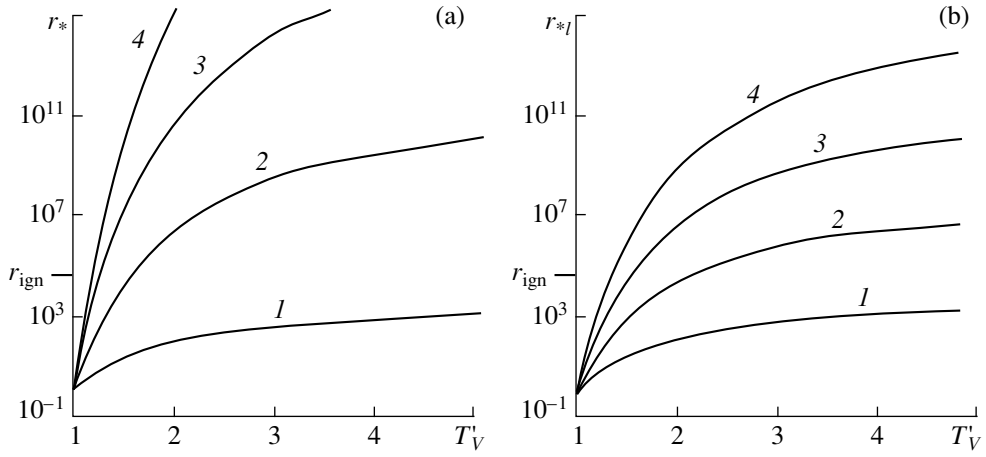


**Fig. 1.** Relative increase in the number of active radicals as a function of $T'_V$ for (a) nonramified reaction with $E'_{V1}$ equal to: (*1*) 20; (*2*) 60; (*3*) 100; and (*4*) 140 and (b) ramified reaction ($l = 2$) with $E'_{V2}$ equal to: (*1*) 10; (*2*) 20; (*3*) 30; and (*4*) 40.

reaction zone corresponds to the time of diffusion $\tau_i^D = \min\{\tau_{ik}^D\}$, and $\tau_{ik}^D = R_a/D_{ik}$, where $D_{ik}$ is the coefficient of the multicomponent diffusion occurring between the *i*th and *k*th components. The formation of active radicals is specified by the time $\tau_i^{ch}$ of the chemical reaction. If $\tau_i^{ch} > \tau_i^D$, no self-ignition occurs. For the $H_2$ + $O_2$ mixture, $\tau_i^D$ corresponds to the diffusion time ($\tau_H^D$) for hydrogen atoms.

To describe the process of self-ignition in a vibrationally nonequilibrium reacting gas for $t < \tau_H^D$, the set of equations is valid, which involves the equation for energy, the kinetic equations for concentrations of components and for the mean content of vibrational quanta in each mode participating in the reactions of molecules [2]. The analysis performed has shown that, for describing the low-temperature initiation of combustion in $H_2$ + $O_2$ mixtures, it is necessary to use the kinetic scheme including chemical reactions with participation of not only $H_2$, $O_2$, $H_2O$, OH, O, and H, but also $HO_2$, $H_2O_2$, and $O_3$:

(1C) $H_2O + M = OH + H + M$,

(2C) $H_2 + M = 2H + M$,

(3C) $O_2 + M = 2O + M$,

(4C) $H + O + M = OH + M$,

(5C) $H_2 + O = OH + H$,

(6C) $O_2 + H = OH + O$,

(7C) $H_2O + O = 2OH$,

(8C) $H_2O + H = OH + H_2$,

(9C) $H_2 + O_2 = 2OH$,

(10C) $HO_2 + M = H + O_2 + M$,

(11C) $H_2 + O_2 = H + HO_2$,

(12C) $H_2O + O = H + HO_2$,

(13C) $H_2O + O_2 = OH + HO_2$,

(14C) $H_2O + OH = H_2 + HO_2$,

(15C) $2OH = H + HO_2$,

(16C) $OH + O_2 = O + HO_2$,

(17C) $H_2O_2 + M = OH + OH + M$,

(18C) $H + H_2O_2 = HO_2 + H_2$,

(19C) $H + H_2O_2 = H_2O + OH$,

(20C) $2HO_2 = H_2O_2 + O_2$,

(21C) $HO_2 + H_2O = H_2O_2 + OH$,

(22C) $OH + HO_2 = H_2O_2 + O$,

(23C) $H_2O + O_2 = H_2O_2 + O$,

(24C) $O_3 + M = O_2 + O + M$,

(25C) $O_3 + H = OH + O_2$,

(26C) $O_3 + O = O_2 + O_2$,

(27C) $O_3 + OH = HO_2 + O_2$,

(28C) $O_3 + H_2 = HO_2 + OH$,

(29C) $O_3 + HO_2 = OH + O_2 + O_2$.

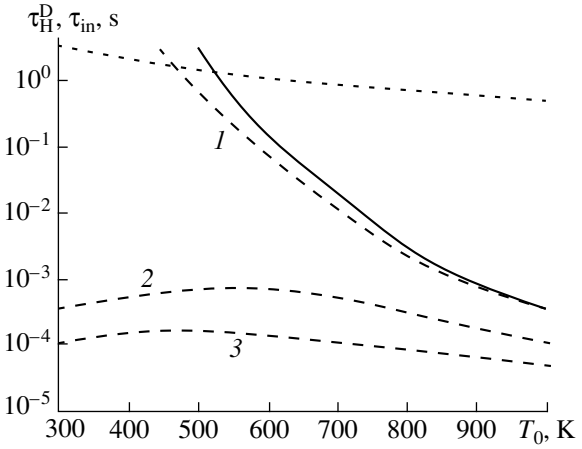


**Fig. 2.** Dependences (for the $2H_2 + O_2$ mixture at a pressure $P_0 = 10$ kPa) $\tau_{in}(T_0)$ in the absence of the preliminary excitation of initial reagents (solid line) and $\tau_H^D(T_0)$ with the preliminary excitation of vibrations in $H_2$ (dashed lines). $T_{40} =$ (*1*) 1000; (*2*) 2000; and (*3*) 3000 K.

In addition to the reactions indicated, we included into the kinetic model the processes of the vibrational-vibrational (*V–V'*) exchange between the symmetric, deformational, and asymmetric modes of $H_2O$ and $O_3$ molecules and modes of $H_2$, $O_2$, and OH molecules. We also included processes of the vibrational-translational (*V–T*) relaxation of the deformational modes for $H_2O$ and $O_3$ and modes of the $H_2$, $O_2$, and OH molecules. It was assumed that the vibrational energy released into modes of the $HO_2$ and $H_2O_2$ molecules when proceeding chemical reactions relaxes very rapidly into the translational degrees of freedom. (As estimates have shown, the rates of the *V–V'* and *V–T* processes for these molecules are higher than the rates of processes of the vibrational energy exchange in $H_2O$.) The temperature dependences $k_q^0(T)$, $W_{\xi,p}(T)$, and $W_{\xi,0}(T)$ for the chemical-reaction rate constants and for the *V–V'* and *V–T* exchange processes, respectively, are taken from [4]. For the processes $O_3(100, 001) + M = O_3(020) + M$ and $O_3(010) + M = O_3(000) + M$, the values of the reaction-rate constants are known only at $T = 300$ K (they are $5 \times 10^{-14}$ cm$^3$/s and $2 \times 10^{-14}$ cm$^3$/s, respectively) [8]. The temperature dependences for these processes were determined in accordance with the SSH theory [9]. The values of $E_q^*$ and the energy $E_r$ released into vibrational degrees of freedom, while

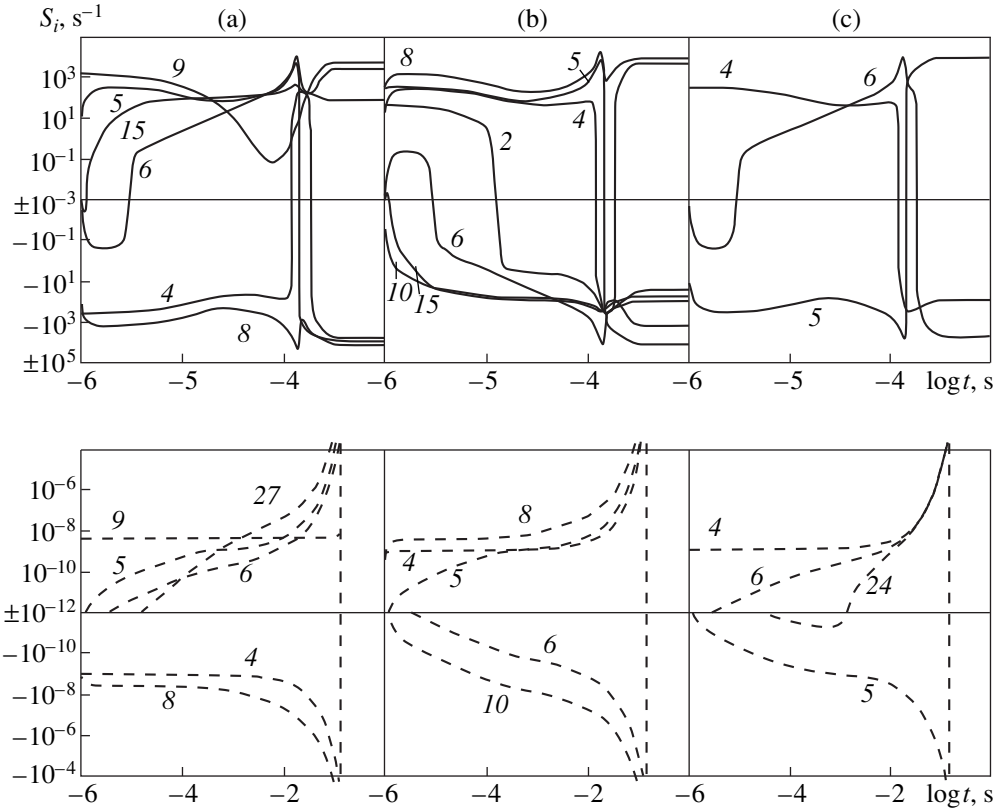


**Fig. 3.** Changing in the rates $S_i$ of the formation and disintegration of (a) OH; (b) H; and (c) O with time, while burning the $2H_2 + O_2$ mixture at $T_0 = 600$ K and $P_0 = 10$ kPa with ($T_{40} = 3000$ K) and without exciting vibrations in $H_2$ (solid and dashed lines, respectively). Ciphers near the curves $S_i(t)$ correspond to the numbers of chemical reactions.

forming a molecule in the *r*th chemical reaction, were calculated in the same manner as in [4].

At low temperatures ($T_0 \le 600$ K), there are marked differences in the mechanism of the combustion initiation of the $H_2 + O_2$ mixture as compared to higher values of $T_0$ even in the case of the absence of the preliminary excitation of the $H_2$ or $O_2$ molecules. At the initial stage, as for high values of $T_0$, the principal reaction initiating the formation of active OH radicals is the (9C) reaction. Furthermore, OH radicals dissociate [the (4C) reverse reaction] and also react with $H_2$, which is accompanied by the formation of $H_2O$ molecules and H atoms [the (8C) reverse reaction]. These products participate in two different processes. The former of them results in formation of O atoms [the (6C) reaction] and initiates the chain-combustion mechanism. The latter process results in the disappearance of H atoms and formation of $HO_2$ radicals [the (10C) reverse reaction]. At $T \ge 800$ K, the rate of the former process becomes higher than that of the latter one, but the situation alters to the opposite one at $T \le 600$ K. At $T \le 600$ K, an important source of O atoms is the dissociation of $O_3$ [the reaction (24C)], which is preliminary formed as a result of the interaction between $HO_2$ and $O_2$ [the (27C) reverse reaction]. The rate of the (24C) reaction is comparable to that of formation of O atoms in the reaction of the chain initiation. The (5C) reaction closes the chain mechanism for the combustion of $H_2 + O_2$ mixtures.

The preliminary excitation of $H_2$ or $O_2$ molecules significantly change the mechanism of the combustion initiation and results in decreasing $\tau_{in}$ at the same $T_0$. In Fig. 2, we show the dependences $\tau_{in}(T_0)$ in the case of the absence ($T_{\xi 0} = T_0$) and of the presence of the excitation of $H_2$ for various vibrational temperatures $T_{40}$ in $H_2$ and the dependence $\tau_H^D(T_0)$ for $R_a = 0.1$ m. As is seen, the condition $\tau_{in} > \tau_H^D$ is realized at lower $T_0$ in the case of the excitation of the $H_2$ molecules. Thus, at $T_{40} = 1000$ K, the self-ignition is possible at $T_0 = 500$ K, while at $T_{40} = T_0$—only at $T_0 = 550$ K. For a significant excitation of $H_2$ ($T_{40} \ge 2000$ K), the character of the dependence $\tau_{in}(T_0)$ changes in the range $T_0 = 600$–300 K; namely, the value of $\tau_{in}$ decreases with the reduction of $T_0$. In the case of a strong excitation of $H_2$ molecules, variation in the form of the dependence $\tau_{in}(T_0)$ is caused by a change in the mechanisms of production of O and H atoms, as well as OH radicals compared to unexcited gas. This is illustrated in Fig. 3 in which we show the variation of the OH, H, and O formation rates in the process of combustion of the hydrogen–oxygen mixture with and without the excitation of $H_2$ at $T_0 = 600$ K. It is seen that the excitation of $H_2$ leads primarily to a significant increase in the formation rate for OH radicals in the (9C) reaction and H atoms in the (8C) reverse reaction. In this case, an efficient source of H atoms becomes the reaction of dissociation of OH and $H_2$ [the (4C) and (2C) reactions, respectively]. An increase in the concentration of H atoms results in accelerating the formation of $HO_2$ radicals in the (10C) reaction. This process initiates increasing the rate of the (15C) reverse reaction, the growth in the concentration of OH radicals and, as a consequence, of H and O atoms as well.

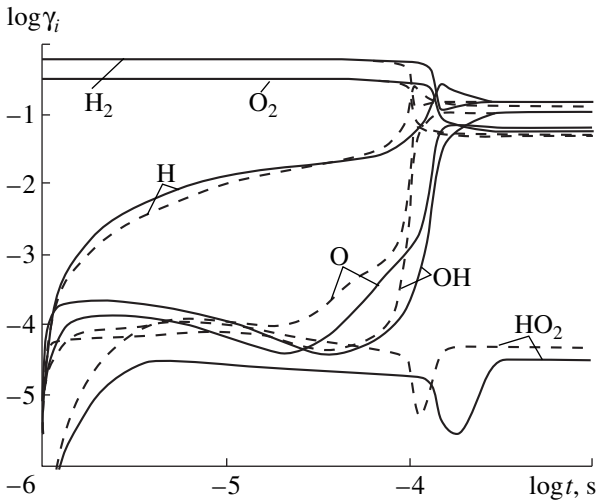


**Fig. 4.** Variation in concentrations for the OH, O, H, $HO_2$, $H_2$, and $O_2$ components with time in the case of combustion of the $2H_2 + O_2$ mixture at $P_0 = 10$ kPa, $T_0 = 600$ and 300 K (solid and dashed lines) in the case of exciting molecular vibrations in $H_2$ ($T_{40} = 3000$ K).

With decreasing $T_0$ from 600 to 300 K, the formation rate for $HO_2$ radicals in the (10C) recombination reaction increases. This fact, as was already noted above, results in increasing the concentration of OH radicals and H and O atoms, and thus, in intensifying the chain mechanism of the process and in reducing the period of induction. This can be clearly seen from Fig. 4, in which the dependences $\gamma_i(t)$, $i$ = OH, H, O, $HO_2$, $H_2$ and $O_2$ are shown for $T_0 = 600$ and 300 K.

The results obtained indicate a possibility of a significant (by the factor of two or higher) reducing the ignition threshold for combustible mixtures when exciting the molecular vibrations in initial reagents. In the case of the low-temperature initiation of combustion by means of a selective excitation of vibrational degrees of freedom in the reacting molecules, new mechanisms of formation of active atoms and radicals appear. These mechanisms can lead to a qualitative change in the dependence for the induction period on the initial temperature of a mixture.

## ACKNOWLEDGMENTS

This work was supported by the Russian Foundation for Basic Research, grant no. 99-01-01165.

## REFERENCES

1. R. O. Brown, Combust. Flame **62**, 1 (1985).
2. A. M. Starik and N. G. Dautov, Dokl. Akad. Nauk **336**, 617 (1994) [Phys.–Dokl. **39**, 424 (1994)].
3. E. M. Fisher, Combust. Flame **108**, 127 (1997).
4. A. M. Starik and N. G. Dautov, Kinet. Katal. **37**, 346 (1996).
5. A. A. Borisov, G. I. Scachkov, and K. Ia. Troshin, in *Advanced Computation and Analysis of Combustion* (Enas Publ., Moscow, 1997), pp. 79–89.
6. Ya. B. Zel'dovich, G. I. Barenblatt, V. B. Librovich, and G. M. Makhviladze, *Mathematical Theory of Combustion and Explosion* (Nauka, Moscow, 1980).
7. N. M. Kuznetsov, *Kinetika monomolekulyarnykh reaktsiĭ* (Kinetics of Monomolecular Reactions) (Nauka, Moscow, 1982).
8. W. T. Rawlins, J. Geophys. Res. **90**, 12 283 (1985).
9. F. J. Tanczaz, J. Chem. Phys. **25**, 439 (1956).

*Translated by V. Bukhanov*